# ENHANCED POWER SYSTEM RESILIENCY TO HIGH-IMPACT, LOW-FREQUENCY EVENTS WITH EMPHASIS ON GEOMAGNETIC DISTURBANCES

BY

MARYAM KAZEROONI

DISSERTATION

Submitted in partial fulfillment of the requirements
for the degree of Doctor of Philosophy in Electrical and Computer Engineering
in the Graduate College of the
University of Illinois at Urbana-Champaign, 2016

Urbana, Illinois

Doctoral Committee:

Professor Thomas J. Overbye, Chair
Professor Peter W. Sauer
Professor Deming Chen
Assistant Professor Hao Zhu
Dr. James D. Weber, PowerWorld Corporation

# ABSTRACT

Various reliability procedures have been developed to protect the power systems against common reliability issues that threaten the grid frequently. However, these procedures are unlikely to be sufficient for high-impact low-frequency (HILF) events. This thesis proposes several techniques to enhance resiliency with respect to HILF events. In particular, we focus on cyber-physical attacks and geomagnetic disturbances (GMDs). Corrective control through generation redispatch is proposed to protect the system from cyber-physical attacks. A modification of the optimal power flow (OPF) is proposed which optimizes the system resiliency instead of the generation cost. For larger systems, the burden of solving the resilience-oriented OPF is reduced through a fast greedy algorithm which utilizes proper heuristics to narrow the search space. Moreover, an effective line switching algorithm is developed to minimize the GMD impact for large-scale power systems. The algorithm uses linear sensitivity analysis to find the best switching strategy and minimizes the GIC-saturated reactive power loss.

The resiliency may be improved through power system monitoring and situational awareness. Power system data is growing rapidly with the everyday installation of different types of sensors throughout the network. In this thesis, various data analytics tools are proposed to effectively employ the sensor data for enhancing resiliency. In particular, we focus on the application of real data analysis to improve the GMD models. We identify common challenges in dealing with real data and develop effective tools to tackle them. A frequent issue with model validation is that for a real system, the parameters of the model to be validated may be inaccurate or even unavailable. To handle this, two approaches are proposed. The first approach is to develop a validation framework which is independent of the model parameters and completely relies on the measurements. Although this technique successfully handles the system uncertainties and offers a robust validation tool, it does not provide the ability to utilize the available network parameters.

Sometimes, the network parameters are partially available with some degree of accuracy and it is desired to take advantage of this additional information. The second validation framework provides this capability by first modifying the model to account for the missing or inaccurate parameters. Then a suitable validation framework is built upon that model. Another common issue that is widely encountered in data analysis techniques is incomplete data when part of the required data is missing or is invalid. Examples of missing data are provided through real case studies, and advanced imputation tools are developed to handle them.

*To my parents, for their love and support.*

# ACKNOWLEDGMENTS

Throughout the course of my Ph.D., I am grateful to those with whom I have had the opportunity to collaborate and all who have taught or mentored me. First, and most sincerely, I thank my advisor, Professor Tom Overbye, for his continual guidance and support throughout my graduate academic career. I have learned a lot from him about power systems and how to do research. Many thanks also go to my thesis committee for their interest, involvement, and encouragement of my work. Additionally, I extend my sincere gratitude to Dr. Kate Davis, adjunct assistant professor at the University of Illinois, and Dr. Saman Zonous, professor at Rutgers University, for their direct guidance on the work in Chapter 2.

Throughout graduate school, I had the privilege of participating in a few industrial internships. I extend thanks to all the mentors who guided me through these precious experiences: At MISO, I learned about power systems planning from Stuart Hansen, Jordan Bakke and Aditya Prabhakar; and at Fujitsu lab, I gained valuable experience in demand response and distribution systems under the guidance of Jorjeta Jetcheva, Daisuke Mashima and Wei-Peng Chen.

There have been quite a few other people I have worked with, who have inspired me with their support, encouragement, and advice. Thanks in particular to Jennifer Gannon, Shamina Hossain-Mckenzie, Komal Shetye and Mark Butala. I would also like to acknowledge my funding sources, the National Science Foundation (NSF), the Power Systems Engineering Research Center (PSERC), and the Illinois Center for a Smarter Electric Grid (ICSEG).

Finally, I thank my family, who sacrificed much to provide a better life for me. They instilled in me the value of hard work and discipline, the interest in mathematics and the belief that I could do anything. Last, thanks to my husband, Arash, for his unconditional support.

# TABLE OF CONTENTS

# CHAPTER 1

# INTRODUCTION

In this chapter, we motivate the need to improve power system resiliency against HILFs. We provide some background on the resiliency enhancement techniques and review the existing work on each topic discussed in the thesis. Finally, we state the contributions of this thesis and summarize the contents of each chapter.

## 1.1 Problem Statement

Merriam-Webster's dictionary defines *resiliency* as "the ability to become strong, healthy, or successful again after something bad happens" or "the ability of something to return to its original shape after it has been pulled, stretched, pressed, bent, etc."

The North American power grid is one of the most reliable in the world owing to the extensive use of reliability procedures including risk modeling, operator training, safety procedures, backup systems and operational communication protocols [1]. However, these procedures are unlikely to be sufficient for high-impact low-frequency (HILF) events. HILF events can cause catastrophic impacts on the grid, yet they rarely occur or, in some cases, may have never occurred before. Examples of HILF risks include coordinated cyber and physical attacks, and natural disasters like tsunamis, earthquakes, hurricanes, pandemics, and geomagnetic disturbances caused by solar weather.

There are several challenges associated with HILF: First, there is little real-world operational experience with respect to HILFs for the simple reason that they happen rarely. Moreover, they are usually caused by uncontrollable external forces. For example, vegetation contact with transmission lines may be avoided by proper control actions, yet no action can reduce the probability of geomagnetic storms. Finally, their risk assessment is difficult since historical events may not

reflect the potential future impacts [2].

The system vulnerability to cyber attacks have increased over the past years. Cyber physical attacks involve targeting multiple key components in the system in a coordinated fashion, which brings the system outside the protection provided by traditional operating protocols. The growing use of communication technologies, the increasing diversity of the system components and finally more reliance on the remote monitoring and automated control are factors that contribute to this growing vulnerability.

Power systems today are more vulnerable to severe GMDs. High-voltage transmission lines have increased by a factor of ten in mileage since 1950s [3]. The voltage level has also increased from 100-200 KV to 345-765 KV, which reduces the line resistances and hence increases the GMDs impacts.

This thesis focuses on enhancing the power system resiliency against HILFs. In particular, we focus on improving resiliency against 1) cyber physical attacks and 2) geomagnetic disturbances. Line switching and generation redispatch are considered as corrective control actions, and effective design procedures are proposed to improve resiliency. Moreover, various data analytics tools are proposed to effectively employ the sensor data for enhanced resiliency applications. GIC data and magnetic field measurements are utilized to improve the GMD models and better evaluate the GMDs negative impacts. The key challenges in dealing with the real data are identified and effective tools are developed to tackle them.

## 1.2 Background

Reliability and resilience are both relevant concepts in power system analysis. Reliability is the ability of the system to deliver power consistently. It is a binary indication of the system performance where the system is either functional or failed. Interruption indices defined by the IEEE standard 1366 are used to measure reliability [4]. While interlinked, a reliable grid is not necessarily resilience and vice versa. Reliability focuses on continuous power delivery and can be described as the end goal. The resiliency framework recognizes that disruptive events are inevitable and focuses on regaining the system functionality quickly and with minimum damage. Resiliency may

be considered as the realistic compromise that captures the unpredictable nature of disturbances.

Enhancing power system resiliency comprises four components [5]. The first building block is damage prevention prior to the event, i.e., the ability to keep the system operational in the case of a disturbance. The second component is resourcefulness during the event, which entails the ability to manage a disaster as it unfolds. It includes identifying the options, prioritizing them, and communicating the decisions to the corresponding entities. Resourcefulness depends mostly on people, not technology. The third component is the rapid recovery that is the capability to move back to normal condition as quickly as possible after an event. The last building block is adaptability, which is learning new lessons from the event. The knowledge obtained from each event can help to revise the existing procedures and develop new ones. Adaptability is performed at all times and improves damage prevention, resourcefulness, and recovery.

Various strategies may be used for damage prevention: First, risk assessment may be employed to analyze the probability of different events and evaluate their impacts on the grid. Second, the grid should be strengthened against HILF events. Upgrading poles and structures with stronger materials and using underground lines are effective hardening strategies against hurricanes. Elevating/relocating substations and moving the equipment of critical buildings to upper floors reduce vulnerability to floods. The third approach is to improve the grid robustness. Building more transmission lines, increasing the energy storage capacity and employing advanced technologies in communication, building controls, and distributed generation can improve the system robustness. The fourth approach is situational awareness. Until recently, utilities have detected outages when customers called and reported them. The outage notification system provided by the smart meters and the time-synchronized visibility capabilities of the phasor measurement units (PMUs) can increase the situational awareness. Corrective control through automated feeder switching contributes to enhanced resiliency as well. Other examples of damage prevention techniques include improving cyber and physical security and enhancing cooling strategies and health sensors of power system components [6].

The term "new normal" is introduced in [5] to describe the degraded planning and operating condition during HILF events. Once the event occurs, the mitigation procedure is employed to minimize the impacts and maximize the service to consumers. This might take days since resources such as reserve capacity, spare equipment and personnel are limited. In the restoration phase, the

system is restored to the new normal and may stay there for months or even years before it returns to pre-event reliability level. Some challenges associated with the new normal operation are:

- Rotating blackouts are designed to maintain reliability with limited generation and transmission resources and unfamiliar operating conditions.
- Other critical infrastructures are affected, e.g., there might be gasoline and diesel fuel shortages before the oil refineries can recover from the event.
- The protection devices are configured for normal operation, which may be too restrictive for the degraded operating state and, hence, may need to be reconfigured.
- The generation dispatch and transmission system operation may need to be executed manually, which increases the human error likelihood.

Remedial action schemes (RAS) are effective solutions to strengthen the system against HILF events [7, 8, 9]. RAS [10] is an automatic protection system designed to detect abnormal or predetermined system conditions and then to take corrective action to restore the power system's safe operational mode. RAS actions may include simple isolation of faulted components to maintain system reliability or changes in demand, generation (MW and Mvar), or system configuration to maintain system stability, acceptable voltage, and/or power flows. The resiliency benefit offered by RAS has urged many utilities to implement them in their systems [11]. RAS are widely deployed, e.g., by Southern California Edison [12], Bonneville Power Administration (BPA) [13] and British Columbia transmission corporations (BCTC) [14].

Power system monitoring improves the situational awareness and consequently the resiliency. With the new developments in the monitoring devices and the growing emphasis on the smart grid, utilities have been installing different kinds of sensors throughout the network. Remote terminal units (RTUs) and supervisory control and data acquisition (SACADA) systems are the conventional monitoring systems that have been widely used in power systems. These systems provide only the magnitude and not the phase angle and have lower sampling rate, i.e., 2-4 seconds. PMUs are the new technology that provide high-resolution synchronized measurements of both magnitude and angle with sampling rate of up to 60 samples per second. Data from the sensors can be used for different applications including power system resiliency. State estimation is constantly used in the

power system operation and the sensor data can improve its performance significantly. Data may also be used for off-line applications such as model validation. Existing models can be validated by comparing the sensor data with the values obtained from the model. More importantly, one can improve a model by making proper adjustments, which increases the agreement between the data and the model-based values.

## 1.3 Literature Review

In this section, we review the existing work related to the techniques developed in this thesis.

### 1.3.1 Generation Redispatch for Cyber Attacks

In the conventional RAS designs, offline calculations are performed to obtain the best control action for the most credible contingencies. These actions are stored and executed in real time when a contingency occurs. The optimal control action depends on the real time state of the system, e.g., the network topology and the amount of generations and loads. The offline calculation considers different scenarios for the system state and stores the best action for each scenario in the form of an arming table. For example, BPA RAS includes a 2D arming table which specifies the amount of generation drop at a particular generator based on the pre-contingency flow level across two major transmission lines [13]. A similar arming table is used for BCTC RAS [14]. Creating and storing such arming tables require lots of data management and may still not capture all possible scenarios that might happen in the case of a real contingency. This is especially important during HILF events when the system is likely to be in an unfamiliar operating condition. To tackle this, online RAS design may be used to calculate the best action in real time. Online RAS designs should be computationally inexpensive as it is desired to execute the control action as quickly as possible.

Corrective controls deal with the system during disturbances when the dynamics are significant and transient stability is crucial. Hence, the system dynamics are considered in the design of many corrective control applications [15, 16]. A transient stability index is defined in [17], based on the maximum angle separation of any two generators during the transient simulation, to assess the dynamic security of the system after executing each candidate corrective action, and the best action

is determined accordingly. Transient energy analysis through a single machine equivalent (SIME) is used in [18] for designing corrective control. Transient stability analysis is computationally expensive, and getting a transient stability solution requires significantly more computation than solving the power flow in steady-state. Hence, performing RAS design in the context of steady-state analysis may simplify the calculations and improve the computational complexity. Steady-state analysis techniques are well-established, and many useful tools (e.g. sensitivity matrices like the line outage distribution factor) exist in the literature which can be utilized in the RAS design. An algorithm is proposed in [19] to find the best lines to be opened for improving the system security. The power flow on the lines before and after a line is opened is used as the criteria for selecting the optimal line. Corrective voltage control through line and bus-bar switching is presented in [20] where the best switching action is determined based on some static security indices. Steady-state analysis techniques are suitable for online RAS design applications where the optimal control action needs to be calculated quickly.

### 1.3.2 GMD Mitigation through Line Switching

Solar coronal holes and coronal mass ejections can disturb the Earth's geomagnetic field. These GMDs in turn induce electric fields which drive low frequency currents in the transmission lines. These geomagnetically induced currents (GICs) can cause increased harmonic currents and reactive power losses by causing transformers half-cycle saturation. This may cause voltage instability by a combination of two means. First, the increased transformer reactive power losses may lead directly to voltage instability. Second, the harmonic currents might cause relay misoperation and unintended disconnection of the reactive power providers such as static VAR compensators (SVCs) [21, 1].

Motivated by the negative impacts of GMDs, various mitigation techniques have been investigated in literature [22, 23]. Capacitors may be installed at the transformer neutral to block GICs. If correctly placed at proper locations, this technique can reduce the GIC-saturated reactive power loss [24, 25]. Installing a capacitor at the neutral may compromise the ground fault detection system or cause insulation hazards and safety risks. Possible solutions to reduce such risks are using parallel resistors or spark gaps, vacuum switching or interrupting the protection circuit [26, 27].

The tradeoff with these solutions is increased complexity, bulkiness and cost. Series capacitors [25], polarizing cells [28], and neutral linear resistance [28, 29] are other types of blocking devices investigated in literature for GMD mitigation.

Line switching has been studied as an effective control strategy to improve power system security [30, 20, 31]. Line outage distribution factors (LODFs) are utilized in [19] to rank the candidate switching actions. Similar sensitivity factors are employed in [32] and [20] to determine the best switching actions. Topology control can modify the line flows so that the overloads and voltage violations are relieved. Using the same concept, the GIC flows may be redirected through line switching to reduce the negative impacts. To the best of our knowledge, GMD mitigation through topology control has not been investigated in literature so far.

The existing GIC mitigation programs focus on the dc analysis of the system and reducing the GIC flows. The ac power flow solution is coupled with the GIC flows and it is desired that the mitigation framework integrates some aspects of the ac analysis along with the already existing dc ones. This is especially important when line switching or series capacitors are considered as the control action. Topology control changes the ac flows and, if not performed correctly, may cause overloads and voltage violations. An effective GMD mitigation should properly model the effect of GICs on the ac power flow solution and develop a strategy that provides sufficient security measures in terms of both GIC flows and ac analysis.

### 1.3.3 GMD Model Validation Based on Real Data

In order to better understand the impacts, it is important to use actual data, when available, to validate the associated models. GIC modeling has been extensively studied [33, 21, 34, 35, 36, 37]. It has been shown that the transformer GIC is linearly related to the electric field, where the linear coefficients depend on the given power system parameters. A variety of GIC flow software and a benchmark test cases have also been developed [38, 37, 39, 40]. However, little previous work has been done in the area of system-wide GIC model validation.

A key task in model validation is to recreate the system model during a fault or event. In the case of a geomagnetic storm, the magnetic field measurements are used to reproduce the electric field and eventually the induced currents. [41] recreates the March 1989 storm for the Ontario

high-voltage network and validates the records of the GIC measurements accordingly. Various methods for modeling the neighboring networks during GMDs are presented in [42] and their effectiveness is validated for the Ontario-Montreal Network. This thesis builds on the existing literature on the GIC model validation with more focus on the transmission-level study as well as system uncertainty considerations. The goal is to identify the key challenges in model validation and eventually develop a general approach which addresses these issues.

The difficulty of GIC model validation lies in various aspects. First, the exact information on the power system topology and dc conductance is hard to obtain, thus so are the linear coefficients. The substation grounding resistance is especially a key element in GIC modeling which is seldom available [43]. Secondly, the electric field needs to be estimated from the magnetic data and this estimation is not exact. Various methods have been developed to effectively determine the E-field through the magnetic and Earth conductivity data [44], yet this data is not accurate, which introduces error to the resulting E-field. Last, the measured data mostly suffer from random noise and system perturbations. Hence, all the model components which include the linear coefficients, the input electric field, and measurement noise model are either unavailable or inaccurate. This emphasizes the need for validation techniques which are robust to such system uncertainties.

Reference [36] presents a linear model which relates the E-field to the GICs through the network topology and resistances. This model relies on the network parameters and its performance depends on the parameters accuracy. If model parameters are not available accurately, the alternative is to develop validation techniques that are independent of the parameters.

### 1.3.4 Substation Grounding Resistance Estimation

A key factor in the GIC modeling is to calculate the linear coefficients. Because of the dc nature of GIC flows, these coefficients depend on the network topology and resistances, where the accuracy of the latter depends on the available network information. Most of the parameters required for calculating the linear coefficients are part of the standard power flow models and are usually available. The only piece of information which may not be available, but strongly affects the modeling accuracy, is the substation grounding resistance. Substation grounding resistance is the effective grounding resistance of the substation neutral which includes the grounding grid and

the emanating ground paths due to shield wires grounding. This parameter depends on the local soil humidity and the ground conditions. Hence, it is very challenging to obtain an accurate value for this parameter in practice.

The effect of inaccurate substation grounding resistance on GIC calculations has been studied previously in the literature. Reference [40] provides a mathematical technique for calculating the effect of grounding resistance on the GICs, and [43] demonstrates the impacts through numerical results on the Finish 400kV grid. In reference [45], a sensitivity analysis has been performed on the 62,500 bus Eastern Interconnection system which demonstrates the significance of grounding resistance for calculating the GIC flows. These previous papers emphasize the need to have accurate grounding resistances for GIC analysis.

A variety of techniques are available in the literature to measure the substation grounding resistance [46, 47]. Four-point method and fall-of-potential method are common procedures for measuring the earth resistivity [48]. The grounding resistance can be calculated from the resistivity through a uniform soil model where the resistivity is assumed to be the same at all depths [49]. Alternatively, a two-layered model may be used, especially at locations near lakes, rivers or mountains where the soil resistivity is not uniform in horizontal direction [50].

These measurement-based approaches to obtain grounding resistances can be complicated by a variety of uncertainties. First, external objects such as water pipelines and adjacent railroad tracks distort the earth potential contours and introduce significant error. This effect can be reduced by aligning the test probes perpendicular to the external object and/or locating the probes far from the object. Second, sources of dc current such as dc railroad tracks, pipelines cathodic protection systems and dc transmission lines produce stray currents which interfere with the grounding resistance measurements. Periodically reversed direct currents can be used in the measurements to reduce the stray currents. Third, the resistance of the electrodes used for the measurements can introduce error if the substation being tested has low resistivity. This type of error can be reduced by either increasing the voltage of the power supply or decreasing the electrode resistance. The complexities associated with measuring the resistances encourage developing alternative techniques to determine them.

### 1.3.5 Enhanced Magnetic Field Estimation

The GICs are driven by the electric field, and an accurate GIC model requires accurate electric field as its input. Estimating the electric field from the magnetic field is presented in [1]. The magnetometers operated by the United States Geological Survey (USGS) and Canadian Space Weather Forecast Center (CSWFC) provide the magnetic data in North America. Unfortunately, the available data is very sparse over the special area with only 26 observatories in all of North America. Various methods have been investigated to interpolate the magnetic field over the Earth's surface. General interpolation techniques such as linear, nearest neighbor, BiHarmonic Spline and Kriging may be used for interpolating magnetic data as presented in [51]. Fourier analysis is used in [52] to obtain the ionospheric currents which produce the magnetic field. With these currents available, the magnetic field at any point in the space is calculated. [53] calculates the ionospheric currents based on the Maxwell's equations using a physical rather than mathematical approach.

### 1.3.6 Enhanced E-field Estimation

Least squares (LS) estimation is used in [54] to estimate the electric field through the GIC measurements. This technique can be improved by utilizing additional information about the E-field. The auto-correlation of the E-field data indicates that it is statistically correlated in the time domain. Hence, a dynamic model can be developed which captures the E-field temporal correlation. Moreover, it has been demonstrated that the estimator accuracy can be greatly affected by the characteristics of the additive measurement noise. Hence, thorough characterization of the noise would greatly benefit the evaluation of the estimation accuracy. One simple way to characterize the noise is to assume each meter follows some given noise scenario. However, this model is limited because it fails to capture all possible noise scenarios simultaneously. Therefore, developing a general model which accounts for various noise scenarios is highly desired.

### 1.3.7 Adding GMD Models to the Existing Test Cases

One of the key challenges in GMD studies is the shortage of suitable test cases for evaluation purposes. Various power system test cases have been developed to validate the models associated

with different aspects of power system such as power flow, dynamics, distributions, reliability [55, 56]. These cases are designed for ac analysis and do not contain the necessary inputs such as substation grounding resistances and geographic coordinates which are essential for GMD studies. Hence, developing realistic test cases which include GIC-related parameters is extremely useful for GMD studies. Reference [40] presents a 17-bus system designed for GIC calculation which models the Finish 400-kV grid. A 20-bus test case is designed in [38] for GMDs studies which includes transformer models and two voltage levels. These cases do not contain the ac power flow parameters and, hence, cannot be used for steady-state voltage stability analysis under a GMD. Reference [39] proposes an algorithm to generate realistic synthetic power system test cases. These cases include both the ac power flow parameters and the GMD-related parameters.

The geographic coordinates are the key parameters which are missing in the standard cases and are essential for GIC analysis. Graph drawing techniques may be utilized to obtain the geographic layout and consequently determine the coordinates. A drawing of a graph is a pictorial representation of its vertices and edges. Very different layouts can be generated for the same graph with varying levels of understandability, usability and aesthetic. Various techniques have been developed for graph drawings each attempting to achieve different quality measures [57, 58]. The common quality measures used for graph drawings are crossing number (number of edge pair that cross each other), the drawing area (the size of the smallest bounding box relative to the closest node distance) and symmetry display.

## 1.4 Contribution of Thesis

This thesis focuses on enhancing the power system resiliency against HILFs. A generation redispatch algorithm is developed to strengthen the network against simultaneous attacks on multiple generators. The proposed method is designed for real-time applications, so that it can capture the uncertainties in the system operating condition during the attack. Moreover, it incorporates the possibility that certain generators are not available to participate in the dispatch due to malicious control. Moreover, the thesis presents several techniques to improve resiliency against GMDs. First, an effective line switching strategy is proposed which minimizes the GIC-saturated reactive

power loss in the system. The proposed switching strategy redirects the GIC flows in a controlled manner to minimize their impacts. Second, various techniques are developed to improve GIC modeling. These techniques contribute to the accurate GMD risk assessment and consequently enhanced resiliency. Moreover, GMD modeling serves as a fundamental building block for many of the hardening procedures including the proposed corrective line switching. The contributions of the thesis to GMD modeling are itemized below:

- Several techniques are developed to validate the GMD models based on the GIC measurements. The sources of error in the measurements, the network parameters and the input E-field are identified and a validation framework is developed which is robust to such uncertainties.

- An effective tool is developed to estimate the substation grounding resistance based on the GIC measurements. This eliminates some of the uncertainties in the GIC modeling.

- An interpolation technique is proposed to estimate the magnetic field at any location over the earth's surface using the sparse available measurements. This facilitates the GIC model validation by providing better magnetic field input.

- Several techniques are proposed to estimate the electric field from GIC measurements. The impact of the measurements error on the performance of the proposed estimators is analyzed extensively.

- A framework is developed to incorporate GMD modeling into the already-existing standard power system test cases. This reduces the shortage of suitable test cases for GMD evaluation purposes.

## 1.5 Thesis Organization

**Chapter 2.** In this chapter, we propose a generation redispatch algorithm to protect power systems against credible contingencies due to accidental failures or malicious endeavors such as cyber attacks. Two generation redispatch algorithms are proposed: A) a modification of the optimal power

flow (OPF) which maximizes the system resiliency, B) a fast greedy algorithm through control subspace synthesis which utilizes effective power system heuristics to narrow the search space. The computation complexities of the proposed algorithms are analyzed and proper modifications are employed to improve the running time for online RAS applications.

**Chapter 3.** This chapter provides detailed background on GICs, their negative impacts and the fundamentals of their modeling.

**Chapter 4.** Topology control is considered as a remedial action to protect the network for GMDs. Similar to the conventional LODFs, transformer LODFs (TLODFs) are defined as the sensitivity of the transformer GIC-saturated reactive power loss to line outages. An algorithm is developed to find the best line switching strategy which minimizes the total GIC-saturated loss based on TLODFS. The coupling between the ac power flow solution and the GIC flows is modeled and proper heuristics are developed to maintain sufficient ac-related security measures. Finally, the scalability of the algorithm to large systems is analyzed and effective techniques are proposed to improve the computational complexity for large-system applications.

**Chapter 5.** This chapter proposes singular value decomposition (SVD) to validate the GIC model. The singular vectors of the GIC matrix concatenated by all the currents across time can be used to infer the electric field. It hence becomes possible to validate the estimated electric field with the actual one obtained from the records of geomagnetic data. This method is unconstrained to the parameters availability and, more importantly, is robust to random noise. The work presented in this chapter was published in [59].

**Chapter 6.** SVD-based analysis successfully handles the system uncertainties and offers effective validation tools. However, it is desired to develop a technique with the ability to utilize the network parameters in case they are available. Sometimes, the network parameters are partially available with some degree of accuracy and it is desired to take advantage of this additional information. Chapter 6 proposes a validation technique which improves on the SVD-based one by utilizing the available parameters. In this technique, first, the conventional GIC model is modified to account for the system uncertainties. Then, a validation framework is built upon this modified model. This framework is successfully demonstrated using a PowerWorld case study and its performances is evaluated. The work presented in this chapter was published in [60].

**Chapter 7.** This chapter proposes a technique to estimate the substation grounding resistance

using GIC measurements. In this technique, the GICs at the substations being tested are collected and the sensitivity of the GICs to the grounding resistances are calculated. Then, the problem is formulated in the form of linear regression model with unknown grounding resistances. By observing the GICs, the calculated sensitivity factors would become the constant coefficients of the linear model. This technique requires only the GIC measurements at the substations being tested and the information on the network topology and other system resistance parameters. This information is part of the power flow model and is usually available with good accuracy. The work presented in this chapter was published in [61].

**Chapter 8.** This chapter focuses on interpolating the magnetic field data to improve the GIC model validation. In order to correlate the GICs flowing in transformer neutrals, it is important to have a good understanding of how the electric field varies across the grid. Magnetic field interpolation benefits the power engineers by providing an estimate of the electric field at any point in the grid. The work presented in this chapter was published in [62].

**Chapter 9.** In this chapter, the E-field dynamic modeling is presented as an effective technique to improve the E-field estimation. Actual magnetic field measurements during several GMD events are used to develop a practical dynamic model and later a Kalman-filtering framework. The overall performance of the proposed estimation technique over the conventional LS estimation is demonstrated through simulation. The work presented in this chapter was published in [63].

**Chapter 10.** This chapter considers the uncertainties on the GIC measurements and their impacts on the E-field estimation. Realistic noise scenarios for GIC measurements are considered and various estimators are introduced to handle the uncertainties. The LS estimator is investigated for GIC readings with white Gaussian noise, while the lease absolute value (LAV) estimator is proposed to handle outliers. Ridge regression (RR) estimator is proposed as an alternative to LS method when additional information on the prior electric field is known. Moreover, a general probabilistic GIC measurement model has been developed which accounts for realistic noise scenarios. Using the probabilistic model, the accuracy and reliability of the LS estimator are derived analytically. The work presented in this chapter was published in [64] and [54].

**Chapter 11.** In this chapter, a framework is developed to incorporate GMD modeling into the already existing standard power system test cases. The Kamada and Kawai (KK) algorithm and Force-directed (FD) method are presented as two effective graph drawing algorithms. The

geographic layout is developed using these techniques, and the substation coordinates, the key parameters required for GIC analysis, are obtained. The effectiveness of these techniques in retrieving the coordinates is evaluated through numerical results using the a 20-bus test case. Moreover, the proposed procedure is applied to the IEEE 24-bus system and the necessary GMD-related parameters are defined for this case.

# CHAPTER 2

# GENERATION REDISPATCH DURING CYBER ATTACKS

## 2.1 Introduction

Enhanced power system resiliency requires not only security incident detection solutions but also automated intrusion response and recovery mechanisms to tolerate ongoing failures and maintain the system's crucial functionalities. In this chapter, we present a design procedure for generation redispatch that improves the resiliency of the power systems against credible contingencies with emphasis on cyber attacks. Two generation redispatch algorithms are proposed: A) a modification of the optimal power flow (OPF) which optimizes the system resiliency instead of the generation cost, B) a fast greedy algorithm which utilizes proper heuristics to narrow the search space. The proposed techniques are computationally inexpensive and are suitable for online RAS applications. We applied the proposed techniques to systems of different sizes and validated their practical deployability through case studies. The contributions of this chapter are as follows:

- We reformulate the OPF in the context of security control and develop a resilience-oriented generation redispatch.
- We propose a greedy algorithm for calculating the optimal generation redispatch through control subspace synthesis. Proper heuristics are considered to narrow down the search space and reduce the computational complexity without compromising the performance.
- We propose a security assessment measure, the *violation index*, to evaluate the security of each candidate action and select the best ones. The violation index considers the physical and operating constraints of the system and evaluates the amount of constraint violation after executing each action. The index is calculated through static and fast steady-state power flow solution.

- We develop an algorithm to identify the critical generators that should participate in RAS logic synthesis. Furthermore, we implemente a working prototype of our proposed solution and validate its practical deployability on realistic power system topologies.

The chapter is organized as follows: We review the past related work in Section 2.2. Power system security control is described in Section 2.3. The reliability-based OPF analysis is presented in Section 2.4. Section 2.5 introduces the security-sompliant sontrol subspace synthesis. Section 2.6 demonstrates the proposed design procedure through numerical results. Section 2.7 concludes the chapter and discusses the future work.

## 2.2 Related Work

Due to the increasing concerns regarding power system stability guarantees in the case of potential contingencies, there has been extensive past work on power system protection. Here, we review the most related recent research.

**Control network protection.** We now review some representative past efforts at securing control systems. Stouffer et al. [65] present a series of NIST guideline security architectures for industrial control systems that cover supervisory control and data acquisition (SCADA) systems, distributed control systems, and PLCs. Such guidelines are also used in the energy industry [66, 67]. It has, however, been argued that compliance with these standards can lead to a false sense of security [68]. There have also been efforts to build novel security mechanisms for control systems. Mohan et al. [69] introduced a monitor that dynamically checks the safety of plant behavior. A similar approach using model based intrusion detection was proposed in [70]. Goble [71] introduced mathematical analysis techniques to quantitatively evaluate the safety and reliability of a control system including its PLC devices. However, the proposed solution focuses mainly on accidental failures and does not investigate intentionally malicious actions.

**Power system security.** There are two types of security control in power systems: preventive and corrective. Preventive control operates the power system in a way that remains secure even when a contingency occurs. The problem with preventive control is that it is not economical since operation is impacted at all times by contingencies which happen infrequently. On the other hand,

corrective control acts to retain system stability only after a contingency occurs. The challenge with corrective control is that it needs to be executed very fast (usually within 10 to 12 cycles) before the system loses synchronism.

The RAS design generally requires an iterative procedure for any given contingency. A set of candidate actions (feasible actions which may improve system security) is generated, and the system security is evaluated for each candidate action; then, the best action is selected accordingly. Existing RAS designs can be classified from two aspects. The first is the method used for assessing the system security of the candidate actions. For example, the transient stability index was introduced and used in [17], transient energy in [19, 18], the line flows before and after opening a line in [19], and voltage security margin in [72]. The second is the type of action considered in the RAS design. For example, generation dispatch was investigated in [17, 15, 18], generation tripping in [73, 16], load shedding in [74, 75] and line switching in [20, 19, 32, 30]. While many RAS designs are based on an iterative approach, some formulate the security problem in the form of an optimization problem and find the best action directly. The optimal power flow is reformulated in the context of security control in [76] and the optimal generation dispatch is calculated. Transient energy analysis is used in [16, 18] to find the generation dispatch/tripping which provides the highest stability measure. The proposed technique uses a security index for selecting the best actions, focuses on generation redispatch as the control action and investigates both iterative approach through the greedy search and direct optimization through the resilience-oriented OPF. To the best of our knowledge, this combination of features is unique among the existing RAS designs.

## 2.3 Power System Security Control

The power system state can be classified into three categories from the security perspective:

1. Normal State: when all the loads in the system are supplied and no constraint is violated.
2. Emergency State: when all the loads are supplied and one or more constraints are violated.
3. Restorative State: when there is loss of load (partial or total blackout) and no constraint is violated.

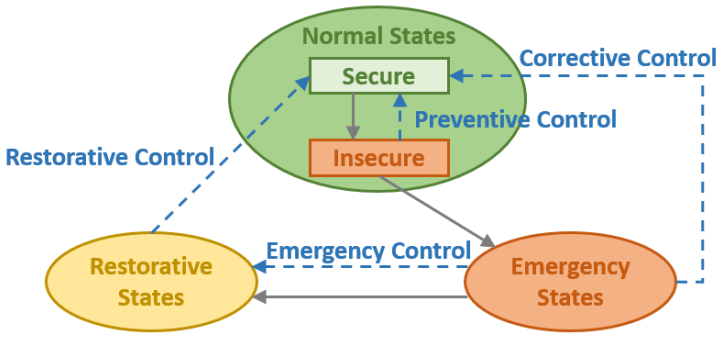


Figure 2.1: The security framework through preventive and corrective control.

When a contingency occurs, e.g., a line outage or generator failure, the system might transition from the normal state to emergency state and, in severe cases, to the restorative state. The goal of the security control is to prevent transitioning to restorative state.

### 2.3.1 Remedial Action Schemes

An alternative and more reactive approach to maintain system security is to use runtime corrective control through remedial action schemes (RAS). Unlike the security constrained OPF (SCOPF), this scheme allows the system to transition to the emergency state and then takes corrective actions to drive it back towards a safe state and normal operational mode. The corrective control needs to be executed quickly, usually within 10 to 12 cycles. Otherwise, the system might transition to the restorative state before the control action is employed. Commonly used remedial actions are shedding generation, tripping lines, switching shunt capacitors, moving phase shifter taps, and controlled islanding. Figure 2.1 illustrates the security framework through preventive and corrective control.

RAS includes a line status monitoring system to detect the contingencies. Controller logic is designed to evoke the proper action for each contingency as illustrated through an example in Fig. 2.2. In this example, the loss of line $A$ triggers the RAS Action I. The subsequent loss of line $B$ activates RAS Action II (possibly more severe). The loss of line $B$ by itself will not evoke any RAS action.

The amount of load/generation that needs to be shed in a RAS action depends on the state of

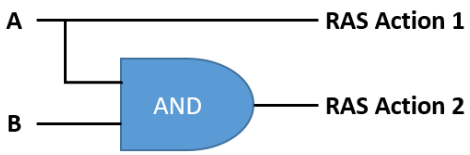


Figure 2.2: Example of RAS controller logic [13] .

the system, e.g., line flows, and generation outputs. This can be implemented through lookup tables that are designed offline which determine the amount of generation shedding for specific set of line flows. In most utilities, like the Bonneville Power Administration (BPA), this process is done manually by the system operator [13]. However, utilities are moving towards automating the process; e.g., the British Columbia Transmission Corporation has already employed automatic arming of the RAS in their system [14]. Automated arming of RAS reduces the arming time, minimizes operation risk and reduces the risk of human error. Moreover, it has full potential for expansion by adding control actions which can push the operating envelope.

## 2.4 Resilience-oriented OPF

We present an automated procedure to design RAS for a given power system topology and its state vector. The generated RAS logic attempts to keep the power system safe from all potential upcoming contingencies. First, contingency analysis is performed to identify the list of incidents that drive the power system to the emergency state. For each credible contingency, a remedial action is calculated and developed that brings the system back to its normal safe state. In this section, a generation redispatch technique is developed through reformulating the OPF to maximize the system security.

First, we give a quick review on optimal power flow (OPF). OPF minimizes the operation cost subject to the power flow and other constraints:

$$min \;\; f(x,u) = \sum_{i \in \mathcal{U}_G} C_i(P_i)$$

$$s.t \quad g(x,u) = 0$$

$$h(x,u) \leq 0 \tag{2.1}$$

where $u$ is the control variable and $x$ is the state variable, which includes the voltage phasors (magnitudes and phase angles) on individual power buses. The voltage magnitude of the PV buses (generators) and the voltage magnitude and angle of the slack bus are excluded since their values are known. The control variables are the generator MW output set-points, settings of the flexible alternating current transmission system (FACTS) devices, phase shifting transformers, and static VAR compensators. For simplicity and without loss of generality, only the generator MW output may be considered as control variable and the objective function may be written as:

$$f(x,u) = \sum_{i \in \mathcal{U}_G} C_i(P_i) \tag{2.2}$$

where $C_i(P_i)$ is the cost of operating generator $i$ with the MW output of $P_i$, and $\mathcal{U}_G$ is the set of generators.

The equality constraint $g(x,u)$ corresponds to the power flow equations and ensures that the active and reactive power at the PQ buses (loads) and the active power at the PV buses (generators) match their given values. The inequality constraint $h(x,u)$ may include the line flow limits, the voltage magnitude limits and the generators output limit as given by:

$$\begin{aligned}
V_i^{min} \leq V_i \leq V_i^{max} \quad & i \in \mathcal{U}_{PQ} \\
P_i^{min} \leq P_i \leq P_i^{max} \quad & i \in \mathcal{U}_{PV} \\
Q_i^{min} \leq Q_i \leq Q_i^{max} \quad & i \in \mathcal{U}_{PV} \\
P_{i,j} \leq P_{i,j}^{max} \quad & (i,j) \in \mathcal{I}
\end{aligned} \tag{2.3}$$

where $V_i$, $P_i$ and $Q_i$ are respectively the voltage magnitude, the active power and the reactive power at bus $i$; and $\mathcal{U}_{PQ}$ and $\mathcal{U}_{PV}$ are the set of PQ and PV buses, respectively. $P_{i,j}$ is the active power on the line between buses $i$ and $j$, $P_{i,j}^{max}$ is the flow limit of this line, and $\mathcal{I}$ is the set of all $(i,j)$ for which there is a line connecting bus $i$ to bus $j$. Note that the generator output limit is a physical constraint and cannot be violated at any time. On the other hand, the voltage limit and line flow limits are operating constraints that relate to system reliability, and these may be formulated

as soft constraints.

### 2.4.1 Security Constrained OPF

The first step in SCOPF is to determine the list of contingencies to be considered. The list includes contingencies which are likely to occur and violate at least one of the network constraints. Insignificant or infrequent contingencies are ignored. SCOPF determines the optimal control which minimizes the objective function for the base case and satisfies the power flow feasibility and the network constraints for the base case and each contingency case as expressed in:

$$\begin{array}{ll} min & f(x^{(0)}, u) \\ s.t & \left.\begin{array}{l} g^{(j)}(x^{(j)}, u) = 0 \\ h^{(j)}(x^{(j)}, u) \leq 0 \end{array}\right\} \; j = 0, 1, \cdots, K \end{array} \tag{2.4}$$

where $x^{(j)}$, $g^{(j)}$, and $h^{(j)}$ represent the state, the power flow feasibility, and the network constraints for the contingency case $j$, respectively. $K$ is the size of the contingency list. The pre-contingency or base case is denoted by $j = 0$ as expressed in

$$j = \begin{cases} 0 & \text{base case} \\ 1 \leq k \leq K & \text{contingency case k} \end{cases} \tag{2.5}$$

SCOPF ensures that the system remains in the normal state and does not transition to the emergency state when a contingency occurs. It increases the system security and eliminates the need for remedial action schemes. However, this is achieved with the expense of less economical operation. The additional constraints for the contingency cases reduce the size of the feasible solution space. Therefore, the solution from SCOPF has a higher cost than the one from OPF as illustrated in Fig. 2.3.

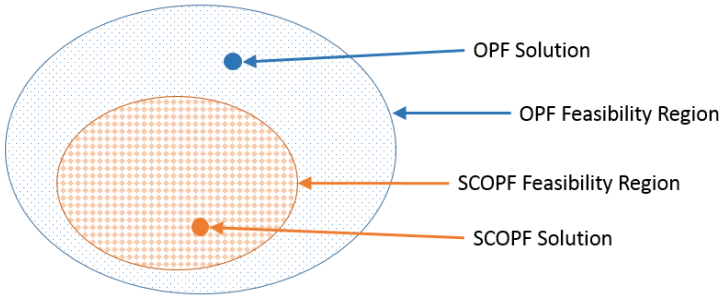


Figure 2.3: Comparison of the SCOPF and OPF solutions.

### 2.4.2 Proposed Resilience-oriented OPF

The optimal power flow is reformulated in the context of security control [76]. This new formulation is termed as the resilience-oriented OPF (ROPF) and recovers the system from the emergency state to the normal state after a contingency. Conventional OPF minimizes the operation cost subject to the power flow and other constraints. When a contingency occurs, retaining system operation becomes the first priority rather than the operation cost. Hence, the objective function of ROPF optimizes the security instead of cost.

Similar to the conventional OPF, the equality constraints of ROPF correspond to the power flow equations and the inequality constraints relate to the generator output limits, voltage constraints, and line flow limits. The voltage constraints and line flow limits may be formulated as soft constraints since they are operating constraints, and unlike the physical constraints, they can be violated. These constraints are modeled by:

$$\begin{aligned} V_i &\leq V_i^{max} + t_i \qquad i \in \mathcal{U}_{PQ} \\ -V_i &\leq -V_i^{min} + r_i \qquad i \in \mathcal{U}_{PQ} \\ P_{i,j} &\leq P_{i,j}^{max} + s_{ij} \qquad (i,j) \in \mathcal{I} \\ 0 &\leq t_i, r_i, s_{ij} \end{aligned} \tag{2.6}$$

where $r_i$ and $t_i$ are respectively the slack variables for the voltage upper and lower limits at bus $i$ and $s_{ij}$ is the slack variable for the line between buses $i$ and $j$. The slack variables are to formulate

the soft constraints and are penalized in the objective function. The objective function enforces the voltage constraints and the line flow limits as expressed in:

$$f(x) = \sum_{i \in \mathcal{U}_{PQ}} \mathcal{V}\bar{V}(2t_i + t_i^2) + \sum_{i \in \mathcal{U}_{PQ}} \mathcal{V}\underline{\mathrm{V}}(2r_i + r_i^2) + \sum_{(i,k) \in \mathcal{I}} \mathcal{V}I(2s_{ik} + s_{ik}^2) \tag{2.7}$$

where $\mathcal{V}\bar{V}$ , $\mathcal{V}\underline{\mathrm{V}}$ and $\mathcal{V}I$ are the weighting parameters chosen with respect to the desired importance of each term.

Solving the proposed ROPF is computationally expensive and might not be practical for a larger system. In the case of a credible contingency, it is crucial to take an effective control action as quickly as possible. Hence, finding a solution that is less accurate, but faster to compute is preferable. Motivated by this, the optimization problem is simplified to reduce the computational complexity. First, the equality constraints associated with the power flow equations are linearized and similar to DC-OPF, DC-ROPF is defined [77]. Second, the inequality constraints associated with the voltage limit are relaxed. The objective function is modified accordingly to exclude the terms associated with the voltage limits:

$$f(x) = \sum_{(i,j) \in \mathcal{I}} (2s_{ij} + s_{ij}^2) - \sum_{i \in \mathcal{N}} u_i \tag{2.8a}$$

$$s.t: \quad P_i^{min} \leq P_i \leq P_i^{max} \quad i \in \mathcal{U}_{PV} \tag{2.8b}$$

$$Q_i^{min} \leq Q_i \leq Q_i^{max} \quad i \in \mathcal{U}_{PV} \tag{2.8c}$$

$$B_{ij}(\theta_i - \theta_j) = P_{ij} \;\; (i,j) \in \mathcal{I} \tag{2.8d}$$

$$\sum_{(i,j) \in \mathcal{I}} P_{ij} - \sum_{(j,i) \in \mathcal{I}} P_{ji} + P_i - D_i + u_i = 0 \quad i \in \mathcal{N} \tag{2.8e}$$

$$0 \leq u_i \leq D_i \qquad i \in \mathcal{N} \tag{2.8f}$$

$$P_{ij} \leq P_{ij}^{max} + s_{ij} \qquad (i,j) \in \mathcal{I} \tag{2.8g}$$

$$0 \leq s_{ij} \tag{2.8h}$$

where $D_i$ is the demand at bus $i$. Constraint (2.8e) relaxes the node balance constraint by allowing

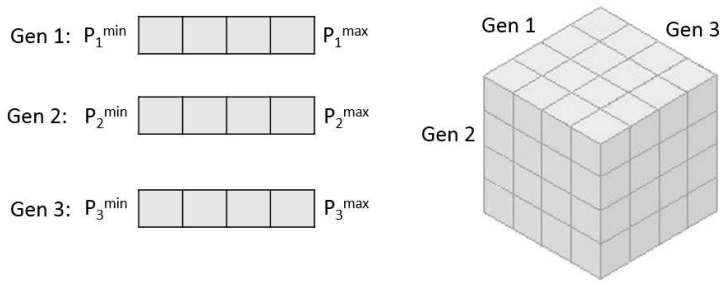


Figure 2.4: Security-compliant generator dispatch subspace synthesis.

partial demand fulfillment at each node. The imbalance between generation and load is allowed by introducing the bounded unmet demand variable (2.8f) at each node and penalizing it in the objective function. This form of ROPF with the voltage constrains excluded is termed as relaxed ROPF throughout the chapter. Numerical results indicate that solving the relaxed ROPF is much faster, yet the solution is as effective as the regular ROPF as will be shown later.

## 2.5 Security-compliant Control Subspace Synthesis

The feasible control subspace of the power system with $n$ generators is discretized into equally distant $n$-dimensional cubes. Each generator's allowed generation dispatch MW range is partitioned by equally spaced points. Consequently, a multi-dimensional mesh grid is constructed that covers all possible combinations of the generator outputs as shown in Fig. 2.4. Each point in the grid corresponds to one control action vector. The power flow is solved for each action and the resultant security constraints are evaluated. The actions that do not violate any constraints are identified as possible RAS solutions.

### 2.5.1 The Proposed Violation Index

It is possible that none of the control actions can satisfy all the security constraints. In that case, the actions that violate fewer constraints and provide a more secure state are selected. A violation index may be defined to speculatively evaluate the resultant security of the system after an action.

Aggregate MVA overload (AMWCO) is introduced in [78] which evaluates the system security based on the total amount of current flow violations,

$$AMWCO = \sum_{(i,j)\in\mathcal{I}} \max\{0, P_{ij}^{(k)} - P_{ij}^{max}\} \tag{2.9}$$

This security index considers only the line flow violations, and excludes the bus voltage or the generator power limits. A security index is defined to account for these constraints,

$$Violation^{(k)} = w_I S_I^{(k)} + w_V S_V^{(k)} + w_P S_P^{(k)} + w_Q S_Q^{(k)} \tag{2.10}$$

where $S_I^{(k)}$, $S_V^{(k)}$, $S_P^{(k)}$, and $S_Q^{(k)}$ are respectively the security indices of the line flows, bus voltages, generator active power and reactive power for action $k$. The terms $w_I$, $w_V$, $w_P$ and $w_Q$ are their corresponding weights which capture varying importance of different violation type. The security index for the line flows is given by

$$S_I^{(k)} = \sum_{(i,j)\in\mathcal{I}} \frac{\max\{0, P_{ij}^{(k)} - P_{ij}^{max}\}}{P_{ij}^{max}} \tag{2.11}$$

This is similar to the aggregate MVA overload in (2.9) except that the MVA overloads are normalized by the line flow limits. The violation index for bus voltage, and generator limits are defined similarly as the aggregate violations normalized by their upper bound limits.

The importance of using the normalization terms and the weights $w$ can be demonstrated through an example. Consider two constraint violations: The first violation is on a bus with voltage of $V_i = 1.5$ p.u. and maximum permissible voltage of $V_i^{max} = 1.05$ p.u. The second violation is on a line with $P_{jk} = 800$ MW active power which has a MW limit of $P_{jk}^{max} = 400$ MW. The amount of violation is $(V_i - V_i^{max}) = 0.45$ and $P_{jk} - P_{jk}^{max} = 400$ for the second one. The first violation is more severe than the second one, yet its amount is much smaller. Normalizing the violation amount by its upper bound limit results in 0.43 for the first violation and 1 for the second one. The violation of voltage constraint is more significant than line flow constraint violation of the same percentage. Hence, higher weight is assigned to the voltage constraint in order to capture its significance. Considering the weights of $w_V = 1$ and $w_I = 0.05$ results in 0.43 for the first

violation and 0.05 for the second one. Now, the terms corresponding to each constraint which appear in the violation index reflect their actual importance to the system security. The current framework considers a rather heuristic approach for assigning the proper weights. Developing a systematic approach for calculating the weights will be an interesting future study.

### 2.5.2 The Performance Improvements

The computational complexity of the control subspace synthesis algorithm is $\mathcal{O}(R^n)$, where $R$ is the discretization granularity for the individual generators, $n$ is the number of generators that can participate in the dispatch, and $\mathcal{O}()$ is the big O time complexity notation. The complexity is exponential in the number of participating generators. For a large system with many generators, the exponential time complexity will be burdensome or even impossible. One approach is to reduce the number of participating generators. Individual generators may have varying impact on the overall system security with some generators being crucial and others being less significant. Excluding less significant generators from the search reduces the number of safe/safer actions considered, while still providing enough candidates to keep the performance near optimal. This will be demonstrated through case studies later in this chapter.

We employ a greedy algorithm to identify the insignificant set of generators to be excluded from the search procedure. For every contingency, the lines and buses at which the constraints are violated are identified. Based on empirical analyses, we observe the identified lines and buses are often clustered at one or multiple locations in the network. The generators close to the areas under stress are classified as crucial and the ones which are further away are labeled as insignificant. The most critical generators are determined in the first level of the algorithm. The less critical generators are determined in subsequent levels of the algorithm. The levels are executed consecutively until the number of critical generators reaches a user-specified value. Algorithm 1 describes more precisely how our framework identifies the critical generators with varying level of importance. In the Algorithm, $\mathcal{U}^k_{Critbus}$ and $\mathcal{U}^k_{Critbus}$ are respectively the set of critical buses and critical generators at level $k$, $CritGenMax$ is the maximum number of critical generators defined by the user and $Size(x)$ returns the size of the set $x$.

We demonstrate the effectiveness of this technique on case studies later in this chapter. While

**Algorithm 1** Critical Generator Identification (CGI)

**procedure** CGI(Network State and Limits)
  $\mathcal{U}^1_{Critbus}$ = Set of busses with Violations
  $\mathcal{U}^1_{Critgen} = \mathcal{U}_{PV} \cap \mathcal{U}^1_{Critbus}$
  $k = 1$
  **while** $Size(\mathcal{U}^k_{Critgen}) < CritgenMax$ **do**
    $\mathcal{U}^k_{Critbus} = \mathcal{U}^{k-1}_{Critbus} \cup N(\mathcal{U}^{k-1}_{Critbus})$
    $\mathcal{U}^k_{CritGen} = \mathcal{U}^{k-1}_{CritGen} \cup (\mathcal{U}_{PV} \cap \mathcal{U}^k_{Critbus})$
    $k = k + 1$
  **end while**
**end procedure**

this is a heuristic technique, it gives very promising results based on our experimentation. We consider development of a systematic and efficient approach with theoretical guarantees to identify the truly-optimal set of crucial generators as a future study.

A second approach for reducing the computational complexity is to exclude some of the non-promising candidates based on the power losses in the system. For each candidate generation dispatch, the total load is fixed, the real output power of all the generators except for the slack bus is known and the real power at the slack generator is limited by its output power bounds. Motivated by this, the mismatch between the total generation and load may be used as a criteria to reduce the size of the search space:

$$P^{min}_{slack} - \delta \leq (P_{Load} - \sum_{i \in \mathcal{U}_{PV}} P_i) \simeq P_{slack} \leq P^{max}_{slack} + \delta \tag{2.12}$$

where $P_{Load}$ is the total load in the system, $P_{slack}$ is the MW output of the slack generator, $P^{max}_{slack}$ and $P^{min}_{slack}$ are respectively the upper and lower bounds of the slack generator's MW output and $\delta$ is the margin of error. The control subspace synthesis with all the combinations for all the generators is referred to as full exhaustive search and the one with only the critical generators and the system loss filtering is termed as the selective search throughout the chapter.

The computation time can be further reduced through using DCPF instead of AC power flow to get the system states for each possible action. Since the DCPF solution is not accurate, it could be used as a fast screening tool before detailed ACPF analysis is performed on the top candidates. The violation index of all the candidate action is calculated based on their DCPF solutions and the

Table 2.1: Comparison of the ROPF Methods for the 24-bus System

| Scenario | Number of Violations | | | AMWCO | Violation Index | Time (sec) |
|---|---|---|---|---|---|---|
| | Gen MW | Voltage | Line Flow | | | |
| No Action | 0 | 7 | 3 | 2.3507 | 0.2183 | - |
| ROPF | 0 | 2 | 0 | 0 | 0.021 | 338.11 |
| Relaxed ROPF | 0 | 2 | 0 | 0 | 0.0246 | 36.87 |
| Relaxed DC-ROPF | 0 | 2 | 1 | 1.1621 | 0.0256 | 9.1946 |

top candidates are selected. AC power flow is solved for only the top candidates; the exact value of their violation indices are obtained and the best action is obtained accordingly.

## 2.6 Simulation and Numerical Results

The performance of the proposed algorithm is evaluated through simulation. The IEEE 24-bus system and the IEEE 118-bus [55] are considered, contingencies are applied to these systems, and effective RAS actions are designed to maintain their security.

First, contingency analysis is performed on the 24-bus system. Figure 2.5 illustrates the number of violations and the violation index as broken down by type for all the single and double generator outage contingencies. It is observed that voltage violations contribute the most to the violation index. The generator outage at bus 23 has the highest violation index among all the single outages and hence is selected as the most credible one for further analysis. The power flow is solved for this contingency case and the security constraints are evaluated. It is observed that this contingency violates seven voltage constraints and three line flow constraints. The violation index of the system prior to any control action is $0.2181$ as calculated by (2.10). The assumed weights for the violation index are $w_V = 1$, $w_P = w_Q = 100$ and $w_I = 0.05$. This selection captures the lower sensitivity of the system security to the percentage violation of line flow limits compared to voltage constraints. The motivation for using high weights for the generator limits is that satisfying physical constraints is more important than satisfying operating constraints.

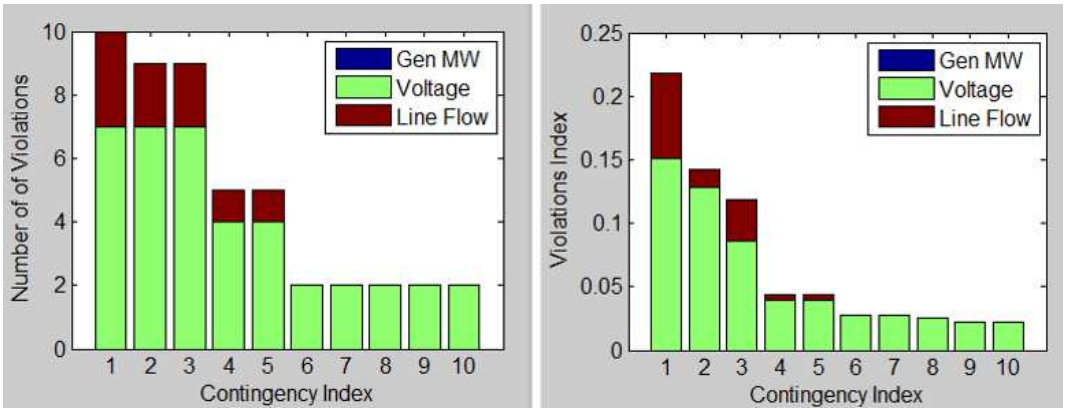


(a)

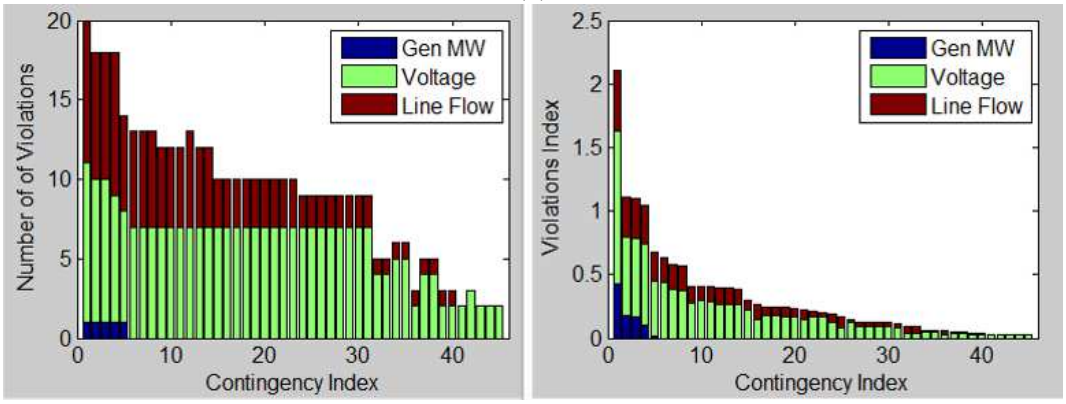


(b)

Figure 2.5: Contingency analysis of the 24-bus system: (a) single generator outage, (b) double generator outage.

The optimal generation redispatch is obtained through solving ROPF as presented in Table 2.1. The weights of the objective function in ROPF are selected based on the weights of the violation index to have a peer comparison between the two methods, i.e. $\mathcal{V}\bar{V} = \mathcal{V}\underline{\mathrm{V}} = w_V = 1$ and $\mathcal{V}I = w_I = 0.05$. The security index is reduced from .218 to 0.021. The computation time is 338.11s, which is significantly high even though the system is small. The computation time can be reduced to 36.8s by relaxing the voltage constraints. Linearizing the power flow equations through relaxed DC-ROPF can further reduce the running time to only 9.11s. The security index stays almost the same for the faster solutions. For reference, AMWCO is also included in the table.

Next, the performance of the control subspace synthesis in finding the best generation redispatch is evaluated. The permissible MW output of each generator is divided into four equal intervals,

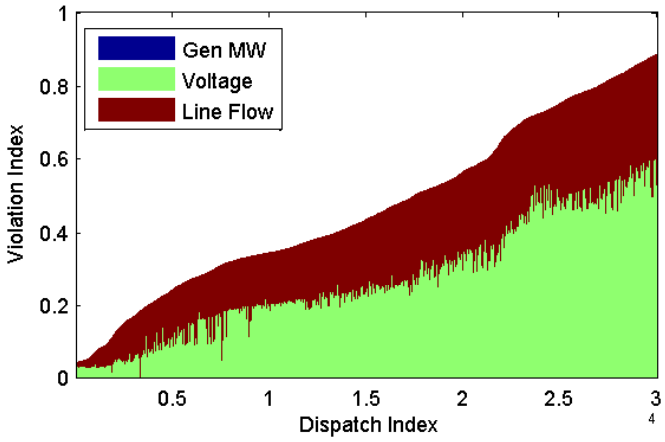


Figure 2.6: Violation indices of the first 30K dispatches (top 11%).

and the possible dispatch scenarios are generated by constructing a multi-dimensional grid of these intervals. The system has 11 generators, where the generator at bus 1 is the slack bus and the generator at bus 23 is out because of the contingency. The security constraints are evaluated for each dispatch, and it is observed that none of the dispatches can satisfy all the constraints. The violation index is used to quantify the security provided by each dispatch and obtain the best action accordingly.

The dispatches are sorted based on their violation indices in descending order. The violation indices of the first 30K dispatches and the types of violations are illustrated in Fig. 2.6. The horizontal axis legends are shown using the scientific notation ($\times 10^4$). The dispatch index denotes its rank in the sorted dispatch list. None of the generator reactive power constraints are violated in any of the dispatches and hence their contributions are excluded. The top three generation dispatches and their corresponding violation indices are presented in 2.2. For reference, the generator dispatch before taking any action is also included. The candidate actions improve the system security significantly as the violation index is reduced from 0.218 to 0.0414. 2.7 illustrates the number of constraint violations for the top 30K dispatches in the sorted list as it is broken down into different violation types.

The generator dispatches for the top 100 actions are analyzed to obtain their statistics and distribution information. 2.8 illustrates the histogram of the number of times that the dispatch of each

Table 2.2: Top Three Dispatches by the Exhaustive Search

| Gen Number | No Action | Generation Redispatch | | |
|---|---|---|---|---|
| | | Action 1 | Action 2 | Action 3 |
| 1 | 0.3637 | 1.06 | 1.07 | 1.07 |
| 2 | 1.37 | 3.33 | 3.33 | 3.33 |
| 7 | 2.72 | 3.33 | 3.33 | 3.33 |
| 13 | 4.64 | 6.67 | 6.67 | 6.67 |
| 14 | 0 | 3.33 | 3.33 | 3.33 |
| 15 | 1.4 | 3.33 | 3.33 | 6.67 |
| 16 | 1.4 | 3.33 | 0.00 | 0.00 |
| 18 | 3.63 | 0.00 | 3.33 | 3.33 |
| 21 | 3.63 | 3.33 | 3.33 | 0.00 |
| 22 | 2.72 | 0.00 | 0.00 | 0.00 |
| Violation Index | 0.2183 | 0.0414 | 0.0416 | 0.0417 |

Table 2.3: Critical Generator Identification (CGI)

| CGI Level | Critical Generators |
|---|---|
| Level 1 | 2 |
| Level 2 | 7 |
| Level 3 | 13,14,15 |
| Insignificant Generators | 16,18,21,22 |

generator was in any of the intervals. We observe that the dispatch of some generators is always within only one or two intervals; e.g., Gen 2 dispatch is always at the first and second interval and Gen 7 dispatch is mostly at the second interval. In contrast, the dispatch of some generators like Gen 16, Gen 18, Gen 21 and Gen 22 falls within all intervals. This suggests that the dispatches of these generators are relatively insignificant to the system security and could be excluded from the exhaustive search for faster computation, as discussed below.

The computation time may be reduced by narrowing down the search space through selective search. The critical generators are identified using the proposed algorithm (Table 2.3). The most critical generators are Gen 2 and Gen 7 that are identified in the first and second levels of the algorithm, while Gen 13, Gen 14, and Gen 15 are identified as third order critical generators. The

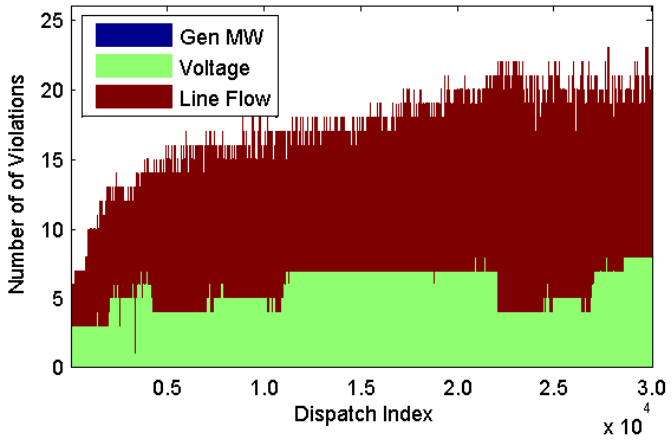


Figure 2.7: Number of violations for the first 30K dispatches (top 11%).

remaining generators, Gen 18, 21, 22, and 23, are labeled as insignificant.

Figure 2.9 shows the line flows and the voltage profile of the system after the contingency. The line flows are visualized through the pie charts on the lines and the voltage profile through the contour plot. The figure shows the stressed area, where the overloaded lines and under voltage buses are located. Gen 2 and Gen 7 are the closest to the stressed area as correctly identified in the first and second level of Critical Generator Identification (CGI); Gen 13, Gen 14 and Gen 15 are in the second order neighborhood, and the remaining generators are far enough to be excluded from the exhaustive search. These results are consistent with the earlier observation of the dispatch distributions from Fig. 2.8. The dispatch of the critical generators among the top 100 actions is within only a few intervals, whereas the dispatch of the insignificant ones is distributed between all the intervals.

Once the critical generators are determined, the MW outputs of the four insignificant generators are fixed to their default values and the selective search is performed on the five critical generators. This reduces the number of combinations significantly, i.e., $4^9/4^5 = 256$ times. The number of combinations can be further decreased by considering the mismatch between the total load and generation for each action and excluding the non-promising ones. The $4^5 = 1024$ combinations from the critical generators are sorted based on their violation index in descending order. The mismatch between the total generators MW output (excluding the slack generator) and the total

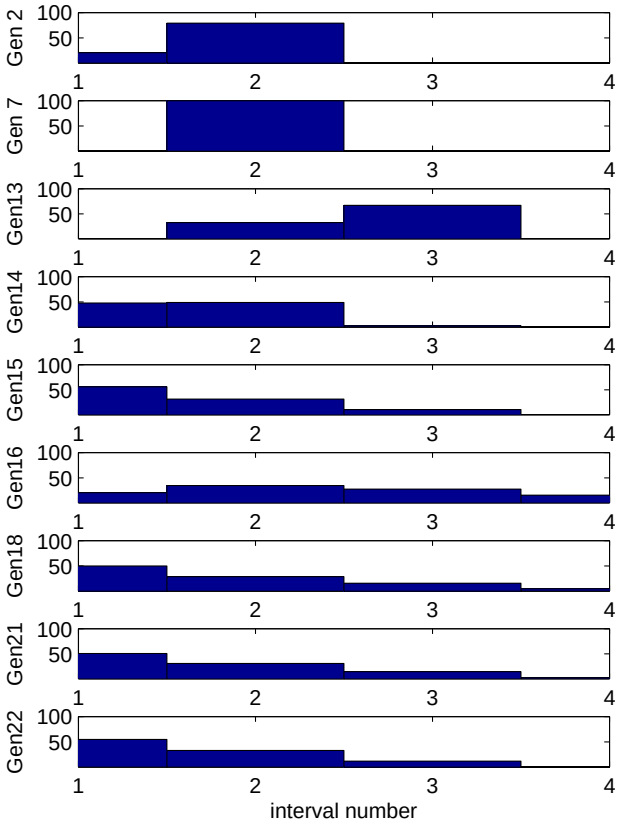


Figure 2.8: Distribution of the generators' dispatches among the top 100 actions. The dispatch of the critical generators is within only a few intervals, whereas the dispatch of the insignificant ones is distributed between all the intervals.

load for the first 800 dispatches in the sorted list are illustrated in Fig. 2.10. The mismatch falls within the range specified by (2.12) for the top 27% candidates (first 178 dispatches). Hence, using the load/generation mismatch as a criteria to eliminate non-promising candidates can reduce the number of candidates by an extra 70% without compromising the performance.

The performance of the selective search relies on the correct identification of the critical generators. To demonstrate this, the participating generators are selected randomly as opposed to using the CGI algorithm. Table 2.4 presents the comparison between different control subspace methods. Five scenarios are considered:

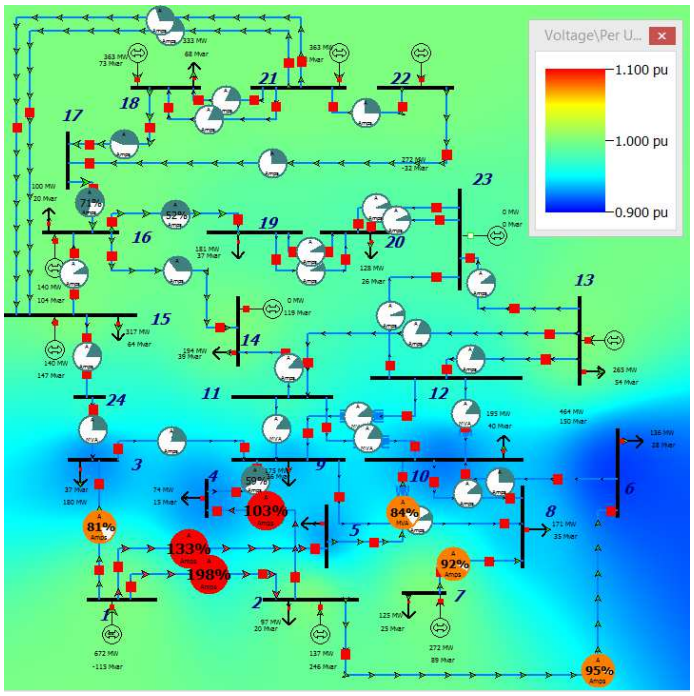


Figure 2.9: Visualization of the constraint violations for the 24-bus system: The pie charts visualize the line flows with red denoting violations. The contour plot visualizes the voltage profile with the blue areas illustrating violations.

1. *Full Search:* All the possible combination of generation redispatches are considered.

2. *Selective Search:* Only the critical generators are included and the search is narrowed based on the system losses.

3. *Naive Search:* The generators that participate in RAS are selected randomly and the search is narrowed based on the system losses.

4. *Selective search with DCPF:* DCPF is used in the selective search for solving power flow

5. *Naive search with DCPF:* DCPF is used in the naive search for solving power flow.

The running time of the full search is extremely high (10085s), which makes it impractical for online RAS applications. The selective search provides the same performance as the full search with much lower computation time (only 0.09% of the full search running time). The violation index obtained from the naïve search is much higher than the smart search, which validates the

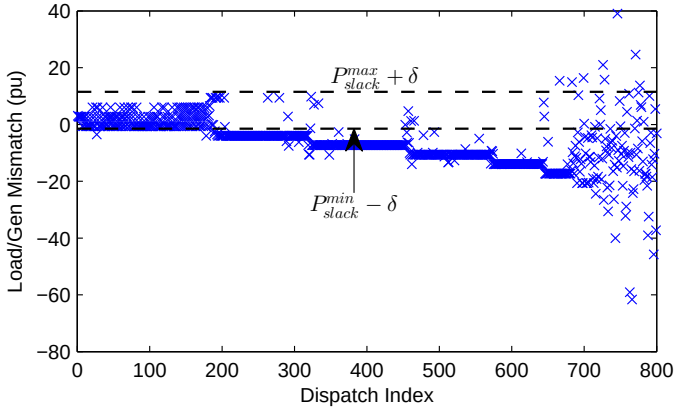


Figure 2.10: Mismatch between the total load and generation for the first 800 dispatches when only the critical generators are included in the exhaustive search.

effectiveness of the CGI algorithm. Using DCPF in the smart search reduces the running time by an order of ten, yet it compromises the performance. This suggests avoiding DCPF in the smart search when the system is small and AC power flow can be solved in reasonable time. Comparing the results of Table 2.1 and 2.4, it is observed that relaxed DC-ROPF and smart search have equally good performance with equally low running time.

Next, the performance of the proposed algorithms on the IEEE 118-bus case is evaluated. Figure 2.11 illustrates the number of violations and the violation index for single and double generator outage contingencies. Double generator outage is considered only among the nine largest generators in the system. The interesting observation is that most of the violations are line flow violations for this system whereas voltage violations are more frequent for the 24-bus system (see Fig. 2.5). The generator outage at bus 69 has the second highest violation index among all the single outages and is selected for further analysis. Different methods are used to find the best generation redispatch for this contingency, as presented in Table 2.5. Prior to any actions, the system has two voltage violations and 17 current violations with violation index equal to 2.428. Relaxed DC-ROPF can reduce the violation index to only 0.082, yet its running time is quite high (1452 sec). Smart search provides a relatively good violation index (0.527) with much lower computation time (282.96 sec). Using DCPF in the smart search reduces the running time by an order of 10 while providing the same violation index.

Table 2.4: Comparison of the Control Subspace Synthesis Methods for the 24 bus System

| Scenario | Number of Violations | | | AMWCO | Violation Index | Time (sec) |
|---|---|---|---|---|---|---|
| | Gen MW | Voltage | Line Flow | | | |
| No Action | 0 | 7 | 3 | 2.3507 | 0.2183 | - |
| Full Search | 0 | 3 | 1 | 0.3812 | 0.0414 | 10085 |
| Smart Search | 0 | 5 | 2 | 0.5486 | 0.058 | 9.44 |
| Smart Search with DCPF | 0 | 6 | 1 | 0.3944 | 0.1284 | 0.934 |
| Naive Search | 1 | 10 | 7 | 0.5486 | 5.0494 | 12.8 |
| Naive Search with DCPF | 1 | 8 | 2 | 0.5032 | 5.968 | 0.9212 |

Recall that using DCPF for the 24 bus system compromised the violation index. Linearizing the power flow equations through DCPF has varying impact on different systems depending on how inductive the transmission lines are, the system voltage profile, etc. The effect of using DCPF on the smart search performance depends on similar characteristics of the system. It also depends on the type of post-contingency violations. For example, if the post-contingency violations are mostly line flow violations (e.g. the 118bus system), using DCPF in the smart search would be effective since DCPF captures the coupling between the generation redispatch and the line flows. On the other hand, if the violations are mostly voltage violations (e.g. the 24-bus case), using DCPF in the smart search jeopardizes the performance since there is no coupling between the voltages and the generator MW outputs in DCPF. Further exploration into the application of DCPF in the smart search and its effect on the performance will be an interesting future study.

All the credible single generator outages are considered for the 118-bus system, and the smart search with DCPF is used to improve the system security. In this study, a contingency is considered credible when the post-contingency violation index exceeds 0.1. The violation index before taking any action is compared with the one from the smart search in Fig. 2.12. It is observed that the smart search successfully protects the network from all the credible contingencies.

The last system to study is the Texas 2000-bus synthetic case with the one-line diagram shown in Fig. 2.13 [55, 79]. The system has eight geographic areas which are color-coded in the one-line

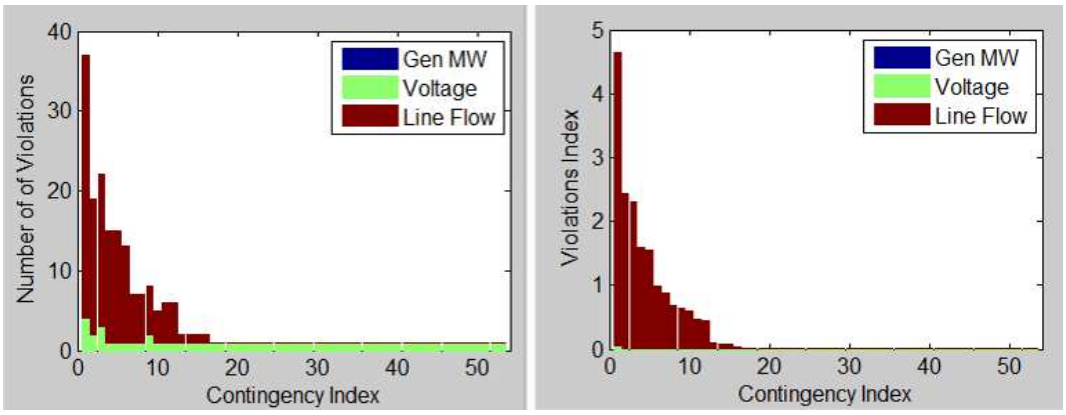


(a)

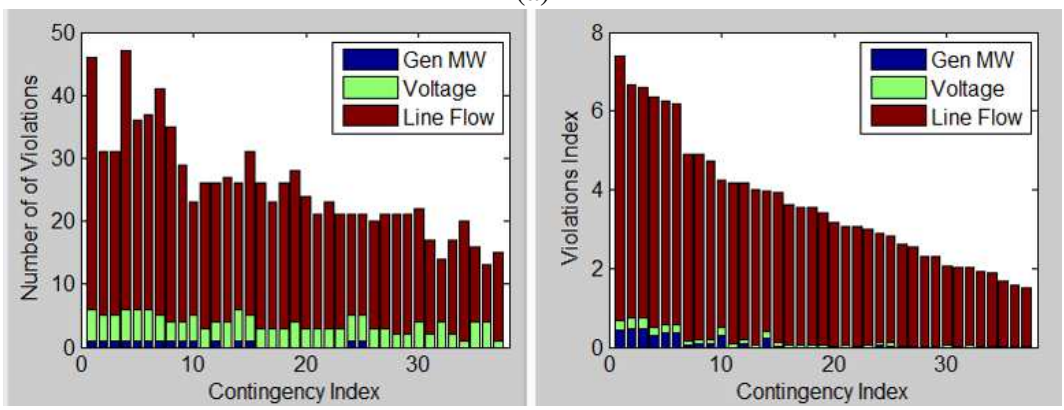


(b)

Figure 2.11: Contingency analysis for the 118-bus system: (a) single generator outage, (b) double generator outage.

diagram; red lines are 345 kV and black lines are 115 kV. Figure 2.14 illustrates the number of violations and violation index for the single and double generator outages. The single outage is performed only on the first 24 largest generators and the double outage only among the first seven largest generators. Gen MW contributes the most to the violation index for this system, unlike the 24-bus and the 118-bus which had voltage violations and line flow violations as the dominant violation type, respectively. All the single generator outages for this system have very low violation index (smaller than 0.8). Hence, the most credible double generator outage is selected for further analysis, i.e. generator outages at buses 1593 and 1735. Table 2.6 presents the performance of the smart search with DCPF in finding the best generation redispatch. Prior to any action, the violation index is 4.7 with three generator MW violations, 94 voltage violations and 22 line flow

Table 2.5: Method Comparison for the 118-bus System

| Scenario | Number of Violations | | | AMWCO | Violation Index | Time (sec) |
|---|---|---|---|---|---|---|
| | Gen MW | Voltage | Line Flow | | | |
| No Action | 0 | 2 | 17 | 9.79 | 2.428 | - |
| Relaxed DC-ROPF | 8 | 1 | 0 | 0 | 0.0825 | 1452 |
| Smart Search | 0 | 3 | 12 | 0.0403 | 0.5274 | 282.96 |
| Smart Search with DCPF | 0 | 3 | 12 | 2.066 | 0.527 | 28.59 |
| Naive Search with DCPF | 1 | 1 | 3 | | 4.246 | 193.9 |

Table 2.6: Generation Redispatch for the 2000-bus System

| Scenario | Number of Violations | | | Violation Index | Time (sec) |
|---|---|---|---|---|---|
| | Gen MW | Voltage | Line Flow | | |
| No Action | 3 | 94 | 22 | 4.70 | - |
| Smart Search with DCPF | 2 | 2 | 1 | 0.63 | 242.9 |

violations. The generation redispatch reduces the violation index to 0.63 with only two Gen MW violations, two voltage violations, and one line flow violation. The algorithm considers eight critical generators with five intervals for each generator. It is important to use DCPF for this system instead of ACPF due to its large size. The running time of solving ACPF is 5.05 seconds while the DCPF running time is only 0.067. The performance of ROPF is not tested on this system because of its computational complexity limitations.

## 2.7 Conclusion

In this chapter, we developed a design procedure for remedial action schemes (RAS) which improves the security of the power system against credible contingencies. Resilience-oriented OPF and security-compliant control subspace synthesis are proposed as two generation redispatch tech-

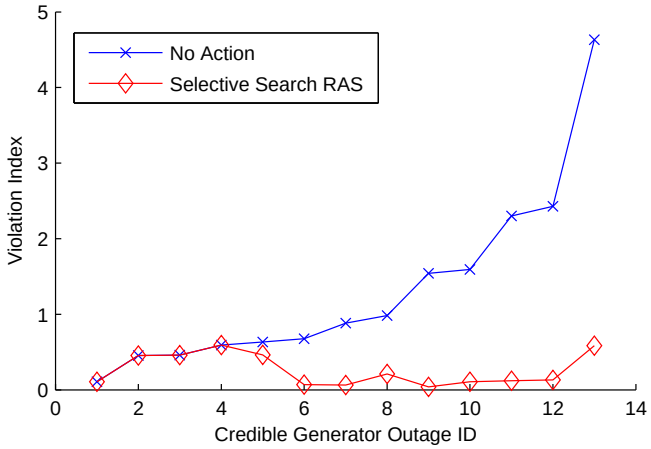


Figure 2.12: Performance of the smart search with DCPF in improving the system security during the credible generator outages of the 118 bus system.

niques that have low computational complexity and are suitable for online RAS applications. Numerical results on the small IEEE 24-bus test case indicate that both methods provide sufficient security for the system with reasonable running time. For a larger case like the IEEE 118-bus system, ROPF offers extremely good security, yet the running time is quite high for online applications. On the other hand, the greedy algorithm offers a solution that is less secure, but much faster to compute. This chapter addresses the trade-off between the security and the computational complexity of the generation redispatch techniques and allows the system operator to select the best technique based on the size of the system, the required security measures, and etc.

The chapter suggests several opportunities for future research. First, the proposed control subspace synthesis focuses on the generation redispatch as the control action. Future research can extend this framework to other control actions such as topology control. Second, the algorithm for critical generators identification may be further improved through controllability analysis and the use of control support groups identified via sensitivity analysis and clustering techniques.

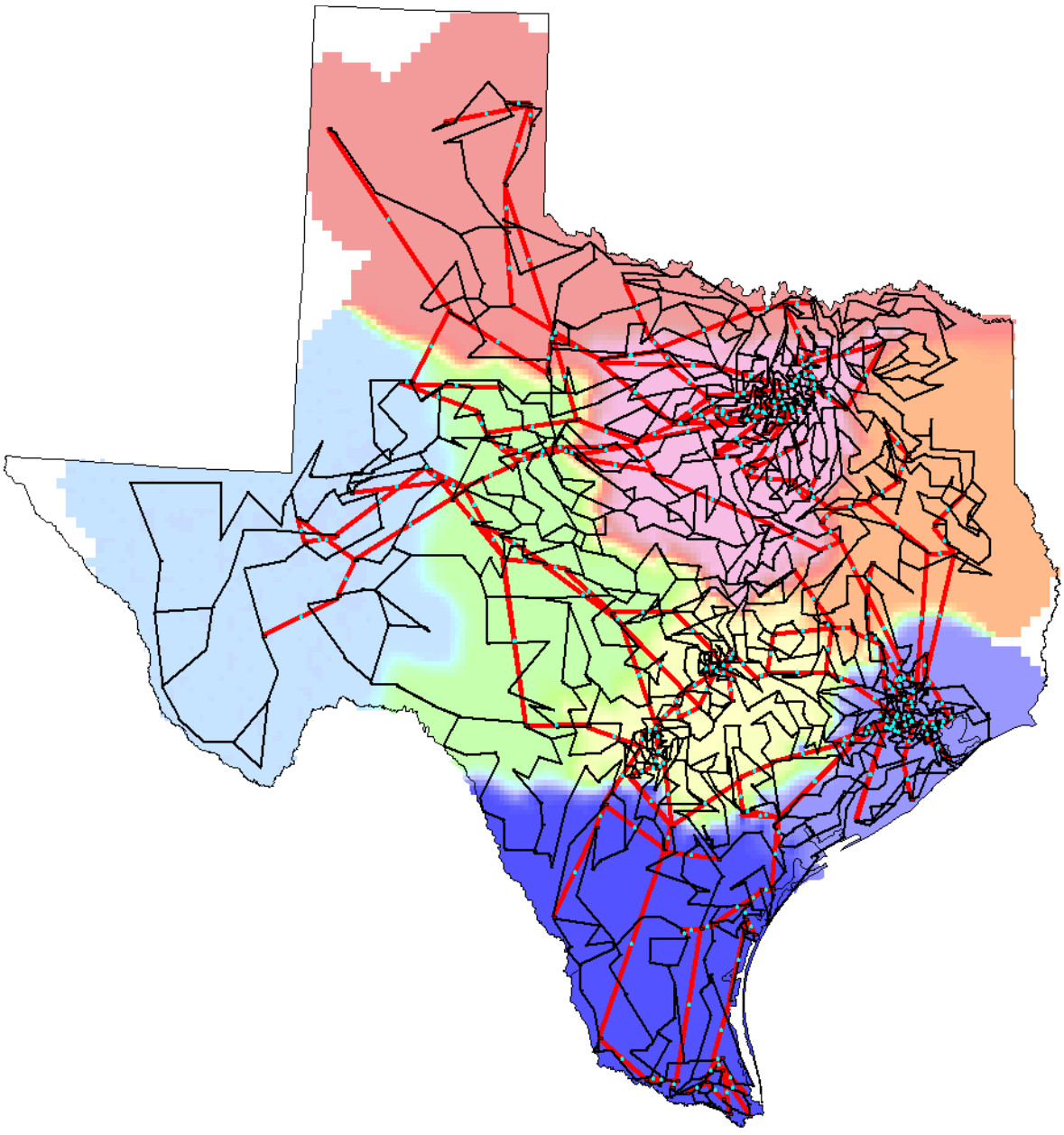

Figure 2.13: One-line diagram of the Texas 2000-bus System. (a) Eight geographic areas are color-coded. (b) Red lines are 345 kV and black lines are 115 kV.

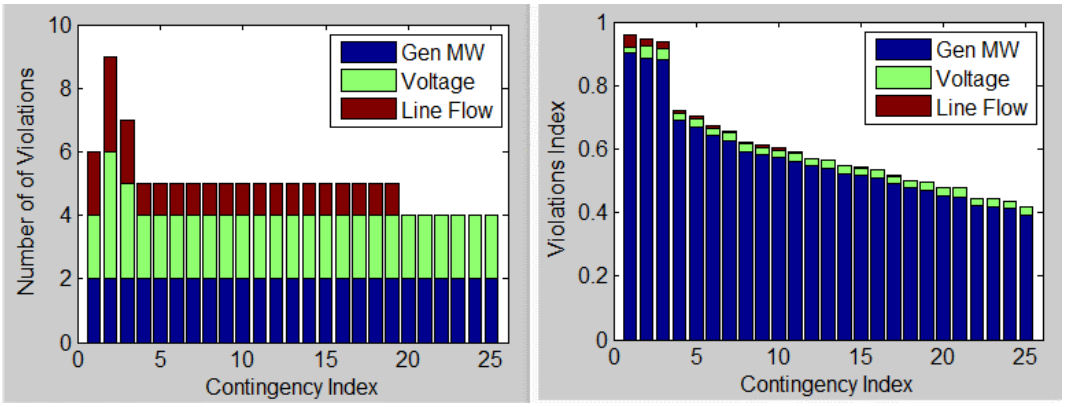


(a)

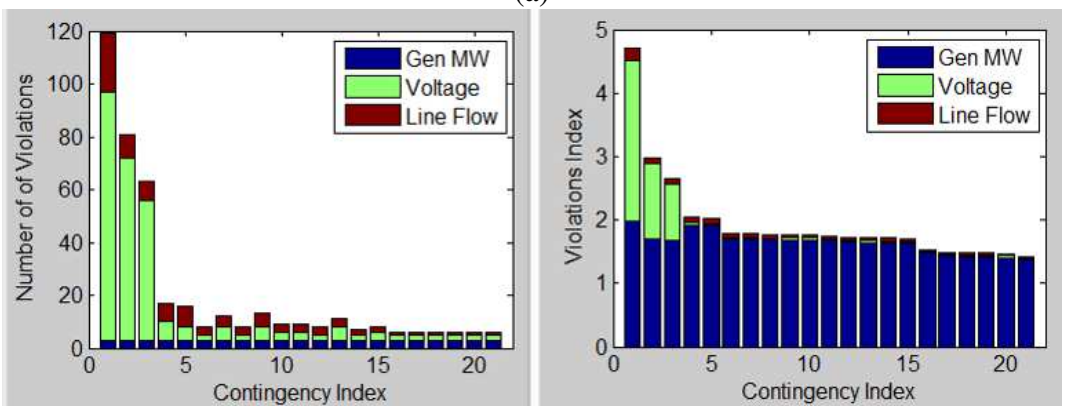


(b)

Figure 2.14: Contingency analysis for the Texas 2000-bus system: (a) single generator outage, (b) double generator outage.

# CHAPTER 3

# BACKGROUND ON GMD MODELING

This chapter provides detailed background on GICs, their negative impacts and the fundamentals of their modeling. The chapter is organized as follows: Section 3.1 provides some background on GMDs. A linear model is presented in Section 3.2 which relates the GICs on transformer neutrals to E-field through network topology and conductances. In Section 3.3, the relation between the magnetic field and the E-field is fully described and the estimation of E-field from the magnetic data is presented. Section 3.4 explains how to estimate the electric field from the GIC measurements.

## 3.1 Background on Geomagnetic Disturbances

The GICs passing through transformer windings create DC flux in the core of power transformers which shifts the operating point of their magnetizing characteristics. With the DC offset, the magnetic flux reaches the saturation level during half of the 60-Hz cycle and the magnetizing current increases dramatically as shown in Fig. 3.1. This phenomenon is usually referred to as half-cycle saturation and happens very frequently during GMD events [21, 36].

Half-cycle saturation increases the transformer reactive power loss significantly. Unless sufficient reactive power support is provided to compensate for these losses, the lack of reactive power in the network may lead to voltage instability and possibly system collapse [37, 80, 33].

Half-cycle saturation increases harmonic currents which in turn increase the eddy current loss and core loss in some components, e.g. transformers and generators. The additional loss results in their heating and may cause major damages. Moreover, harmonic currents can affect the performance of the protection systems. Many of the conventional protection devices such as the electromechanical relays are sensitive to the current harmonics and are susceptible to misoperation

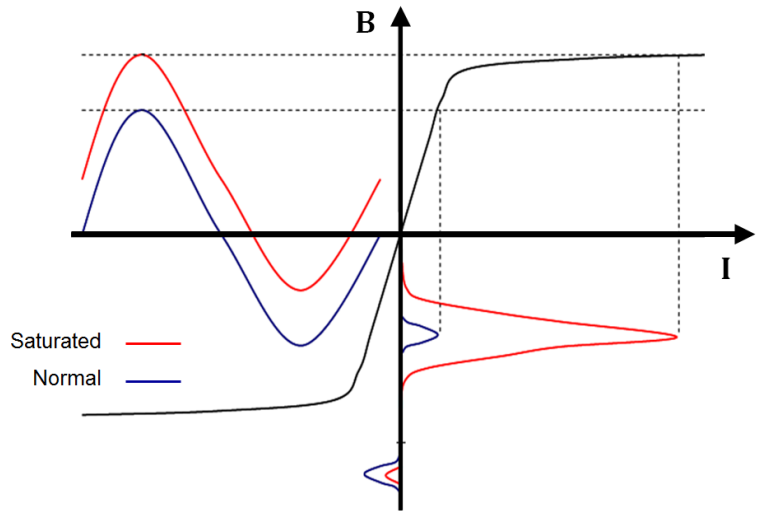


Figure 3.1: Transformer's half-cycle saturation caused by GICs.

during GMD events. Malfunction of the protection devices during GMD events isolates the capacitor banks and static VAR compensators (SVCs) at the time when their reactive power support is highly needed. This moves the network further to the margins of voltage instability.

The 1989 Hydro-Québec blackout demonstrates the significance of GMDs and their potential impacts on the power grid. On March 13, 1989, Hydro-Québec network with 21,500 MW generation and 2,000 kilometers of power lines went down for nine hours and caused tens of millions of dollars damage to the utility and the costumers. The major cause of the Hydro-Québec blackout is reported to be the unintended tripping of seven SVCs which initiated a series of events leading to voltage instability and eventually system collapse. The protection devices which tripped these SVCs were sensitive to the current harmonics produced by half-cycle saturation and malfunctioned. After the SVCs were tripped, part of the generation units with 9.5 GW capacity went down, even though the reason for their disconnection is not clear yet. This generation loss resulted in severe voltage and frequency drop in the rest of the network. Consequently, the rest of the generation units were disconnected, and ultimately the entire network collapsed due to voltage and frequency instabilities [10].

Considering the negative impacts of GICs on power system, proper mitigation programs are required to protect the system. GMD risk management evaluates the vulnerability of the network to potential GMD events. In GMD risk management, the potential GMD events that may affect

the network are studied and the probabilities of their occurrence are considered. For each potential GMD, the impacts on the power system are assessed and the potential damages and costs are estimated. Finally, effective operating procedures are developed which minimize the storm impacts as well as the mitigation costs.

Reducing the GICs through GIC blocking devices is also an important part of the GIC mitigation program. Neutral current blocking devices are the neutral resistors or capacitors which are placed at the neutral-to-ground connection of the transformers. These devices reduce the GIC passing through the transformer by increasing the resistance of the GIC loop. Series capacitors are also considered as GIC blocking devices although their main purpose is system stability rather than GIC reduction. Note that the placement of GIC blocking devices is a very challenging task and requires careful study on the network topology and equipment configuration. Improper placement of the blocking devices may block the GIC in one line and direct it to some other line which is already under stress by GICs.

## 3.2 GIC Modeling

Within the footprint of an interconnected power system, the geoelectric field is often assumed to be uniform as represented by $\mathbf{E} := [E^N,\ E^E]^T$, with $E^N$ and $E^E$ denoting its Northward and Eastward components, respectively.

To this end, consider a transmission network with the set of buses $\mathcal{N}^B$ and the set of substations $\mathcal{N}^S$, which together form the set of nodes $\mathcal{N} := \{1, \ldots, N\} = \mathcal{N}^B \bigcup \mathcal{N}^S$. As all the generators are grounded via the nearest substation, the buses directly connected to generators can be excluded from $\mathcal{N}^B$ in the GIC modeling. Furthermore, the node connectivity can be represented by the set of edges $\mathcal{E} := \{(n, m)\} \subseteq \mathcal{N} \times \mathcal{N}$, which includes the set of transmission lines $\mathcal{L} := \{(n, m)\} \subseteq \mathcal{N}^B \times \mathcal{N}^B$, as well as the pairs $(n, m)$ if and only if substation $n$ is directly connected to bus $m$ by a transformer. For any $(n, m) \in \mathcal{E}$, let $g_{nm} = g_{mn}$ denote the equivalent conductance between $n$ and $m$, which will be the transmission line conductance if $(n, m) \in \mathcal{L}$. Otherwise if $n \in \mathcal{N}^S$ and $m \in \mathcal{N}^B$, $g_{nm}$ corresponds to the conductance due to transformer windings to the substation neutral and autotransformers' series and common windings. Similarly, let $g_{nn}$ represent the grounding

conductance of the substation neutral for $n \in \mathcal{N}^S$. Notice all the conductance quantities have accounted for the three phases in parallel. With these notations, an $N \times N$ real symmetric matrix $\mathbf{G}$ can be constructed with nonzeros only at its diagonal and entries corresponding to $\mathcal{E}$, with the $(n, m)$-th entry given by

$$G_{nm} := \begin{cases} -g_{nm}, & \text{if } (n,m) \in \mathcal{E} \\ \sum_{\nu \in \mathcal{N}_n} g_{n\nu}, & \text{if } n = m \in \mathcal{N}^B \\ g_{nn} + \sum_{\nu \in \mathcal{N}_n} g_{n\nu}, & \text{if } n = m \in \mathcal{N}^S \\ 0, & \text{otherwise.} \end{cases} \tag{3.1}$$

The conductance matrix $\mathbf{G}$ serves as the counterpart of the bus admittance matrix for ac power network analysis, as detailed soon.

### 3.2.1 Input Voltages as Current Injections

The input of GIC modeling is the aforementioned induced voltage along the transmission lines. The effect of geoelectric field on the line $(n, m) \in \mathcal{L}$ is equivalent to having a dc voltage source in series with that line, with the voltage level given by

$$U_{nm} = E^N L^N_{nm} + E^E L^E_{nm} \tag{3.2}$$

where $L^N_{nm}$ and $L^E_{nm}$ denote the northward and eastward distance for line $(n, m)$. Using the Norton equivalent, all the induced voltage sources can be converted to dc current injection to every bus $n$, as given by

$$I_n = \sum_{(n,m)\in\mathcal{L}} I_{nm} = \sum_{(n,m)\in\mathcal{L}} \left( L^N_{nm} g_{nm} E^N + L^E_{nm} g_{nm} E^E \right) \tag{3.3}$$

$$I^{inj}_n = \sum_{(n,m)} I^{inj}_{nm} = \sum_{(n,m)} g_{nm} U_{nm} = \Big( \sum_{(n,m)\in\mathcal{L}} L^N_{nm} g_{nm} \Big) E^N + \Big( \sum_{(n,m)\in\mathcal{L}} L^E_{nm} g_{nm} \Big) E^E \tag{3.4}$$

where the second equality follows by substituting (3.2) and (3.3). Notice for all the substations that are not directly connected by transmission lines, the injected current is simply $I_n = 0, \forall n \in \mathcal{N}^S$. Concatenating (3.4) across all $N$ nodes gives rise to

$$\mathbf{I}^{NO} := [I_1, \ldots, I_N]^T = \mathbf{CE} \tag{3.5}$$

where the $n$-th row of matrix $\mathbf{C}$ is given by $[\sum_{(n,m)\in\mathcal{L}} L^N_{nm} g_{nm}, \sum_{(n,m)\in\mathcal{L}} L^E_{nm} g_{nm}]$.

### 3.2.2 DC Network Analysis

To obtain the GIC flows, stack the dc voltage $V_n$ at any bus or substation neutral in $\mathbf{V} := [V_1, \ldots, V_N]^T$, which follows the dc power flow model as

$$\mathbf{V} = \mathbf{G}^{-1}\mathbf{I}^{NO} = \mathbf{G}^{-1}\mathbf{CE} \tag{3.6}$$

Note that $V_n$ is the dc node voltage, different from the induced line voltage $U_{nm}$. The GIC flow between any two nodes is given by

$$I^T_{nm} = g_{nm}(V_n - V_m),\ \forall n \in \mathcal{N}^B,\ m \in \mathcal{N}^S \tag{3.7}$$

By Ohm's law, the GICs at the transformer neutrals are related to the bus voltages:

$$\mathbf{I} = \mathbf{G}^S\mathbf{V} = (\mathbf{G}^S\mathbf{G}^{-1})\mathbf{I}^{No} = (\mathbf{G}^S\mathbf{G}^{-1}\mathbf{C})\mathbf{E} = \mathbf{HE} \tag{3.8}$$

where $\mathbf{G}^S$ is a diagonal matrix with the grounding resistances on its diagonal, $\mathbf{I}$ is the vector of currents passing through transformer neutrals and $\mathbf{H}$ is the coefficient matrix defined as $\mathbf{H} := \mathbf{G}^S\mathbf{G}^{-1}\mathbf{C}$ . This model indicates that the GICs are linearly dependent on the E-field through the coefficient matrix $\mathbf{H}$. Matrix $\mathbf{H}$ only depends on the network topology and resistances.

The GIC model represents the whole electrical network and the GIC vector $\mathbf{I}$ includes the neutral currents of all the transformers. For a large system, the whole network is not of interest, and it

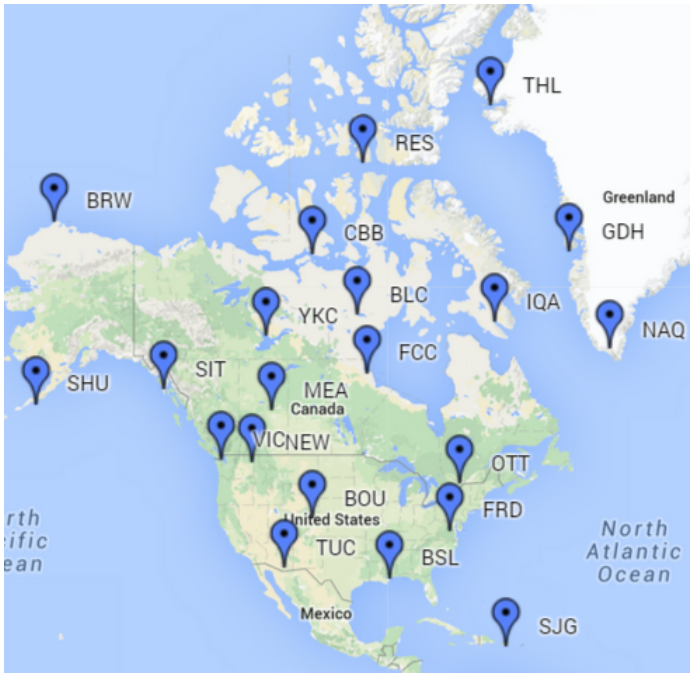


Figure 3.2: Geographic location of the investigated magnetic observatories.

is desired to reduce the model to cover only specific transformers. This can be done by selecting only the corresponding entries in the $\mathbf{I}$ matrix and truncating the coefficient matrix accordingly.

## 3.3 Electric Field Estimation Based on the Magnetic Data

The magnetic observatories operated by USGS and CSWFC provide magnetic measurements at multiple locations in North America [81]. The locations of these observatories are shown in Fig. 3.2. The electric field induced on the power lines is related to the magnetic flux density through the Earth's surface impedance as given by

$$E(\omega) = \frac{1}{\mu_0} \mathcal{Z}(\omega) B(\omega) \tag{3.9}$$

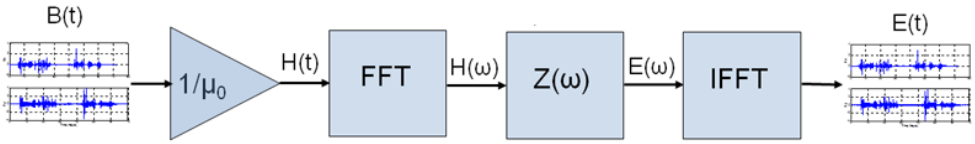


Figure 3.3: Estimation of E-field from magnetic field in frequency domain.

where $\mathcal{Z}$ is the earth surface impedance and $B$ is magnetic field intensity. Assuming uniform conductivity for Earth, the Earth surface impedance is obtained by

$$\mathcal{Z}(\omega) = \sqrt{\frac{j\omega\mu_0}{\sigma}} \tag{3.10}$$

where $\sigma$ is the Earth conductivity, $\omega$ is the frequency and $\mu_0$ is the permeability of free space. The Earth impedance is a function of frequency; therefore, it is easier to conduct the electric field calculation in the frequency domain. Fourier transform (FT) is used to convert the magnetic field data from time domain to frequency domain. In frequency domain, magnetic field intensity is multiplied by the Earth surface impedance to obtain the electric field. The resulting electric field is in frequency domain and inverse FT may be used to recover the electric field in time domain. This process is illustrated in Fig. 3.3.

Studies show that the conductivity of the Earth is not uniform and (3.10) provides a naive approximation of the Earth surface impedance [44]. To have a better approximation, a layered model for Earth conductivity is considered as shown in Fig. 3.4. The depth and conductivity of each layer depends on the tectonic structures of the region. The last layer (the innermost layer) is extremely deep, and its impedance can be calculated through the uniform conductivity model in (3.10). Having the impedance of the last layer, the impedance of each layer is obtained recursively based on the impedance of the layer below it as given by

$$\mathcal{Z}_n = \mathcal{Z}_0 \frac{1 + \dfrac{\mathcal{Z}_{n+1} - \mathcal{Z}_0}{\mathcal{Z}_{n+1} - \mathcal{Z}_0} e^{-2k_n d_n}}{1 - \dfrac{\mathcal{Z}_{n+1} - \mathcal{Z}_0}{\mathcal{Z}_{n+1} - \mathcal{Z}_0} e^{-2k_n d_n}} \tag{3.11}$$

where $Z_0$ is the impedance of the innermost layer, $d_n$ is the depth on the $n^{th}$ layer and $k_n$ is defined

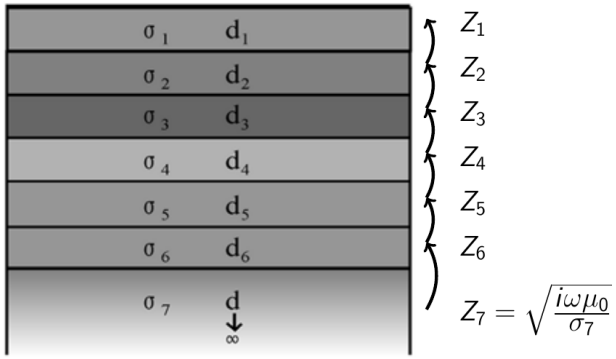


Figure 3.4: Earth layered resistivity model.

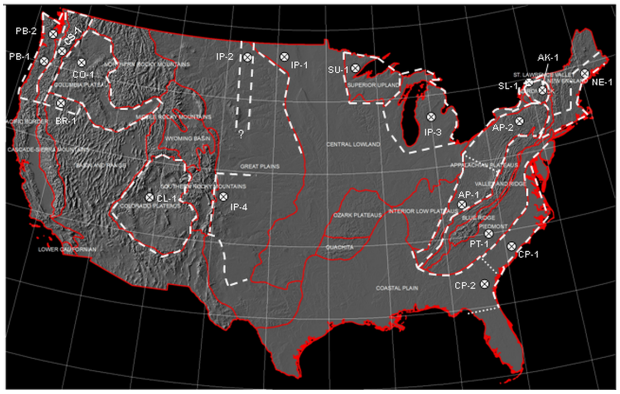


Figure 3.5: Earth resistivity models with respect to physiographic regions.

as $k_n := \sqrt{j\omega\mu_0\sigma_n}$. The Earth surface impedance is the impedance of the top layer and is obtained in the last recursion. This recursive process is demonstrated in Fig. 3.4

USGS provides the Earth resistivity models with respect to physiographic regions of the USA with the locations shown in Fig. 3.5. The model includes 12 to 14 layers for each region with the corresponding depths and conductivities. As an example, the resistivity model for the Lower Michigan Interior Plains (IP-3) is shown in Fig. 3.6. The dashed lines in the figure indicate the higher and lower resistivity range. Interestingly, the resistivity of each layer has a wide range of variation especially at the outer layers. This introduces uncertainty to the Earth surface impedance since it depends on the resistivity of the layers.

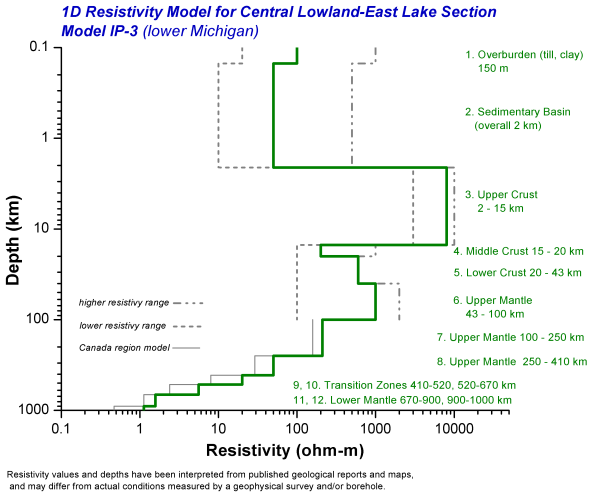


Figure 3.6: Resistivity model for Lower Michigan Interior Plains (IP-3).

## 3.4 Electric Field Estimation Based on the GIC Data

Assuming a uniform E-field model, at each instant in time, the E-field has two components: the eastward field $\mathbf{E}^E$ and the northward field $\mathbf{E}^N$. During the GMD, the E-field is dynamic over the discrete time horizon $\mathcal{T} := \{t^1, t^2, ..., t^T\}$, which can be concatenated into the $2 \times T$ matrix:

$$\mathbf{X} = \begin{bmatrix} e^{E,t^1} & e^{E,t^2} & \dots & e^{E,t^T} \\ e^{N,t^1} & e^{N,t^2} & \dots & e^{N,t^T} \end{bmatrix} \tag{3.12}$$

where $e^{E,t^n}$ and $e^{N,t^n}$ are the eastward and northward E-fields at the $n^{th}$ time instant, respectively. Similarly, for the dynamic GIC flow $\mathbf{I}$ to form the matrix:

$$\mathbf{Z} = \begin{bmatrix} z_1^{t^1} & z_1^{t^2} & \dots & z_1^{t^T} \\ z_2^{t^1} & z_2^{t^2} & \dots & z_2^{t^T} \\ \vdots & \vdots & \ddots & \vdots \\ z_K^{t^1} & z_K^{t^2} & \dots & z_K^{t^T} \end{bmatrix} \tag{3.13}$$

where $z_k^{t^n}$ is the GIC reading of the $k^{th}$ sensor at the $n^{th}$ time instant and $K$ is the total number of sensors. The GIC sensors are installed at the transformers neutral and measure the DC current

passing through its neutral. The matrix form of the linear GIC model is given by

$$\mathbf{Z} = \mathbf{H}\mathbf{X} + \mathbf{V} \tag{3.14}$$

where $\mathbf{V}$ is the measurement noise. As the GIC model is linear, the E-field may be obtained from GIC measurements using various linear estimators. Without prior information of $\mathbf{X}$, the most popular one is the ordinary LS estimator, as given by

$$\hat{\mathbf{X}}^{LS} := \arg\min_{\mathbf{X}} \|\mathbf{Z} - \mathbf{H}\mathbf{Z}\|_2 = (\mathbf{H}^T\mathbf{H})^{-1}\mathbf{H}^T\mathbf{Z} \tag{3.15}$$

where $\|\cdot\|_2$ is the vector Euclidean norm and $\hat{\mathbf{X}}$ is the estimated E-field. Assuming that the matrix $\mathbf{H}$ is full rank, the LS estimator has a simple closed-form solution and thus is efficiently computable. It is also statistically optimal assuming $\mathbf{V}$ is white Gaussian of uniform variance.

If some GIC readings are corrupted outliers, i.e., some entries of $\mathbf{V}$ fail to follow the normal distribution, robust estimation approaches are necessary. A simple one of that kind is the least absolute value (LAV) estimator, as given by

$$\hat{\mathbf{X}}^{LAV} := \arg\min_{\mathbf{X}} \|\mathbf{Z} - \mathbf{H}\mathbf{X}\|_1 \tag{3.16}$$

where $\|\cdot\|_1$ denotes the vector Manhattan norm which is equal to the sum of entry-wise absolute values. Although there is generally no closed-form solution for (10.3), it can be transformed to a convex linear program, for which efficient solvers are available. The LAV estimator is less accurate if there are actually no outliers; thus, different robust estimators have been proposed to tackle this, such as Huber's Estimator or a more recent one motivated by sparsity [82].

Additional information on $\mathbf{X}$ could greatly improve the performance of linear estimators. If the relative covariance of $\mathbf{X}$ with respect to noise standard deviation is known, this gives rise to the Ridge Regression (RR) by augmenting the LS error criterion as

$$\hat{\mathbf{X}}^{RR} := \arg\min_{\mathbf{X}} \|\mathbf{Z} - \mathbf{H}\mathbf{X}\|_2^2 + \mathbf{X}^T(\lambda\mathbf{I})^{-1}\mathbf{X}$$

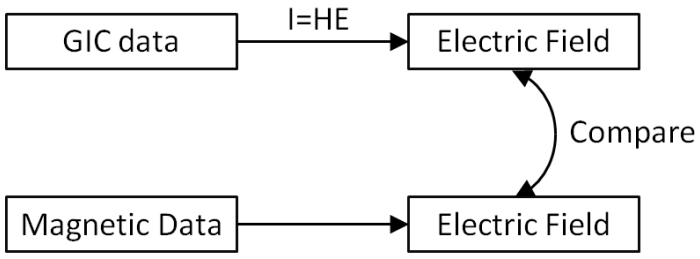


Figure 3.7: GIC model validation framework based on GICs and magnetic measurements.

$$= (\mathbf{H}^T\mathbf{H} + \lambda^{-1}\mathbf{I})^{-1}\mathbf{H}^T\mathbf{Z} \tag{3.17}$$

where $\lambda\mathbf{I}$ is the relative covariance of $\mathbf{X}$. By incorporating the prior information on $\mathbf{X}$, the RR is especially powerful in improving the numerical stability when $\mathbf{H}$ is ill-conditioned. However, this introduces some bias on the estimator, which may be difficult to account for in practice. Note that the three estimators (LS, RR and LAV) either have closed form expression or can be solved as a linear program. Hence, all the estimators enjoy low computational complexity.

The E-field estimated from GICs is eventually compared with the one obtained from the magnetic field data to validate the model as illustrated in Fig. 3.7.

# CHAPTER 4

# MITIGATION OF GMDS THROUGH LINE SWITCHING

## 4.1 Introduction

Hardening the network against GMDs through corrective control is an effective approach to improve resiliency. This chapter considers line switching as a remedial action for GMD mitigation in large-scale power systems. The algorithm uses linear sensitivity analysis to find the best switching strategy which minimizes the GIC-saturated reactive power loss. The coupling between the ac power flow solution and the GIC flows is modeled and proper heuristics are developed to maintain sufficient security measures in terms of both GIC flows and ac analysis. Finally, the computational complexity of the algorithm is analyzed and effective techniques are utilized to reduce its running time for large-system applications. The effectiveness of the algorithm is demonstrated through numerical results using a small 20-bus test case as well as large power systems. The algorithm provides an effective tool to minimize the transformer damage during GMDs and improve the resiliency.

The chapter is organized as follows: Section 4.2 presents the modeling of GIC-saturated reactive power loss. Solving power flow including GICs is described in Section 4.3. The proposed line selection algorithm is presented in Section 4.4. Section 4.5 demonstrates the proposed technique through numerical results. Section 4.6 presents a conclusion and direction for future work.

## 4.2 Modeling GIC-saturated Reactive Power Loss

The GIC passing through the transformer increases its reactive power loss. GIC-saturated reactive power loss can be linearly related to the effective GICs as expressed in:

$$Q^{GIC} = KV^{pu}I^{GIC} \tag{4.1}$$

where $Q^{GIC}$ is the GIC-saturated reactive power loss, and $K$ is the transformer loss coefficient which mostly depends on the core type [83]. $I^{GIC}$ is the effective GIC and is calculated based on the transformer type and winding configuration. For a grounded wye-delta transformer, $I^{GIC}$ is simply the current in the grounded coil. For transformers with multiple grounded windings (-autotransformers), the effective current is a function of the current in both coils as expressed in [84]:

$$I^{GIC} = \frac{aI_H + I_L}{\alpha} \tag{4.2}$$

where $I_H$ and $I_L$ are respectively the per phase dc current passing through the high side winding (-series winding) and low side winding (-common winding) and $\alpha$ is the transformer turn ratio. Calculating $I_H$ and $I_L$ from (3.7), the effective current at transformer $t$ is given by:

$$I_t^{GIC} = g_{sh}(V_h - V_s) + \frac{1}{\alpha}g_{sl}(V_l - V_s) \tag{4.3}$$

where $h$ and $l$ are the high and low side bus nodes for transformer $t$, and $s$ is its substation node. Concatenating (4.3) across all transformers gives rise to:

$$\mathbf{I}^{GIC} = \mathbf{\Phi V} = \mathbf{\Phi G}^{-1}\mathbf{CE} \tag{4.4}$$

where $\mathbf{\Phi}$ is a $T \times (N + N_S)$ matrix with the $(t, m)$-th entry given by

$$\Phi_{tm} := \begin{cases} g_{sm}, & \text{if } m = h \\ \alpha g_{sm}, & \text{if } m = l \\ -g_{sh} - \alpha g_{sl}, & \text{if } m = s \\ 0, & \text{otherwise.} \end{cases} \tag{4.5}$$

### 4.2.1 Effect of Line Switching on GIC Flows

Next, the effect of opening a line on the GIC flows is studied. Opening line $(n, m)$ modifies the $\mathbf{G}$ matrix by deducting the terms related to the disconnected pairs:

$$\mathbf{G} \leftarrow \mathbf{G} - g_{nm} e_{nm} e_{nm}^T \tag{4.6}$$

where vector $e_{nm}$ of length $N$ has all zero entries except for the $n$-th and $m$-th being +1 and -1, respectively. Similarly, the $\mathbf{H}$ matrix is modified by

$$\mathbf{H} \leftarrow \mathbf{H} - e_{nm}[L_{nm}^N, L_{nm}^E] \tag{4.7}$$

Opening a line does not affect the $\mathbf{\Phi}$ matrix. Opening multiple lines requires updating $\mathbf{G}$ and $\mathbf{H}$ successively for each opened line.

## 4.3 Power Flow Solution Including GICs

To solve power flow including the GICs, the GIC-saturated reactive power loss of each transformer is modeled as a constant current source. Adding these current sources changes the reactive power injections at the high voltage side of the transformers by:

$$Q_i \leftarrow Q_i - K V_i^{pu} I_i^{GIC} \tag{4.8}$$

where $Q_i$ is the reactive power injection at bus $i$. The power balance equations are nonlinear and the most common technique for solving them is Newton-Raphson solution. This technique uses the first order Taylor series to linearize the power balance equations as expressed in:

$$\begin{bmatrix} \Delta\theta \\ \Delta|\mathbf{V}| \end{bmatrix} = -\mathbf{J}^{-1} \begin{bmatrix} \Delta\mathbf{P} \\ \Delta\mathbf{Q} \end{bmatrix} \tag{4.9}$$

where $\Delta\mathbf{P}$ (-$\Delta\mathbf{Q}$) is the vector containing all the real (-reactive) power imbalances and $\mathbf{J}$ is Jacobian matrix defined as:

$$\mathbf{J} = \begin{bmatrix} \frac{\partial\Delta\mathbf{P}}{\partial\Delta\theta} & \frac{\partial\Delta\mathbf{P}}{\partial\Delta|\mathbf{V}|} \\ \frac{\partial\Delta\mathbf{Q}}{\partial\Delta\theta} & \frac{\partial\Delta\mathbf{Q}}{\partial\Delta|\mathbf{V}|} \end{bmatrix} \tag{4.10}$$

The algorithm starts with an initial guess, uses (4.9) to update the states in each iteration and continues the process until the power mismatches are smaller than a threshold. Adding the GIC-related constant current sources modifies the entries of the Jacobian that correspond to the partial derivative of the reactive power to voltage magnitudes of the same bus:

$$\frac{\partial\Delta Q_i}{\partial\Delta|V_i|} \leftarrow \frac{\partial\Delta Q_i}{\partial\Delta|V_i|} - KI_i^{GIC} \tag{4.11}$$

The other entries of the Jacobian matrix stay unchanged.

## 4.4 Iterative Line Switching Algorithm

The transformer LODF (TLODF) can be expressed as:

$$TLODF = [s_{ij}] = [Q_i^{GIC,(j)} - Q_i^{GIC,(0)}], \quad i \in T,\ j \in L \tag{4.12}$$

where $s_{ij}$ is the variation of GIC-saturated loss at transformer $i$ caused by opening line $j$, $Q_i^{GIC,(j)}$ is the GIC-saturated loss at transformer $i$ when line $j$ is opened and $Q_i^{GIC,(0)}$ is the initial loss. An analytical technique may be developed to derive TLODFs as a function of the network parameters.

Alternatively, one can follow the sensitivity definition to calculate the TLODFs as described in Algorithm 2. $L$ in the algorithm is the number of lines.

**Algorithm 2** Determining the TLODF

**procedure** DETERMINING THE TLODF
    Calculate the initial GIC-saturated loss at each transformer, $\mathbf{Q}^{GIC,(0)}$
    **for** $1 \leq n \leq L$ **do**
        Open line $n$
        Calculate the GIC-saturated loss at each transformer, $\mathbf{Q}^{GIC,(n)}$
        Calculate the $n^{th}$ column of the TLODF matrix by $\mathbf{Q}^{GIC,(n)} - \mathbf{Q}^{GIC,(0)}$
        Close line $n$
    **end for**
**end procedure**

TLODFs are used to identify the best line switching strategy that minimizes the GIC-saturated loss. The total loss reduced from opening a line is obtained by taking the sum of TLODF matrix along the corresponding column. Let $Q^T = Sum(TLODF, 2)$ be the sum of the TLODF matrix along the columns. The best lines are obtained by sorting $\mathbf{Q}^T$ in descending order and selecting the lines with the lowest $\mathbf{Q}^T$ values.

Similar to LODFs, TLODFs consider single line outages. The TLODF for multiple-line outages is not equal to the sum of the single-line TLODFs of the corresponding lines. The notion of generalized LODF was introduced in [85] which considers multiple-line LODFs. A similar concept may be considered for TLODF and analytical techniques can be developed to calculate multiple-line TLODFs. A rather simple approach for calculating TLODFs under multiple-line outages is to consecutively open one line and calculate the single-line TLODFs for the new system until all the desired lines are opened. The line switching algorithm can thus be improved using a similar approach. First, the TLODF is calculated and the best line to be opened is selected accordingly. Next, the TLODF matrix is calculated for the new system and the second line to be opened is selected. This process is repeated until the number of opened lines reaches a user-defined threshold, $M$. This technique is presented in Algorithm 3.

**Algorithm 3** Iterative Line Selection

```
procedure SELECTING BEST LINES TO OPEN
    for 1 ≤ m ≤ M do
        Calculate TLODFs
        Calculate Q^T from TLODF
        Find the line with lowest Q^T and open that line.
    end for
end procedure
```

### 4.4.1 Improving the Computational Complexity

The computational complexity of the proposed algorithm is $\mathcal{O}(LMT)$ where $L$ is the number of lines, $M$ is the maximum number of lines that can be opened and $T$ is the computation time for solving for the GIC flows. The number of lines for a power grid is typically slightly larger than the number of buses. Solving GIC flows requires calculating the inverse of $\mathbf{G}$ and then multiplying it by $\mathbf{\Phi}$. $\mathbf{G}$ is a sparse matrix roughly in the order of $O(N^2)$ and the computation time of taking its inverse is $\mathcal{O}(N^{2.2})$ [86]. $\mathbf{\Phi}$ is a sparse matrix of roughly the same order and multiplying it by $\mathbf{G}^{-1}$ requires $\mathcal{O}(N^{2+\mathcal{O}(1)})$ [87].

To reduce the running time, first, the TLODF matrix is calculated and $\mathbf{Q}^T$ is calculated for each line by taking the sum of the TLODF matrix over its columns. The first $C$ lines in the sorted list are selected as critical lines and are investigated for further analysis. $C$ is a user-defined parameter which controls the complexity. After selecting the critical lines, the iterative line selection algorithm is applied to only these lines; i.e., the TLODFs are calculated for only the critical lines and the optimal lines are obtained based on the $\mathbf{Q}^T$ values. The critical lines may be updated after each $U$ iterations by recalculating the full TLODF matrix. $U$ is again a user-defined parameter which controls the computation time. Some insights on how to select suitable $C$ and $U$ values are presented later through simulation. Details of the fast line selection algorithm are presented in Algorithm 4.

Parallel computing may be used to further reduce the running time. The columns of the TLODF matrix can be calculated in parallel. Another approach to improve the computational complexity is to take advantage of the small network modification in computing the inverse of G. Instead of computing the full $\mathbf{G}^{-1}$ each time a line is opened, it could be calculated just once for the base case and then be derived from the base case through rank-1 update in $\mathcal{O}(N)$ or $\mathcal{O}(N^2)$ compu-

**Algorithm 4** Fast Iterative Line Selection

```
1: procedure SELECTING BEST LINES TO OPEN
2:     Initialize the number of opened lines, m to zero.
3:     while m ≤ M do
4:         Calculate full TLODFs.
5:         Calculate Q^T from TLODF.
6:         Find the critical lines from Q^T.
7:         for 1 ≤ c < U do
8:             Update TLODFs for critical lines.
9:             Update Q^T of critical lines.
10:            Find the line with lowest Q^T and open it.
11:            m = m + 1.
12:            if m ≤ M then
13:                Break
14:            end if
15:        end for
16:    end while
17: end procedure
```

tations. The switching design procedure would probably be performed off-line, and therefore the computational complexity is not very critical. However, it may be desired to perform the analysis in real-time as the switching strategy depends on the state of the system, e.g. induced E-field and ac line flows (dependency on the ac flows will be explained in the next subsection).

### 4.4.2 Incorporating ac Analysis into the Algorithm

Opening a line changes the structure of the Jacobian matrix and the new system may not have a power flow solution. The line selection algorithm should guarantee that the switching strategy provides a power flow solution. One possible procedure to ensure this is as follows: The algorithm starts with the fist line in the sorted list. The candidate line is opened and the Y-bus of the new system is calculated. If the new Y-bus is full rank, the candidate line is selected. If not, it is discarded and the second line in the sorted list is considered as the new candidate. The process is continued until a line that provides a full-rank Y-bus is found as detailed in Algorithm 5. This process is performed instead of step five in Algorithm 3 or step 10 in Algorithm 4. Note that calculating the new Y-bus after opening a line is not computationally expensive as it can be derived from the initial Y-bus in negligible computational time.

**Algorithm 5** Power Flow Solution Check

```
procedure FIND THE LINE WITH POWER FLOW SOLUTION
    for 1 ≤ c < C do
        Open Line c in the sorted list.
        Calculate the Y-bus for the new System.
        if new Y-bus is full rank then
            Return line c.
        end if
        Close line c.
    end for
end procedure
```

Factors other than TLODFs may be used as a criterion for selecting the best lines. The power system experiences reactive power shortage during GMDs and reducing the GIC reactive loss is desired. However, opening a line changes the AC flows in the system and may compromise the system security. Hence, a meaningful line selection algorithm should consider some aspects of the ac analysis along with the already existing GIC related criterion (GIC-saturated loss). Motivated by this, the AC line flow may be considered as an additional criterion for selecting the best lines:

$$F_i = \frac{\mathbf{Q}_i^T}{\bar{P}_i} \tag{4.13}$$

where $\bar{P}_i$ is the flow on line $i$. $F$ is calculated for all the lines and the line with the lowest $F$ value is selected in each iteration. This criterion selects the line that reduces the GIC-saturated loss more and also has lower AC flow on it.

### 4.4.3 Line Switching Strategy through Exhaustive Search

The iterative line switching algorithm is computationally efficient and scalable to larger systems; however, its solution is not optimal. The problem of finding multiple best lines is simplified to finding the single best line in each iteration. This provides the local optimum and not necessarily the global one. Moreover, the procedure to guarantee the power flow solution is naive and the algorithm may fail to find the existing feasible actions that can provide power flow solutions. Examples of such corner cases will be shown later. For smaller systems, alternative approaches may be used which are more computationally expensive, yet provide a better solution. A greedy

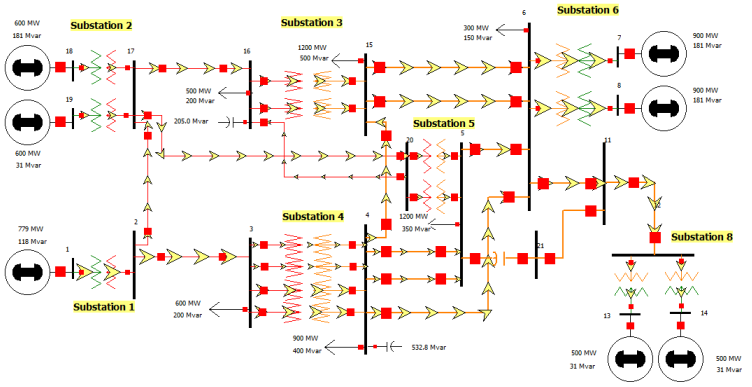


Figure 4.1: One-line diagram of the 20-bus system in [38].

algorithm applicable to small systems is described below:

Let $M$ be the maximum number of lines that can be opened and $L$ be the number of lines. All distinct ways of selecting $M$ lines from $L$ lines are considered, i.e. $\binom{L}{M}$ combinations. For each candidate action, the selected lines are opened, the GICs for the new system are calculated and the resulting loss is obtained. The combinations are sorted based on their associated losses, and the action which provides the lowest loss is chosen as the best action. For a large system, the number of possible combinations is huge and performing exhaustive search is not practical. To address this, the search can be narrowed down by finding the critical lines and performing the exhaustive search on only those lines. The critical lines are identified based on the TLODFs and the $\mathbf{Q}^T$ values. This reduces the running time from $\binom{L}{M}$ to $\binom{L}{C}$ where $C$ is the number of critical lines.

## 4.5 Numerical Results

In this section, the algorithm is applied to systems of varying sizes and its performance is evaluated through numerical results.

Table 4.1: Line Switching Solutions Obtained from the Iterative Algorithm for the 20-bus System

| Order | Opened Line | Total Loss |
|---|---|---|
| 0 | - | 19.68 |
| 1 | 5 | 18.16 |
| 2 | 6 | 15.24 |
| 3 | 14 | 12.34 |
| Running Time: 0.35 s | | |

Table 4.2: Line Switching Solutions Obtained from the Exhaustive Search for the 20-bus System

| Number of Opened Lines | Action Number | Opened Lines | Total Loss (pu) | Running Time (s) |
|---|---|---|---|---|
| 2 | 1<br>2* | 7, 8<br>5, 6 | 13.39<br>15.24 | 4.42 |
| 3 | 1<br>2* | 6, 7, 8<br>5, 6, 14 | 12.10<br>12.34 | 21.20 |
| 4 | 1 | 5, 8, 14, 16 | 11.56 | 73.81 |
| 5 | 1 | 5, 8, 13, 14, 16 | 10.66 | 186.64 |

### 4.5.1 20-bus System

First, the 20-bus system in [38] is investigated with the one-line diagram shown in Fig. 4.1. An electric field with the magnitude of 8 V/km and the orientation of 124°N is enforced to the system. This orientation results in the largest GICs for the system and hence is considered for the analysis. The GIC model in (4.4) is used to calculate the GIC-saturated loss and the line selection algorithm is utilized to minimize the loss. The selected lines in each iteration and the resulting total loss are presented in Table 4.1. The algorithm is terminated after the third step since opening any of the remaining lines results in an ill-conditioned Jacobian and no power flow solution. The running time of the algorithm is 0.35 seconds.

Next, the iterative algorithm is compared with the exhaustive search. Table 4.2 presents the best actions obtained from the exhaustive search when the number of opened lines, $M$ changes from two to five. For $M = 2$ and $M = 3$, the second best action found by the exhaustive search is the same as the one obtained from the iterative algorithm (shown by $^*$ in the table). This indicates

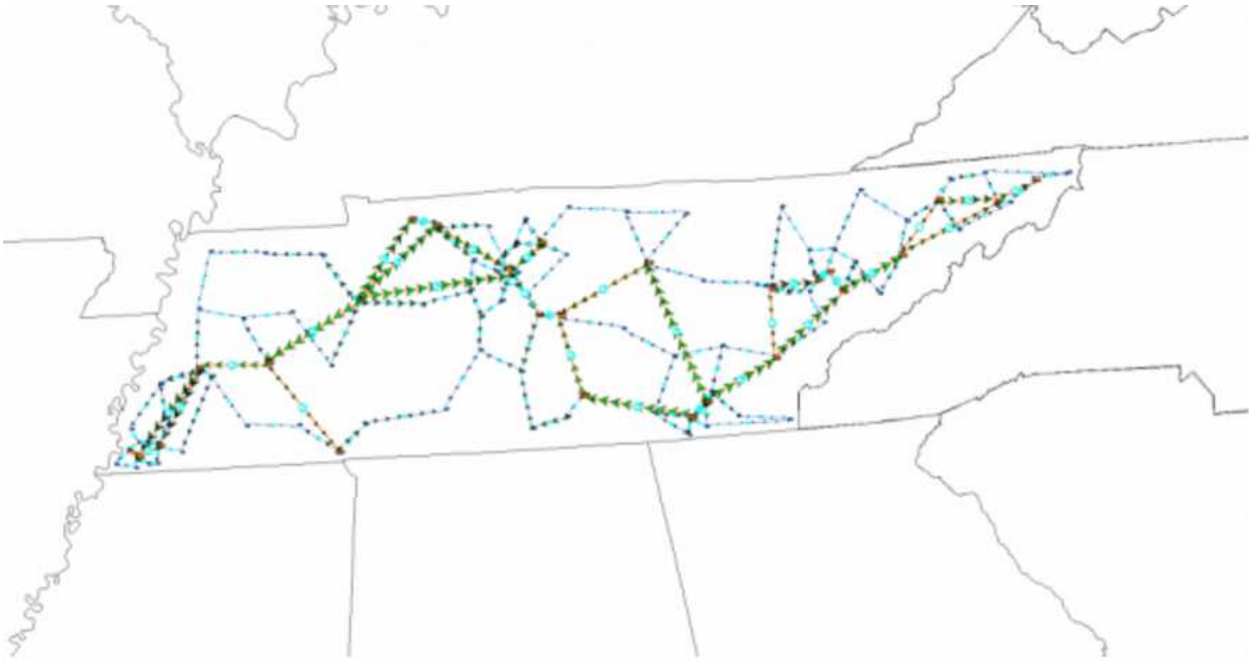

Figure 4.2: One-line diagram of the150-bus synthetic system; the green lines are 500 kV and the blue lines are 230 kV.

that the solution from the iterative algorithm is very close to the optimal solution. For $M = 4$ and $M = 5$, the exhaustive search still manages to find feasible solutions, unlike the iterative algorithm that terminates at the third iteration. This shows that the procedure to find feasible actions with power flow solutions is naive and there might be corner cases that the iterative algorithm fails to find.

### 4.5.2 A 150-bus Synthetic System

The next system to study is the medium-size UIUC 150-bus synthetic test case in [39, 55] with the one-line diagram illustrated in Fig. 4.2. The green lines in the one-line diagram are 500 kV and the blue lines are 230 kV. This case is entirely synthetic, built from the public load/generation data of the Tennessee region and a statistical analysis of real power systems.

An electric field with 8v/km magnitude and 26°N orientation is enforced to the system. Again, the motivation for choosing this orientation is that it provides the highest GICs. The GIC flow is solved and the resulting GIC-saturated loss is calculated. Figure 4.3 shows the effect of GICs on

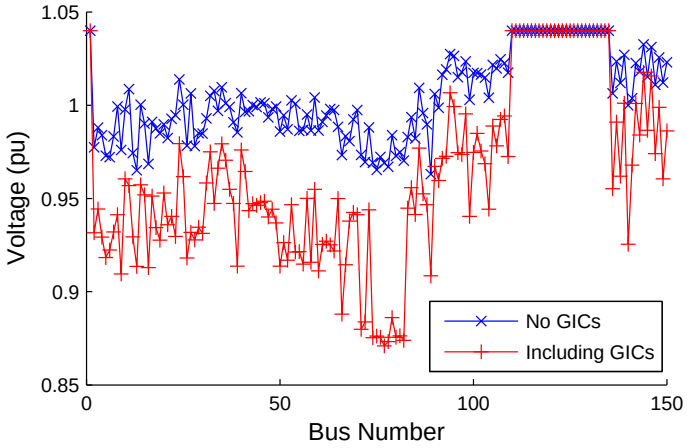


Figure 4.3: Effect of GICs on the voltage profile of the 150-bus synthetic system.

the voltage profile. The system experiences reactive power shortage due to the GIC-saturated loss and the voltage at most of the PQ buses falls below the permissible value, i.e. 0.95 pu.

The line selection algorithm is utilized to minimize the loss. Figure 4.4 illustrates the performance of the algorithm using two approaches: 1) using TLODFs as the criterion to select the best line, 2) using a combination of TLODFs and AC line flows as proposed in (4.13). Both approaches reduce the total loss as more lines are opened. The total loss is lower when only TLODFs are considered. However, the algorithm terminates at the seventh iteration since no other action with power flow solution can be found beyond that point. Including the AC line flows in the algorithm results in larger loss in each iteration, yet the algorithm can proceed up to the $21^{th}$ iteration while still providing a feasible solution. The final solution obtained at the last iteration of this approach has a lower loss than the one obtained from the last step of the first approach which includes only TLODFs.

Figure 4.5 shows the average of the bus voltages at different steps of the algorithm using the two approaches. The average voltage is higher when AC line flows are integrated in the selection process. This suggest incorporating the ac analysis in GMD mitigation for improved performance.

The GIC-saturated loss in the individual transformers before and after utilizing the line switching algorithm is illustrated in Fig. 4.6. The algorithm reduces the losses significantly in most of the transformers. The losses remain unchanged or even slightly increased for few of the transformers.

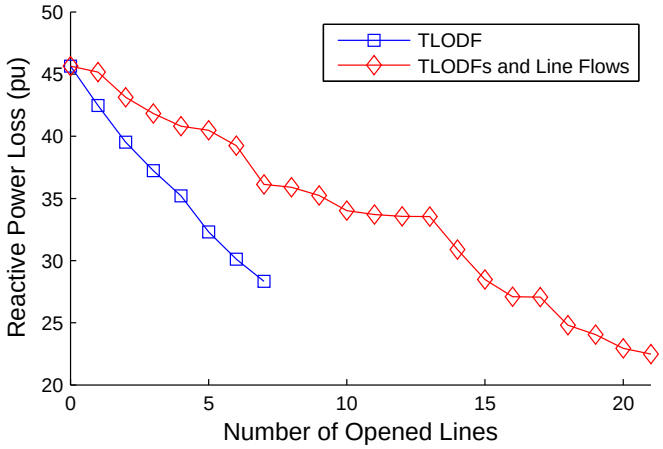


Figure 4.4: Total GIC-saturated reactive power loss in terms of the number of opened lines using the proposed line switching algorithm.

Developing techniques to restrict the losses in each transformer as opposed to the minimizing the overall loss will be an interesting future study.

### 4.5.3 2000-bus Synthetic System

The last system to study is the 2000-bus synthetic system [55, 79]. Similar to the 150-bus synthetic system, this case is entirely synthetic and built from the public load/generation data of the region using real power systems statistical analysis.

An electric field with 8v/km magnitude and 91°N orientation (the direction with highest GICs) is enforced to the system. The GIC-saturated loss is calculated and the line selection algorithm is applied to find the best switching strategy. The system is large and the running time is significant, i.e. 3047.7 seconds when the number of opened lines is 120. The computations are performed on a Dell XPS 700 system with Intel core i7. The running time may be reduced through the fast line selection algorithm. Figure 4.7 illustrates the total loss in terms of the number of opened lines for two scenarios:

(A) All the lines are considered and the full TLODF matrix is updated in each iteration.

(B) 200 critical lines are selected and the full TLODF matrix is not updated ($C = 200$, $U$ is not

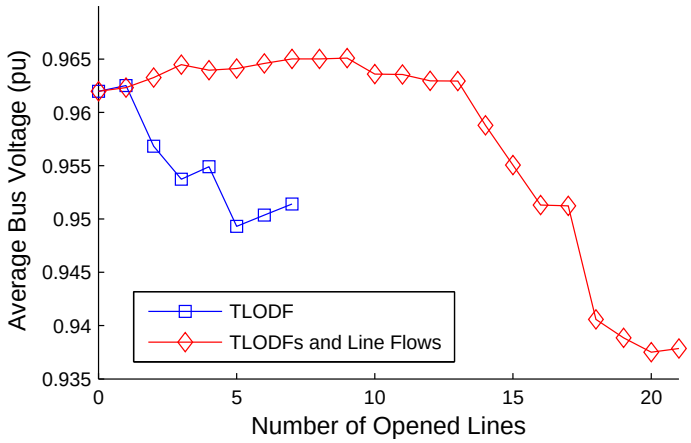


Figure 4.5: Average bus voltage in terms of the number of opened lines using the proposed line switching algorithm.

Table 4.3: Analyzing the Computational Complexity of the Iterative Line Switching Algorithm under Different Scenarios

| | TLODF Update Frequency | Number of Critical Lines | Running Time (s) | Total Loss (pu) | Error (%) | Time Ratio (%) |
|---|---|---|---|---|---|---|
| A | 1 | 3024 | 3047.7 | 3.62 | 0 | 100 |
| B | - | 200 | 124.4 | 4.18 | 15.61 | 4.08 |
| C | 10 | 200 | 320 | 3.72 | 2.47 | 10.49 |
| D | 40 | 200 | 181 | 3.71 | 2.72 | 5.93 |
| E | 40 | 100 | 105.2 | 3.72 | 2.72 | 3.45 |

defined).

It is observed that the fast scenario (Scenario B) provides the same loss as the full calculation (Scenario A) when the number of opened lines is smaller than 40 and start to diverge afterwards. Hence, it is reasonable to recalculate the TLODFs and update the list of critical lines after each 40 iterations, i.e. $U = 40$.

Table 4.3 presents the running time and accuracy of the algorithm for different values of U (the TLODF update frequency) and C (and the number of critical lines). The first two scenarios in the table are the same scenarios presented earlier. The accuracy of each scenario is presented in terms of the percentage error between its resulting loss and the one from the full search (Scenario A).

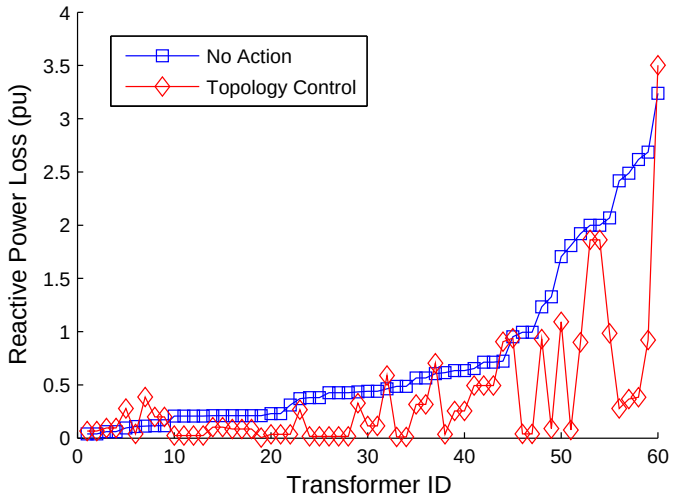


Figure 4.6: GIC-saturated loss in the individual transformers before and after utilizing the topology control.

The presented time ratio denotes the ratio of the running time of each scenario to the full search. Using the fast search with 100 critical lines and the TLODF update frequency of 40 (Scenario E) can provide the same performance as the full search with 2.72% error at only 3.45% of its running time.

## 4.6 Conclusions

In this chapter, a line switching algorithm is developed to mitigate the negative impacts of GMDs. The algorithm minimizes the GIC-saturated reactive power loss based on TLODFs (counterparts of LODFs in GIC analysis). Some aspects of the ac analysis are considered to provide sufficient ac-related security measures. The computational complexity of the algorithm is analyzed and heuristics are utilized to reduce its running time for large-system applications. The algorithm performance is evaluated through numerical results using the small 20-bus system, the medium-size 150-bus synthetic system and the large 2000-bus synthetic case. The main observations are as follows:

- Considering the AC line flows as an additional criterion for selecting the best lines improves

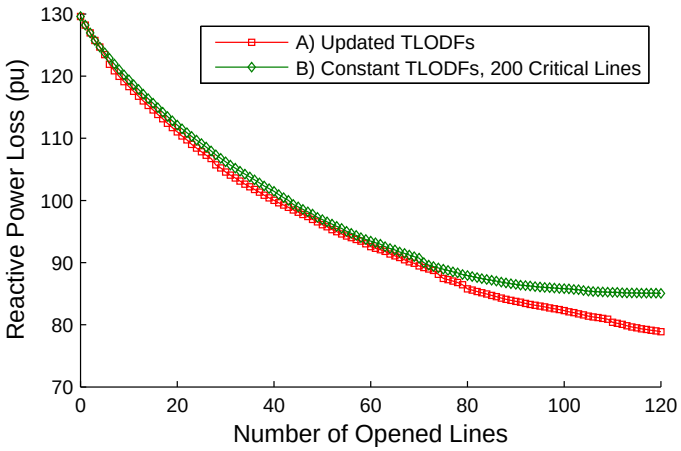


Figure 4.7: Effect of the TLODF update frequency on the performance of the algorithm for the 2000-bus synthetic system.

the overall performance in terms of AC and DC power flow solutions.

- The optimality of the proposed strategy was evaluated by comparing it with the exhaustive search. The numerical results indicate that while the algorithm does not find the optimal solution, it gets very close to it (finds the second best solution).

- The heuristics used for fast computation are evaluated through case studies on the 2000-bus synthetic system. It was observed that that the running time can be reduced by up to 97% while the loss reduction is compromised by only 2%.

The chapter suggests several directions for future research. First, the proposed algorithm minimizes the total loss in the system, but does not impose any limit on the loss of individual transformers. The algorithm can be further refined to restrict the losses in each transformer while minimizing the total loss. Second, this chapter focuses on line switching as the remedial action. Future research can extend this framework to other types of actions such as shunt capacitor switching and neutral blocking devices.

# CHAPTER 5

# GMD MODEL VALIDATION BASED ON SINGULAR VALUE DECOMPOSITION

## 5.1 Introduction

This chapter proposes singular value decomposition (SVD) to validate the GIC model solely through the measurements and independent of the network information. Under the uniform E-field, there exists a linear relation between the GICs and the E-field. This enables development of an SVD-based technique to estimate the E-field and eventually validate the model. This framework is later extended to include more realistic non-uniform E-fields and its effectiveness is verified using a practical 20-bus test case. GMD modeling is a fundamental part of the GMD mitigation and the model validation tool presented in this chapter can contribute to the resiliency against GMDs by improving the associated models.

The chapter is organized as follows: SVD-based analysis is presented in Section 5.2, which introduces the singular vectors for estimating the E-field. Section 5.3 presents the proposed validation framework using a 20-bus test case. In Section 5.4, the GIC model is modified to account for non-uniform E-field and its validity is examined using SVD and through simulation. Section 5.5 presents a conclusion and directions for future work.

## 5.2 Singular Value Decomposition

The GIC model is defined in (3.14) and reproduced below:

$$\mathbf{Z} = \mathbf{H}\mathbf{X} + \mathbf{V}$$

where $\mathbf{X}$ and $\mathbf{Z}$ are the matrices containing electric field and GICs data respectively, as expressed in:

$$\mathbf{X} = \begin{bmatrix} e^{E,t^1} & e^{E,t^2} & \dots & e^{E,t^T} \\ e^{N,t^1} & e^{N,t^2} & \dots & e^{N,t^T} \end{bmatrix} \qquad \mathbf{Z} = \begin{bmatrix} z_1^{t^1} & z_1^{t^2} & \dots & z_1^{t^T} \\ z_2^{t^1} & z_2^{t^2} & \dots & z_2^{t^T} \\ \vdots & \vdots & \ddots & \vdots \\ z_K^{t^1} & z_K^{t^2} & \dots & z_K^{t^T} \end{bmatrix}$$

An interesting observation follows as the rank $R := \text{rank}(\mathbf{Z}) \leq 2$ since $\text{rank}(\mathbf{X}) \leq 2$. However, the real data matrix might not exactly exhibit this low rank due to the measurement noise, system perturbations or non-uniform E-filed. To tackle this, we propose to use the singular value decomposition (SVD) for matrix $\mathbf{Z}$ to get the best rank-2 approximation [88]. To this end, the matrix SVD can be written as

$$\mathbf{Z} = \mathbf{U}\mathbf{S}\mathbf{V}^T = \sum_{r=1}^{R} s_r u_r v_r^T \tag{5.1}$$

where $\mathbf{U}(\mathbf{V})$ is the orthonormal matrix formed by left-(right-) singular vectors $\{u_r\}_{r=1}^R$ ($\{v_r\}_{r=1}^R$), and $S$ is a diagonal matrix formed by the singular values $\{s_r\}_{r=1}^R$. The SVD analysis is closely related to the matrix rank. The noise-free matrix $\mathbf{Z}$ has rank $R = 2$, and the two right singular vectors $v_1$ and $v_2$ will scale, respectively, with the eastward and northward E-fields. For higher-rank matrix, $s_1 u_1 v_1^T + s_2 u_2 v_2^T$ will be the best rank-2 approximation to $\mathbf{Z}$ in the sense of minimum Frobenius norm difference.

SVD analysis can validate the GIC model by two means. The first approach is to look at the singular values of the GIC matrix to evaluate its rank. The data would perfectly match the model when there are two larger singular values and the rest are remarkably small. In this case, the matrix rank would be close to two, indicating the data is well fitted to a rank-2 approximation similar to the model in (5.1). The second approach is to compare the E-field estimated through the two right singular vectors with the one obtained from the magnetic field data. Agreement between these two estimations validates the model.

The advantage of SVD analysis is that it does not require any prior information about the net-

work. This method estimates the E-field through the GIC measurements without using any additional network information. SVD analysis also benefits from robustness to different types of uncertainties in the system. The three common sources of error with significant impact on the GIC model are recognized as follows:

**1. White Gaussian noise:** The noise generated by many natural sources appears in the form of white Gaussian noise. GIC measurements are often perturbed by this type of noise.

**2. Incorrect meter scaling:** It is possible that the GICs obtained from measuring devices differ from the actual GICs by some constants. This type of error is caused by the incorrect meter scaling.

**3. Outliers:** The linear GIC model assumes uniform E-field over all measurements. Natural factors such as geographic distant, regional ground structure or neighboring water bodies could result in a different E-field for a transformer. The GIC measured at such a transformer does not agree with the model and is considered as outlier.

The robustness of the SVD-based method to these three types of uncertainties is evaluated later through simulation.

## 5.3 Numerical Results Using a Test Case

In this section, the effectiveness of the proposed model validation techniques is evaluated through simulation. For this study, the 20-bus system in [38] is investigated with the one-line diagram illustrated in Fig. 4.1. For this testing we will superimpose actual GMD data from March $9$, $2012$, on this fictitious test system. On March 9, the geomagnetic storm began at 2:00 UTC and reached a very high level in the following hours. The magnetic field data used here are from values measured at the Fredericksburg observatory, located in the US at a latitude/longitude of $38.205°N$, $77.373°W$. The E-field obtained from this magnetic field is enforced on the system and the induced GICs are determined by solving the GIC flows using PowerWorld Simulator with the GIC add-on. To simulate the system perturbations and measurement noise, white Gaussian random noise with

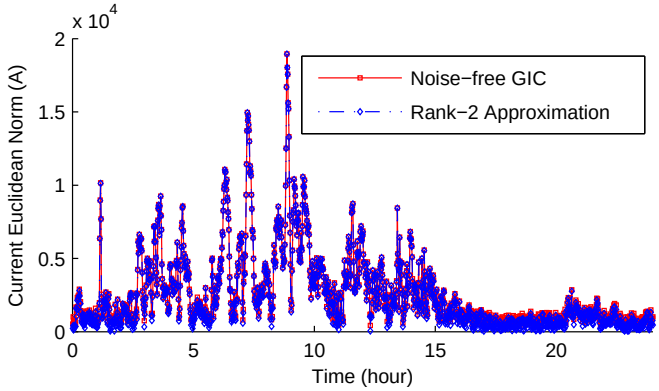


Figure 5.1: Comparison of the noise-free GIC and the rank-2 approximation.

signal-noise-ratio (SNR) equal to $20$dB is added to the ideal GICs and the synthetic measurements are obtained.

SVD analysis is used to obtain the rank-2 approximation of the GIC matrix as illustrated in Fig. 5.1. This approximation has extremely high agreement with the actual noise-free data. To validate the relation between the first right singular vector $v_1$ and the eastward E-field, both vectors are scaled to have a unit Euclidean norm and plotted in Fig. 5.2. Clearly, there is a strong correlation between the two plots, which validates the claim of Sec. 5.2 that the SVD analysis can indicate the actual E-field up to scaling. Last, the first left singular vector $u_1$ is also compared with the actual eastward coefficients. For comparison, both fields have also been scaled to have unit Euclidian norm, as shown in Fig. 5.3. It is observed that the left singular vectors agree well with the coefficients. However, this is not a general observation and the left singulars are not guaranteed to always correlate with the coefficients. Examples of such disagreement will be provided later in the chapter.

The robustness of the SVD-based E-field estimation to Gaussian noise, incorrect meter scaling and outliers is demonstrated in Fig. 5.4. For each of these noise scenarios, three severity levels are considered, termed as “Low”, ”Moderate”, and “High”. White Gaussian noise with SNR equal to $20$, $10$ and $5$ is added to the ideal measurements to simulate the Low, Moderate, and High scenarios, respectively. To model incorrect meter scaling, each reading is multiplied by a uniformly distributed random variable whose range relates to the noise severity. $(0.75, 1.5)$, $(0.5, 3)$ and

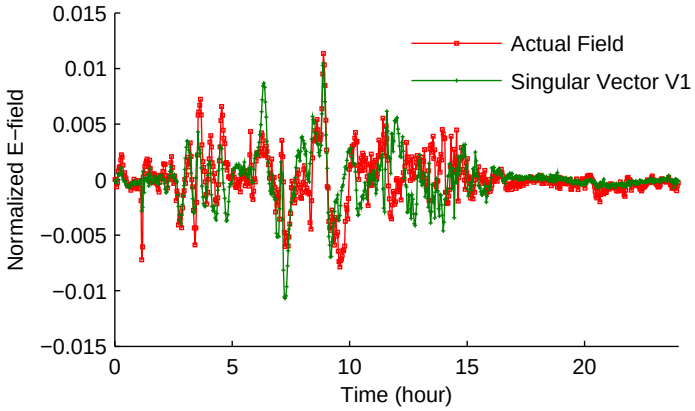


Figure 5.2: Comparison of the actual northward E-field and the estimate using $v_1$.

$(0.25, 6)$ are the three ranges used to model the severity levels with the wider range corresponding to more severe scenario. Finally, the outliers are modeled by using a different E-field to generate them. The E-field is based on actual data for the same time period from the Ottawa observatory, located in Canada at a latitude/longitude of $45.403°N$, $75.552°W$. The Ottawa data is used to simulate the outliers whereas the normal measurements are generated by the Fredericksburg data. The severity level is increased from Low to High by increasing the number of outliers from $1$ to $3$. Monte Carlo simulation with $100$ realizations is investigated to perfectly simulate all types of uncertainties. It is observed that the E-field estimation is very robust to Gaussian noise and incorrect scaling. Although the robustness of the estimator to outliers is relatively low, it still provides sufficient accuracy and the error stays below $3.5\%$.

The first left singular vector is compared with the eastward coefficients under different scenarios and its normalized error is plotted in Fig. 5.5. The interesting observation is that the coefficient estimation is very robust to Gaussian noise, yet is very sensitive to incorrect scaling and outliers. The sensitivity to outliers is especially very high and the error goes as high as $100\%$. This suggests that the SVD-based coefficient estimation is not valid in the presence of these types of noise.

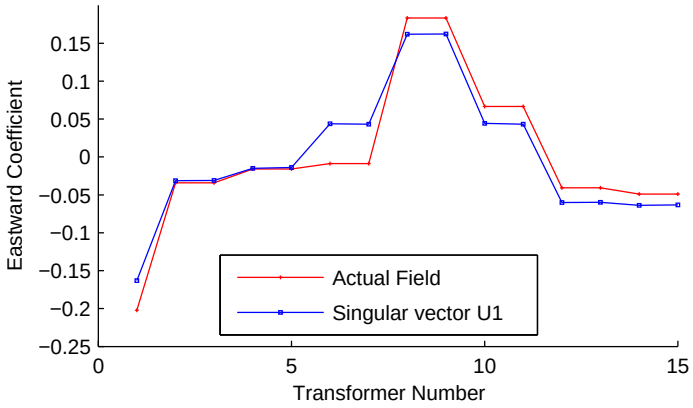


Figure 5.3: Comparison of the actual northward coefficients with the estimate using the right singular vector $u_1$.

## 5.4 Non-uniform Electric Field

The E-field varies with the magnetic field and the surface impedance as given in (3.9) and reproduced here:

$$E(\omega) = \frac{1}{\mu_0} \mathcal{Z}(\omega) B(\omega)$$

where $\mathcal{Z}$ is the Earth surface impedance, $B$ is the magnetic flux density, $\omega$ is the frequency and $\mu_0$ is the permeability of free space. The surface impedance depends on the regional tectonic structure and is calculated through the local conductivity model [89]. The magnetic field varies with the geomagnetic latitude. Preliminary studies consider the effect of both latitude and local conductivity on the E-field to be linear and model it through scaling factor as given by [90]:

$$\mathbf{E} = \alpha\beta \, \mathbf{E}_{ref} \tag{5.2}$$

where $\alpha$ and $\beta$ are the scaling factors to account for the local earth conductivity structure and the geomagnetic latitude respectively, and $E_{ref}$ is the reference E-field. The GIC of the $k^{th}$ transformer

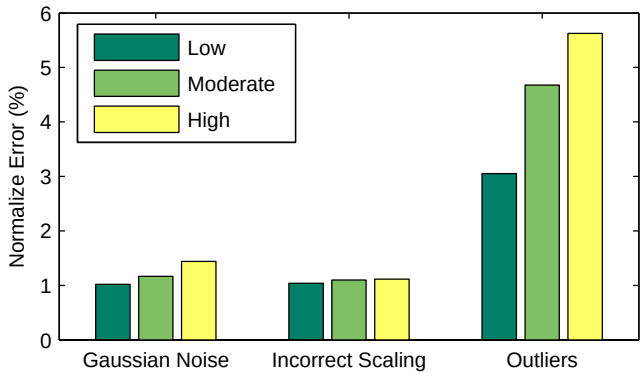


Figure 5.4: Robustness of the SVD-based E-field estimation to different system uncertainties.

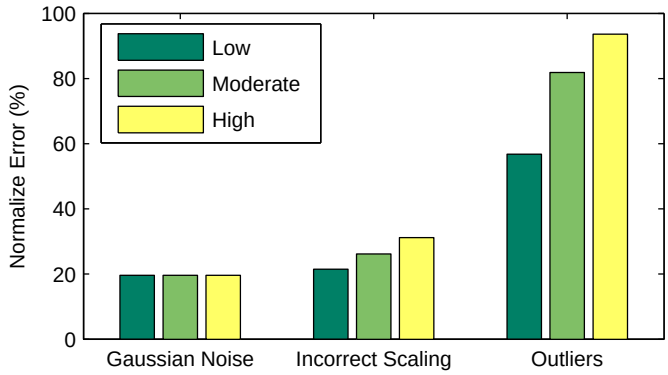


Figure 5.5: Accuracy of the SVD-based coefficient estimation under different system uncertainties.

at the $n^{th}$ time instant is given by:

$$z_k^{t^n} = H_k E_k^{t^n} = H_k \lambda_k E_{ref}^{t^n} \tag{5.3}$$

where $\lambda_k := \alpha_k \beta_k$ is the scaling factor for the $k^{th}$ transformer. Writing this for all the measurements at all the time instances gives rise to:

$$\mathbf{Y} = [\lambda_1 H_1 | \lambda_2 H_2 | \cdots | \lambda_K H_K]^T \mathbf{X} = \mathbf{H}_C \mathbf{X} \tag{5.4}$$

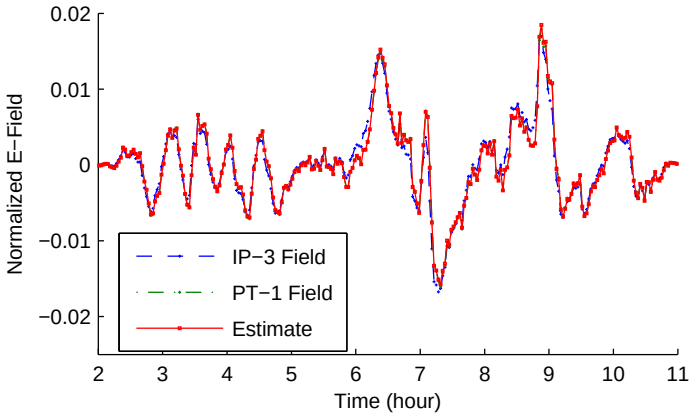


Figure 5.6: Non-uniform E-field scenario with different conductivity: estimated and actual E-fields in north direction.

where $\mathbf{H}_C$ is the modified coefficient matrix to account for the non-uniform E-field. Note that the rank of the GIC matrix is still two since rank$(\mathbf{X}) \leq 2$.

Next, the impacts of these scaling factors are considered through simulation using the 20-bus test case. Two non-uniform E-field scenarios are considered and SVD is used to validate the model under these scenarios. The first scenario considers two E-fields both generated by the same magnetic field (Fredericksburg), but two different conductivity models. These models relate to the Piedmont (PT-1) and the lower Michigan Interior Plains (IP-3). The E-field generated by the PT-1 model is enforced to the substations 1, 2 and 3 whereas the rest of the network is subject to the IP-3 E-field. The induced GICs are determined by solving the GIC flow program and SVD is used to estimate the electric field. The estimated E-field, the IP-3 E-field enforced to the first three substations and the PT-1 field enforced to the rest of the network are normalized and plotted in Fig. 5.6. It is observed that the IP-3 and PT-1 E-fields are highly correlated with $0.97$ correlation coefficient. This indicates that the effect of the local conductivity on the E-field is closely linear and modeling it through the scaling factor $\lambda$ is valid and accurate. This is further verified by observing the agreement between the estimated E-field with the two E-fields in the network.

The second scenario studies the effect of the geomagnetic latitude on the E-field. In this scenario, the two E-fields are generated by two different magnetic data (Fredericksburg and Ottawa), but the same conductivity model (IP-3). The Ottawa E-field is enforced to the first three substa-

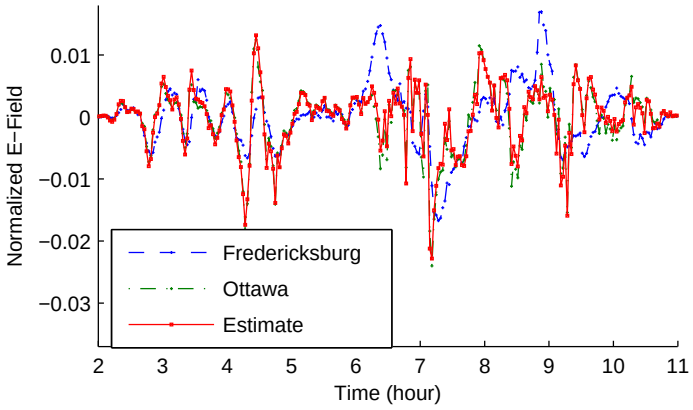


Figure 5.7: Non-uniform E-field scenario with different magnetic field data: estimated and actual E-fields in north direction.

tions and the rest of the network is covered by the Fredericksburg E-field. These two E-fields along with the estimated field obtained from GICs are normalized and plotted in Fig. 5.7. It is clear that the Ottawa and Fredericksburg E-fields are weakly correlated ($0.41$ correlation coefficient), which implies that the effect of the geomagnetic latitude on the E-field is not linear. The interesting observation is that the estimated E-field agrees with the Ottawa E-field and not Fredericksburg even though most of the substations are covered by the Fredericksburg field. A possible explanation is that the Ottawa E-field is, on average, $4.9$ times larger than Fredericksburg which makes it the dominating field. The fact that the estimated E-field does not agree with both of the enforced E-fields suggests that using the scaling factor for the geomagnetic latitude may not provide sufficient accuracy and a more detailed model is desired.

## 5.5 Conclusions

This chapter investigates how to validate the GIC model using a modeless, SVD-based approach. Under an ideal uniform electric field, there exists a linear relation between the transformer GIC values and the E-field. Nonetheless, without accurate information of the power network topology and dc conductances, it becomes extremely difficult to characterize such linear dependency and accordingly estimate the E-field for validation. To tackle this, further analysis of the geomagnetic data suggests that the GIC matrix formed by different transformers across time will have rank

2 and the right singular vectors can be used to infer the E-field. This SVD-based approach has validated the linear relation using a realistic test case. The validation framework is also extended to account for non-uniform E-field and is successfully demonstrated through simulation.

# CHAPTER 6

# PARAMETER-BASED GMD MODEL VALIDATION

## 6.1 Introduction

Providing resiliency to GMDs is very challenging and it is desired to utilize all the available information on the network to achieve this goal. This chapter proposes a validation technique which improves over the SVD-based one in Chapter 5 by utilizing the available parameters. In this technique, first, the conventional GIC model is modified to account for the system uncertainties. Then, a validation framework is built upon this modified model. This framework is successfully demonstrated using a PowerWorld case study and its performances is evaluated. The effectiveness of the proposed technique in handling real system uncertainties is validated through actual GIC data provided by the American Transmission Company (ATC).

The chapter is organized as follows: Model validation under system uncertainties is presented in Section 6.3. Section 6.4 demonstrates the proposed technique using the 20-bus PowerWorld test case, while the more interesting real data validation is given in Section 6.5 with transformer neutral current measurements from ATC. Section 6.6 presents a conclusion and directions for future work.

## 6.2 Determination of the Transformers Coefficients

There are two coefficients associated with each transformer and the GIC model in (3.8) can be rewritten as:

$$\mathbf{I} = [\mathbf{H}^E \mid \mathbf{H}^N] \times \begin{bmatrix} E^E \\ E^N \end{bmatrix} \tag{6.1}$$

where $H^E$ and $H^N$ are the eastward and northward coefficients. An interesting observation is that the GICs are equal to the eastward coefficients when $E^E$ is one and $E^N$ is zero. Similarly, the GICs are equal to the northward coefficients when $E^E$ is zero and $E^N$ is one. This will be a basis for finding the coefficients as described in the following algorithm.

**Step 1:** An eastward E-field with unity magnitude is enforced to the system and the resulting GICs are calculated. According to (6.1), the eastward coefficients are equal to the GICs under this condition.

**Step 2:** A northward E-field with unity magnitude is enforced to the system and the northward coefficients are calculated similar to Step 1.

This algorithm requires calculation of the GICs induced by an enforced E-field. This can be done through basic circuit laws e.g. KVL, KCL and Ohm's law. Alternatively, a commercial power system software like PowerWorld Simulator may be used to conduct such calculations.

## 6.3 Model Validation Under Actual Measurements

In practice, the GIC model in (3.14) fails to represent the actual measurements as they are subjected to different types of noise and system uncertainties. To account for such uncertainties, the GIC model is modified by introducing a scale for each measurement as given by:

$$\mathbf{Y} = \mathbf{S}\,\mathbf{H}\,\mathbf{X} + \mathbf{N} \tag{6.2}$$

where $\mathbf{S}$ is a diagonal matrix with the scales on its diagonal. If properly defined, the scales can capture the system uncertainties. The GIC real data may be used to find such scales as described in Algorithm 6. In the algorithm, $Diag()$ of a vector is a diagonal matrix with the vector's entries on its diagonal, $\vec{1}$ is an all-one vector, $Sum()$ of a matrix returns the sum of all its entries and $K$ is the number of measurements.

The coefficient matrix depends on the network topology and resistances and its accuracy depends on the available network information. Most of the network parameters required for constructing the coefficient matrix are part of the standard power flow models and are accurately

**Algorithm 6** Scales Calculation

**procedure** SCALES CALCULATION($\mathbf{Y}$, $\mathbf{H}$)
    Initialize all the priori scales to one: $\mathbf{S} = Diag(\vec{1})$.
    Initialize the posteriori scales to zero: $\mathbf{S}^+ = Diag(\vec{0})$.
    Define the convergence tolerance, $\varepsilon$.
    **while** $\mid \mathbf{S}^+ - \mathbf{S} \mid > \varepsilon$ **do**
        Update the priori scales by $\mathbf{S} = \mathbf{S}^+$
        Estimate the E-field using:
            $\hat{\mathbf{X}} = (\mathbf{H}^T\mathbf{S}^T\mathbf{S}\mathbf{H})^{-1}\mathbf{H}^T\mathbf{S}^T\mathbf{Y}$.
        Calculate the posteriori scales by:
            $\mathbf{S}^+ = \text{Diag}(\mathbf{Y})\text{Diag}^{-1}(\mathbf{H}\hat{\mathbf{X}})$.
        Normalize the scales by $\mathbf{S}^+ = \frac{K\mathbf{S}^+}{Sum(\mathbf{S}^+)}$.
    **end while**
    **return S**
**end procedure**

available. The only piece of information which may not be available, but has high impacts is the substation grounding resistance, which is the effective grounding resistance of the substation and includes the ground grid and the emanating ground paths due to shield wire grounding. Techniques are available in the literature to measure this parameter [46], yet many factors can compromise the measurement and consequently introduce error to the GIC model validation. First, external objects such as water pipeline and adjacent railroad tracks distort the earth potential contours. Second, sources of dc current such as dc railroad tracks, pipelines cathodic protection systems and dc transmission lines produce stray currents which interfere with the grounding resistance measurements. Third, the resistance of the electrodes used for the measurements can introduce error if the substation being tested has low resistivity. Last, the grounding resistance mostly depends on the humidity, salt level or temperature and therefore is time-variant. Accurate measurement of the grounding resistance is very challenging and the available data (if any) is often inaccurate. Assigning the proper scales to the substation accounts for the inaccuracy of its grounding resistance.

The scales can be used to evaluate how well the GICs at a particular transformer agree with the model. In practice, not all the measurements conform to the model and some of the readings may exhibit different behavior. A possible reason for such divergent behaviors is non-uniform E-field. The linear GIC model is valid only when the E-field is uniform over the investigated area. When the geographic location of a transformer is too far from the others, its E-field may differ and its

GIC will not agree with the model. The proposed scale estimation technique detects the outlier measurements by assigning them zero scale and eventually excludes them from the dataset. An example of using the scales to detect outliers will be provided later.

Compared to the SVD-based analysis presented in [59], the proposed framework has several advantages owing to the additional network parameters. First, the proposed framework can validate the measurements independently and identify those that do not conform to the model, whereas the SVD analysis determines the validity of the measurements all together without providing any insight on the individual measurements. Second, the proposed method provides additional tools for validating the parameter accuracy. The method utilizes the network parameters to estimate the E-field. Hence, the agreement between this estimation and the one from the magnetic field data validates the accuracy of the assumed parameters. Last, the proposed model provides more accurate E-field estimation than the SVD-based one, which makes the validation framework built upon it more effective. Numerical results indicate that the first left singular of the SVD analysis perfectly captures the eastward E-field, yet the second left singular fails to estimate the northward E-field accurately. The comparison between the two methods will be provided later through case studies as well as real data analysis, and the advantages of the proposed technique discussed here will be demonstrated.

## 6.4 Numerical Results Using a Test Case

In this section and the next, the effectiveness of the proposed validation technique is evaluated. This section uses the fictitious 20-bus system from [38], whereas in Section 6.5 the technique is evaluated using actual data GIC neutral currents for five transformers located in the ATC footprint for a GMD that occurred on March $9$, 2012. For consistency, the same March $9$, 2012, data will be used with the 20-bus case.

On March $9$ the geomagnetic storm began at 2:00 UTC and reached a very high level in the following hours. The magnetic field data used here are from values measured at the US Geological Survey (USGS) Fredericksburg Geomagnetic Observatory, located in the US at a latitude/longitude of $38.205°N$, $77.373°W$. The reason for choosing this observatory is, again, to maintain

consistency with the results in Section 6.5. The transformers used in Section 6.5 are located in the ATC footprint and Fredericksburg is the closest observatory to these transformers.

The E-field obtained from the Fredericksburg magnetic field is enforced on the system and the induced GICs are determined by solving the GIC flows using PowerWorld Simulator with the GIC add-on. White Gaussian random noise with signal-noise-ratio (SNR) equal to $20$dB is added to the ideal GICs to simulate the system noise, and the synthetic measurements are obtained.

To evaluate the performance of the model validation framework under different uncertainties, three scenarios are considered, each focusing on one type of uncertainty:

**1. Inaccurate Coefficients Scenario:** In this scenario, the available coefficients at the eighth and ninth transformers are two times larger than the actual ones ($100\%$ error). This could be caused by the inaccurate substation grounding resistances. In practice, the coefficients may have much lower error and this study considers the worst case scenarios.

**2. Outliers Scenario:** In this scenario, the measurements at the eighth and ninth transformers are enforced to be outliers. Outliers are considered to be measurements which are generated by a different E-field. The E-field data at The Natural Resources Canada (NRCan) Ottawa Geomagnetic Observatory is used to simulate the outliers whereas the normal measurements are generated by the Fredericksburg data. Ottawa observatory is located in Canada at a latitude/longitude of $45.403°N$, $75.552°W$.

**3. Low Uncertainty Scenario:** This scenario considers the ideal case when the substation grounding resistances are accurate and no outlier exists in the measurements.

The transformer scales can account for the inaccurate coefficients. Figure 6.1 illustrates the scales under the first scenario where the assumed coefficients at the eighth and ninth transformers are double the actual ones. According to the figure, the scales for these transformers take the value of 0.5 to compensate for this inaccuracy. A correct estimate of the coefficients can be obtained through multiplying the assumed coefficients by their corresponding scales as shown in Fig. 6.2.

The transformer scales can be used to detect the measurement outliers as illustrated in Fig. 6.3. The readings from the eighth and ninth transformers are enforced to be outliers and the scale estimation technique successfully detects them and eliminates them from the model by assigning them zero scales.

The 20-bus system has two shunt capacitors at bus 4 and 16. Numerical results indicate that

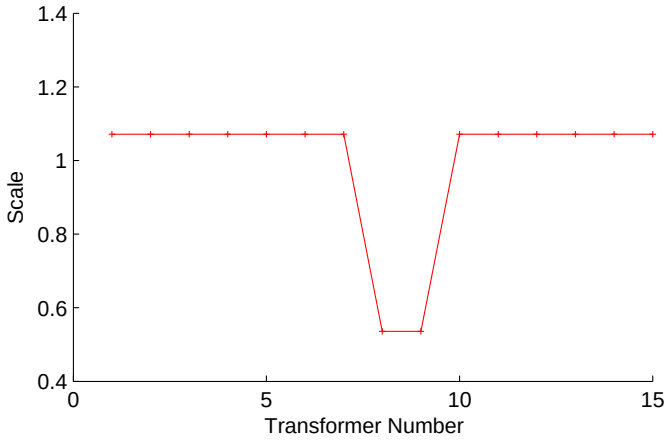


Figure 6.1: Transformer scales under the inaccurate coefficients scenario.

disconnecting these capacitors does not affect the proposed framework. This is because the GIC calculation is based on steady state dc analysis in which the capacitors act as open circuit. Hence, disconnecting them does not change the GIC model. The effect becomes significant when AC analysis is performed as opposed to dc. Power flow is solved including GICs and it is observed that connecting the shunt capacitors provides reactive power support and improves the voltage profile. The framework is robust to power filters and static synchronous compensator (STATCOM) devices as well since they only affect the AC analysis and not the dc.

Next, the performance of the proposed model is compared with the SVD-based technique presented in [59]. Table 6.1 presents the accuracy of the two methods in estimating the E-field. For reference, the results for the conventional model in (3.14) are also included. Pearson correlation coefficient is used to measure the correlation between the estimated and the actual E-field with the following definition:

$$\rho_{X,Y} = \frac{\text{cov}(X,Y)}{\sigma_X \sigma_Y} \tag{6.3}$$

where $\rho_{X,Y}$ and $\text{cov}(X,Y)$ are the Pearson correlation and covariance between signals $X$ and $Y$, respectively, and $\sigma$ is the standard deviation. The comparison is performed for the three uncertainty scenarios described earlier, which are Inaccurate Coefficients, Outliers, and Low Uncertainty. These scenarios are denoted by "Scen1", "Scen2" and "Scen3" in the table, respectively. In

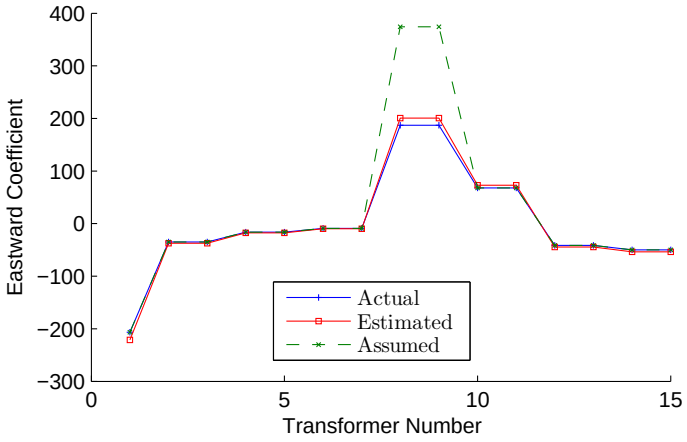


Figure 6.2: Correcting the inaccurate coefficients through the scales.

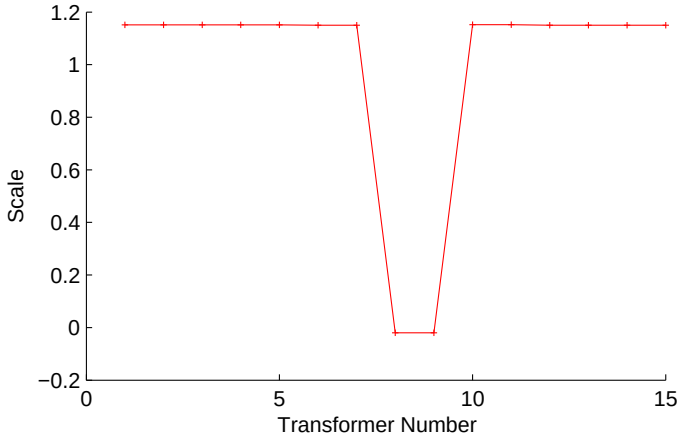


Figure 6.3: Transformer scales under the outlier scenario.

the east direction, all three methods estimate the E-field accurately under all three uncertainty scenarios and their corresponding correlation coefficients are always larger than 0.92. For the northward E-field, the proposed model and the conventional one provide accurate estimation, whereas the estimate from the SVD-based technique is not accurate with its correlation coefficient reaching as low as 0.59.

Figure 6.4 illustrates the actual E-field in east direction as compared with the estimates obtained from the proposed model and the SVD analysis. The fields are scaled to have unit Euclidean norm.

Table 6.1: Accuracy Comparison of the E-field Estimation Techniques for the Test Case

| Estimation Technique | Eastward E-Field | | | Northward E-Field | | |
|---|---|---|---|---|---|---|
| | Scen1 | Scen2 | Scen3 | Scen1 | Scen2 | Scen3 |
| Proposed | 1.000 | 1.000 | 1.000 | 1.000 | 1.000 | 1.000 |
| Conventional | 0.997 | 0.992 | 1.000 | 0.999 | 0.998 | 1.000 |
| SVD | 0.974 | 0.927 | 0.974 | 0.710 | 0.591 | 0.710 |

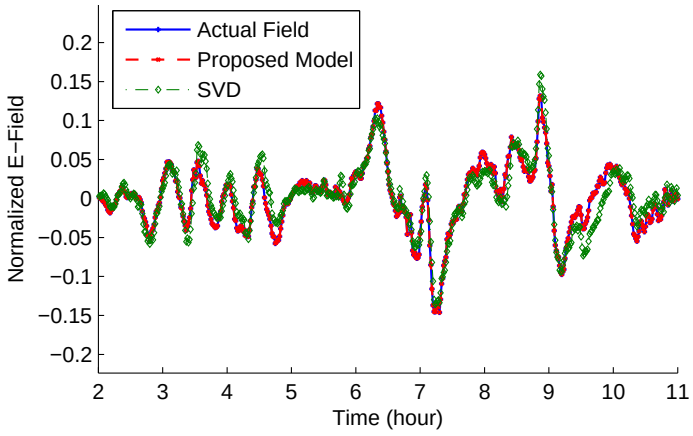


Figure 6.4: Comparison of the eastward E-field estimation using different methods for the test case.

The agreement between the estimated and actual fields verifies the accuracy for both methods. Figure 6.5 demonstrates similar comparison for E-field in north direction. In this direction, the estimate from the proposed model has extremely high agreement with the actual field whereas the SVD analysis fails to provide good accuracy. The estimate from the conventional model is not included in Fig. 6.4 and Fig. 6.5 for better clarity, as it is perfectly aligned with the estimate from the proposed model. The E-field estimated by the conventional model differs from that estimated by the proposed model only by a scaling factor, and hence the normalized fields in the figures are aligned.

The last validation test is to study the accuracy of different techniques in estimating the individual GIC measurements. The E-fields estimated by the conventional and proposed model are used in their corresponding GIC flow equations, which are (3.14) for the conventional model and (6.2) for

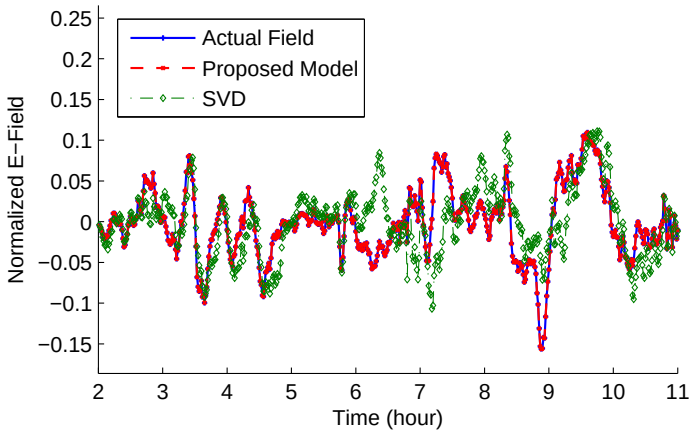


Figure 6.5: Comparison of the northward E-field estimation using different methods for the test case.

Table 6.2: Percentage Error Norm in Estimating GICs Based on Different Techniques

| Estimation Technique | Scen1 | Scen2 | Scen3 |
|---|---|---|---|
| Proposed | 4.91% | 5.22% | 5.01% |
| Conventional | 48.29% | 66.45% | 5.01% |
| SVD | 4.91% | 5.21 % | 5.00% |

the proposed one, and the estimated GICs are obtained. This estimation is then compared with the actual GICs which was initially used to estimate the E-field. The SVD-based technique estimates GICs through rank-2 approximation. Table 6.2 presents the estimation error for the investigated techniques with error defined as

$$Error = \frac{\|\hat{\mathbf{Y}} - \mathbf{Y}\|_F}{\|\mathbf{Y}\|_F} \tag{6.4}$$

where $\hat{\mathbf{Y}}$ is the matrix of estimated GICs and $\|\cdot\|_F$ is the Frobenius norm. It is observed that the SVD analysis and the proposed model estimate the GICs accurately for all uncertainty scenarios. The conventional model estimates the GICs accurately under the ideal scenario, but its estimation error increases up to 66% in the presence of grounding resistance uncertainty or outliers.

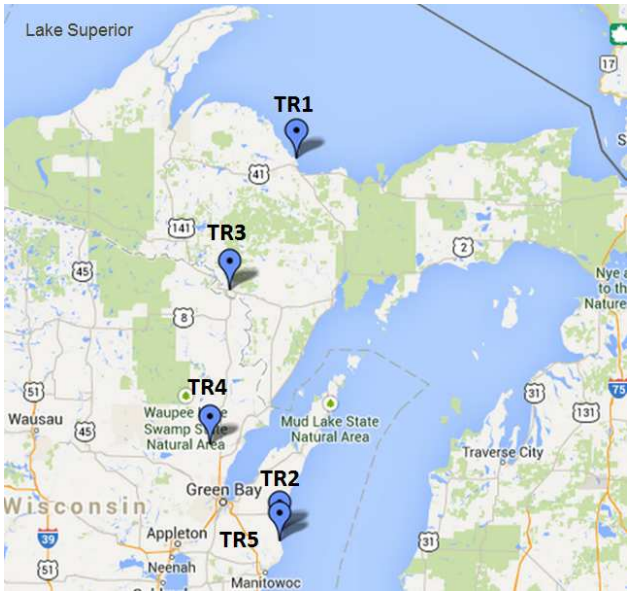


Figure 6.6: Geographic location of the investigated ATC transformers.

## 6.5 Numerical Results for Real Data

In this section, the GIC model is validated using real data measurements provided by ATC. This study focuses on the neutral current measurements of five transformers near the Wisconsin/Michigan area with the locations illustrated in Fig. 6.6. The geographical proximity of the Fredericksburg magnetometer to the ATC footprint makes using its data relevant to this study.

The GIC data for the March 9, 2012, storm is chosen primarily for the analysis, as plotted in Fig. 6.7. The transformers are indexed from 1 to 5. The highest GIC observed at these transformers is 27 A. Records of previous storms indicate that GICs can reach up to 330 A for more vulnerable locations and more severe storms [10]. Such observations indicate that the existing infrastructure including the shielding techniques does not protect the substations from GMDs. The GICs are derived from the E-field induced over long transmission lines and are sunk into the ground through the substation grounding. The shielding techniques may protect a small range, but fail to block the GICs coming from long transmission lines. It is observed that at the transformers TR4, and TR5, the absolute value of the current is measured and the direction is missing. An effective data preprocessing technique is used to retrieve the direction as presented in the following.

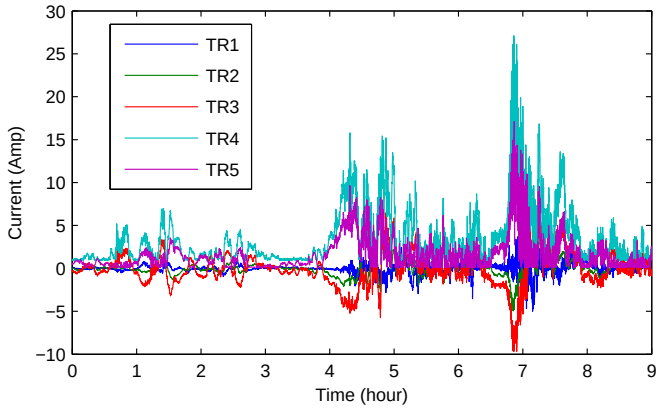


Figure 6.7: GICs at investigated ATC transformers on March 9, 2012.

### 6.5.1 Data Preprocessing

The set of GIC measurements may be divided in to two groups: A) the measurements that have the direction information (directed GICs) and B) the measurements which are missing direction (undirected GICs). The matrix containing the GICs may be rearranged to separate the directed measurements from the undirected ones as expressed in:

$$\mathbf{Y} = \left[\frac{\mathbf{Y}_D}{\mathbf{Y}_U}\right] \quad , \quad \mathbf{H} = \left[\frac{\mathbf{H}_D}{\mathbf{H}_U}\right] \tag{6.5}$$

where $\mathbf{Y}_D$ and $\mathbf{Y}_U$ are the matrices of the directed and undirected GICs, respectively, and $\mathbf{H}_D$ and $\mathbf{H}_U$ are their corresponding coefficient matrices. The electric field can be estimated from the directed GICs using least squares estimation:

$$\hat{\mathbf{E}}^{LS} = (\mathbf{H}_D^T \mathbf{H}_D)^{-1} \mathbf{H}_D^T \mathbf{Y}_D \tag{6.6}$$

Once the E-field is determined, an initial estimate of the undirected GICs is obtained through:

$$\hat{\mathbf{Y}}_U^- = \mathbf{H}_U \hat{\mathbf{E}}^{LS} \tag{6.7}$$

Finally, the direction of this estimate is utilized to retrieve the direction of the actual measurement as given by

$$\hat{\mathbf{Y}}_U^+ = sign(\hat{\mathbf{Y}}_U^-) \cdot \mathbf{Y}_U \tag{6.8}$$

where $\hat{\mathbf{Y}}_U^+$ is the final estimate of the undirected GICs, and $\hat{\mathbf{Y}}_U^-$ is the initial estimate.

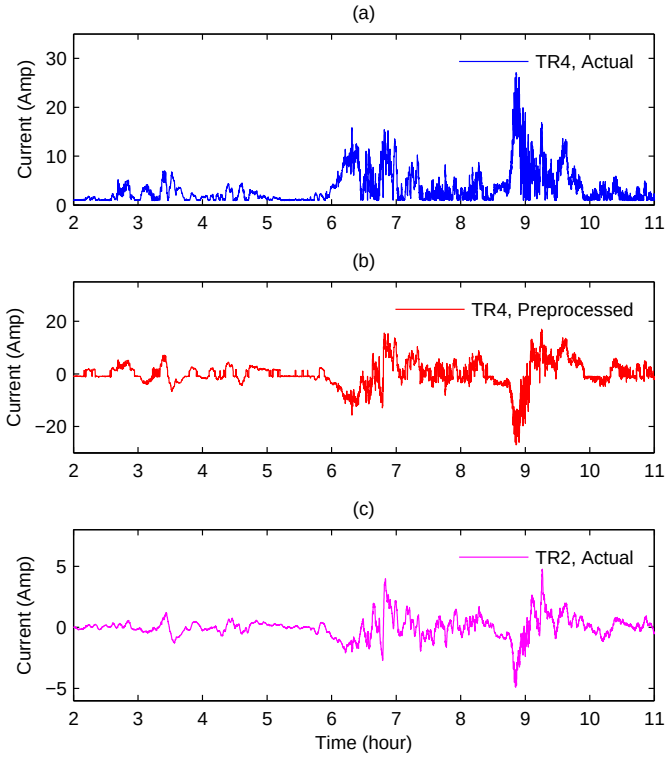


Figure 6.8: Proposed data preprocessing technique. (a) Actual and (b) preprocessed data for transformer TR4. (c) Actual data for the transformer TR2.

The proposed technique is applied to the measurements at TR4 and TR5, and their directions are retrieved. The actual data at TR4 and its preprocessed result is presented in Fig. 6.8. For reference, the GIC at TR2 is presented as well. The preprocessed data has strong correlation with the data at TR2 which validates the effectiveness of this technique.

Table 6.3: Grounding Resistance and Coefficients of Investigated ATC Transformers

| Name | $H^E$ | $H^N$ | $R_g$ |
|---|---|---|---|
| TR1 | 20.816 | 25.831 | 0.168 |
| TR2 | 21.5 | 34.4 | 0.222 |
| TR3 | -13.8 | 4.2 | 0.168 |
| TR4 | -14.875 | 18.818 | 0.181 |
| TR5 | 3.2 | 2.14 | 0.148 |

### 6.5.2 GIC Model Validation

To perform the GIC model validation, first the transformers coefficients are calculated. The investigated transformers are part of the Eastern Interconnect (EI). The EI system is simulated in PowerWorld Simulator using the available network parameters and the coefficients are calculated based on the method described earlier. Unfortunately, the grounding resistances are not available for the EI system and a simplistic model was used to estimate their values. The assumed grounding resistances and the resulting coefficients are presented in Table 6.3.

In theory, all parts of the network should be considered for calculating the coefficients. However, studies show that the GIC impacts are localized and considering only the nearby areas provides sufficient accuracy. In the current study, all the EI areas are included in the calculations, yet later investigations demonstrated that this was not necessary and considering only the areas near Wisconsin provided sufficient accuracy.

There are two GIC models to be validated: The conventional model in (3.14) and the modified one in (6.2) with the introduced scales. The model validation framework is used to evaluate the effectiveness of these models through real data analysis.

Figure 6.9 illustrates how well each individual measurement agrees with the conventional model. First, the E-field is estimated from the GIC measurements through the conventional model as proposed in (10.2). The estimated E-field is multiplied by the transformer coefficients to get the estimated GIC using $\mathbf{I} = \mathbf{HE}$. This estimation is then compared with the actual measurement. According to the figure, the estimated and actual GICs agree very well at TR2, TR3, and TR4. The estimate at TR1 does not agree well with the actual GIC, but still has the same order of magnitude. The worst agreement is at TR5 where the estimate is almost zero, even though the actual GIC

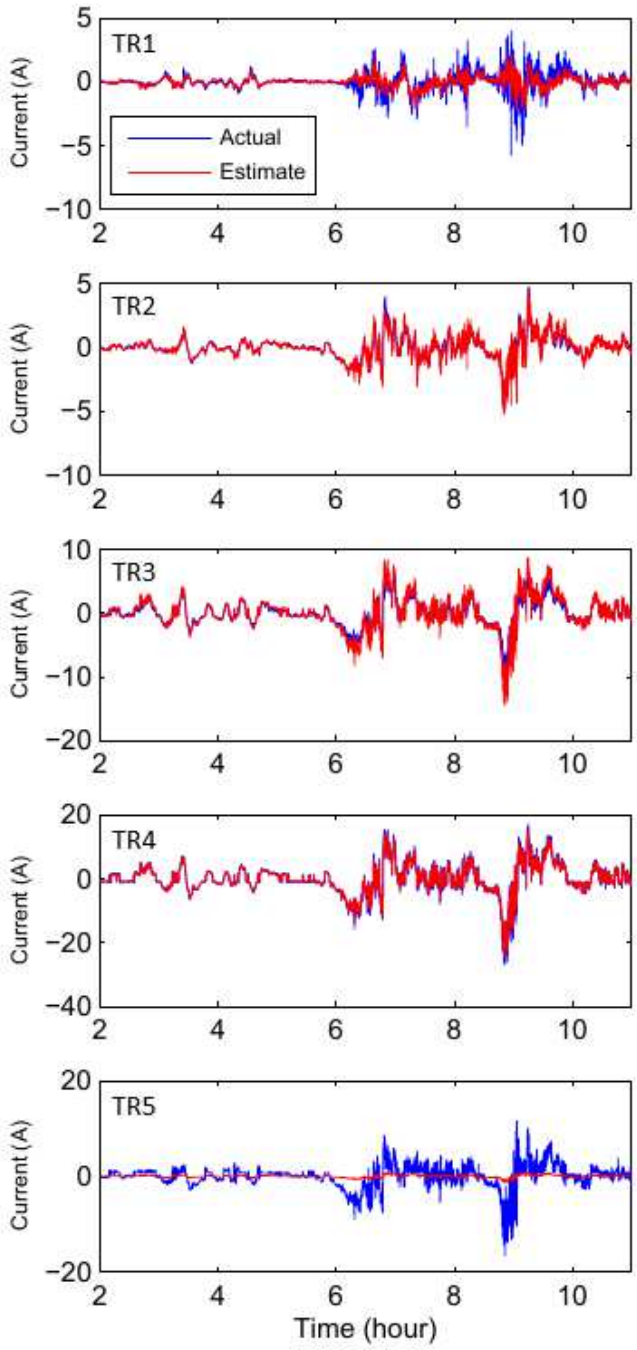


Figure 6.9: Accuracy of the conventional model in estimating the GICs.

reaches up to 20 A. Going back to Table 6.3, the coefficients for TR5 are 3.2 and 2.14 in east and north direction, respectively. These values are very small compared to the other transformers; e.g., the coefficients of TR1 are 20.8 and 25.8. TR5 coefficients are expected to be larger since its

Table 6.4: Pearson Correlation Coefficients Between the GICs

| Name | TR1 | TR2 | TR3 | TR4 | TR5 |
|---|---|---|---|---|---|
| TR1 | 1 | -0.166 | 0.072 | 0.117 | 0.051 |
| TR2 | -0.166 | 1 | 0.791 | 0.652 | 0.651 |
| TR3 | 0.072 | 0.791 | 1 | 0.700 | 0.653 |
| TR4 | 0.117 | 0.652 | 0.700 | 1 | 0.883 |
| TR5 | 0.051 | 0.651 | 0.653 | 0.883 | 1 |

measured GIC is in the same order as the other transformers. This casts doubt on the accuracy of the assumed coefficients. The modified model may be used to correct the inaccurate coefficients through the scales as will be demonstrated shortly.

The modified model accounts for the system uncertainties and in particular, the inaccurate coefficients. Figure 6.10 compares the estimated GICs obtained from the modified model with the actual measurements. This time, the estimated GIC at TR5 has high agreement with the actual one, which confirms that the modified model accounts for the inaccurate coefficients by assigning a larger scale to TR5. Another interesting observation is that the estimated GIC at TR1 is close to zero. This is because the modified model assigns a very small scale to TR1 which reduces the estimated GIC to almost zero. Recall that the modified model assigns zero scales to the outlier measurements as was demonstrated through an example in previous section (see Fig. 6.3). Similar to the example case, the measurement at TR1 has irregularity, and hence gets a zero scale. It is clear in Fig. 6.10 that all the measurements are correlated except for TR1. This can be confirmed using the Pearson correlation coefficients as presented in Table 6.4. The value at row TR$X$ and column TR$Y$ of the table is the coefficient between the GICs at transformers $X$ and $Y$. Pairwise comparison of these coefficients confirms the weak correlation for TR1.

Many factors could contribute to zeroing out the scale of a transformer. One possible reason is having a different E-field than the rest of the network, in which case the uniform E-filed assumption does not hold and the GIC model is no longer valid. Hence, the transformer with a different E-field is excluded from the model by setting its scale to be zero. TR1 is located in the northern part of Michigan and is on the shore of Lake Superior as shown in Fig. 6.6. Its higher latitude as well as the nearby body of water could result in a different E-field and eventually zero out the scale.

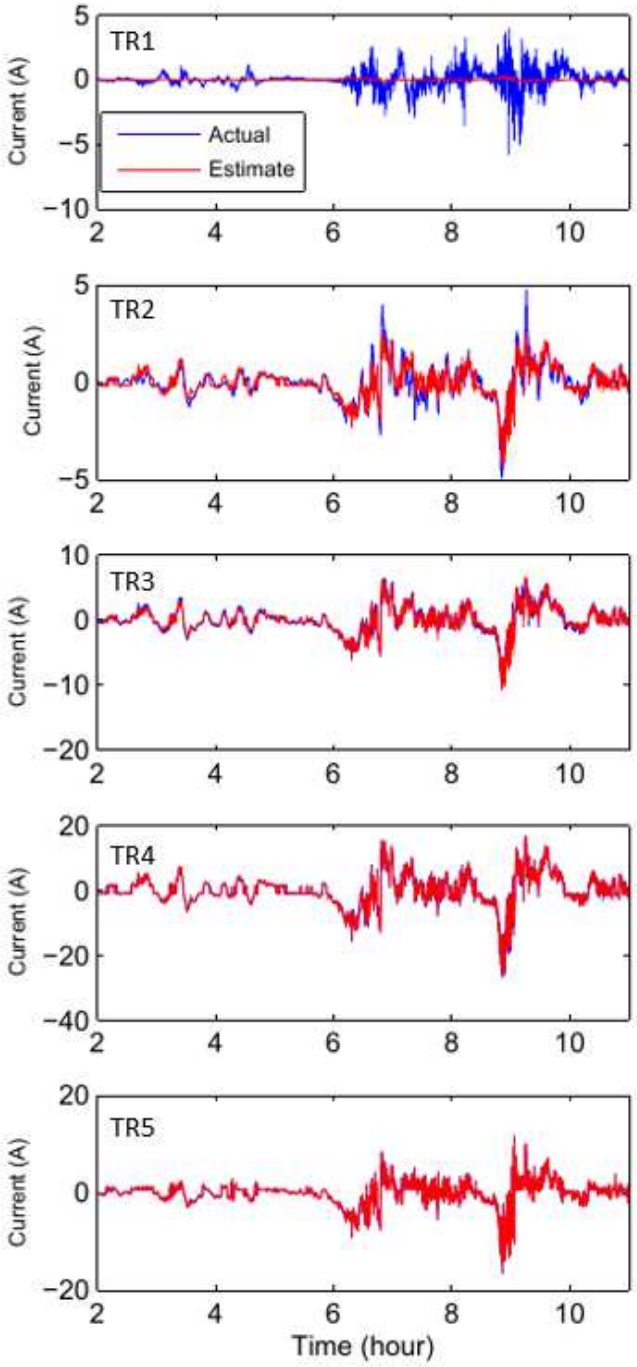


Figure 6.10: Accuracy of the modified model in estimating the GICs.

The ultraviolet emission measurements obtained from Special Sensor Ultraoviolet Spectrograph Imager (SSUSI, a remote-sensing instrument mounted on a satellite) can provide auroral environ-

Table 6.5: Accuracy Comparison of the E-field Estimation Techniques for the ATC system

| Estimation Technique | Eastward Field | Northward Field |
|---|---|---|
| Proposed | 0.629 | 0.740 |
| Conventional | 0.656 | 0.737 |
| SVD | 0.630 | 0.016 |

mental data records (EDRs) with information on the electron energy flux (Q), the magnetic field lines and the auroral boundaries during a solar storm [91]. Analysis of the auroral EDRs for the March 9, 2012, storm indicates that the aurora moved to the lower latitudes during the storm. The aurora even hit the Ottawa magnetic observatory as confirmed with its magnetic field measurements. This suggests that the irregularity at TR1 could be due to the magnetic disturbances associated with the aurora. Further exploration into the E-field at the transformer TR1 and why its scale vanishes will be an interesting future study.

The performance of the proposed technique is compared with the SVD-based approach. The E-field estimated from the magnetic data is compared with the estimate from GIC measurements using both methods, and their Pearson correlation coefficients are presented in Table 6.5. For reference, the results for the conventional GIC model in (3.14) are also included in the table. All three methods estimate the eastward E-field quite accurately with their correlation coefficients around 0.6. The proposed model and the conventional one estimate the northward E-field with relatively good accuracy, whereas the estimate from the SVD-based approach is extremely inaccurate with its correlation coefficient equal to 0.016.

Figure 6.11 presents the eastward E-field obtained from the magnetic data as compared with the estimate from the GIC measurements using both the proposed model and the SVD analysis. The fields are scaled to have unit Euclidean norm. The estimate from both methods agrees well with that from the magnetic data. Figure 6.12 demonstrates a similar comparison for the E-field in the north direction. In this direction, the estimate from the proposed model agrees relatively well with that from the magnetic data, whereas the estimate from SVD analysis has significant mismatches. For better clarity, the estimate from the conventional model is not included in Fig. 6.4 and Fig. 6.5 as it is perfectly aligned with the estimate from the proposed model.

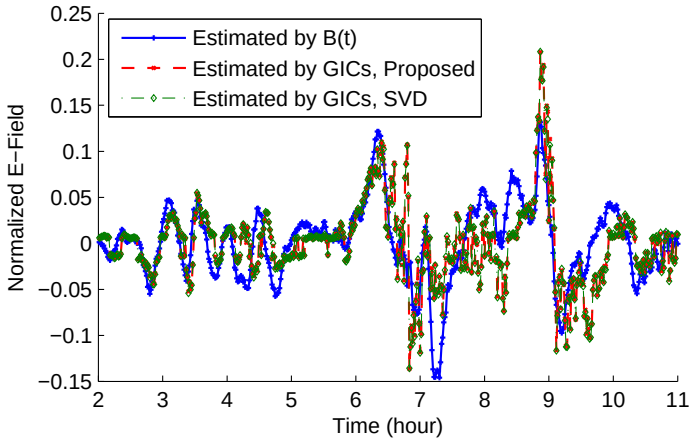


Figure 6.11: Comparison of the eastward E-field estimation using different methods for the ATC system.

## 6.6 Conclusions

In this chapter, a validation technique is presented which utilizes the network parameters to provide stronger validation tools. This method introduces the transformer scales to account for the system uncertainties and provides the extra capability of detecting the outlier measurements. The proposed validation framework is demonstrated using a small case study and its performance is extensively studied under different scenarios. More interesting real data validation is conducted using the GIC measurements provided by ATC. The data from five transformers are validated, the inaccurate model parameters are adjusted through the scales, and finally the existing outlier in the set of the measurements is successfully detected.

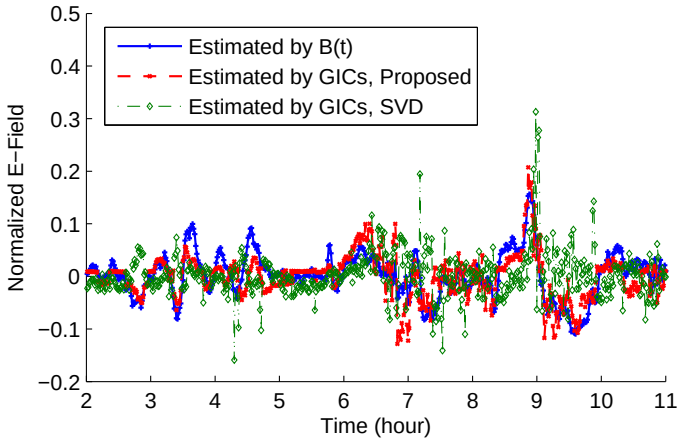


Figure 6.12: Comparison of the northward E-field estimation using different methods for the ATC system.

# CHAPTER 7

# SUBSTATION GROUNDING RESISTANCE ESTIMATION FOR IMPROVED GMD MODEL VALIDATION

## 7.1 Introduction

This chapter focuses on estimating the substation grounding resistance to improve the modeling of geomagnetically induced currents (GICs). Grounding resistances are not included in the standard power flow models, and their approximate values are often used for performing GIC studies. This chapter provides an algorithm to estimate the resistances from the GIC measurements. This algorithm calculates the linear sensitivity factors of the GICs around the local grounding resistive components and uses linear regression to solve for the resistances. The effectiveness of the proposed algorithm is demonstrated using both a small test case as well as a 62500-bus model of the North American Eastern Interconnection. The proposed technique reduces the uncertainties of the GMD model by providing more accurate grounding resistances. This improves the resiliency to GMDs through better assessment of the GICs and their risks.

The chapter is organized as follow: The algorithm for estimating the substation grounding resistance through GIC measurements is presented in Section 7.2. In Section 7.3, the dependency of the proposed technique on the E-field is identified and proper adjustments are considered to eliminate such dependencies. Section 7.4 discusses the practical issues with implementing the algorithm and a suitable framework is presented which simplifies the implementation. Section 7.5 demonstrates the proposed technique using a 20-bus test case, while the application on a large 62500-bus system is given in Section 7.6. Section 7.7 presents a conclusion and directions for future work.

## 7.2 Grounding Resistance Estimation

The grounding resistance error is described as the vector of the differences between the actual grounding resistances and the assumed ones as given by

$$\partial R = R - R_0 \tag{7.1}$$

where $R$ is the vector containing the actual grounding resistance of all the substations and $R_0$ is the vector of the assumed grounding resistances.

The sensitivity of the GIC to the grounding resistance is defined as the percent variation of the current in terms of the percent variation of the grounding resistance as given by [45]:

$$s_{ij} = \frac{\partial(\%I_{GIC,i})}{\partial(\%R_j)} = \frac{(\partial I_{GIC,i}/I_{GIC,i})}{(\partial R_j/R_j)} \tag{7.2}$$

In this study, the actual variation is used instead of the percent variation to simplify the problem formulation: $s_{ij} = \partial I_{GIC,i}/\partial R_j$. For a set of $K$ substations, one can build the $K \times K$ sensitivity matrix $S = \{s_{ij}\}$ where $s_{ij}$ is the sensitivity of the GIC at substation $i$ to the grounding resistance of substation $j$. The sensitivity depends on the E-field direction and the sensitivity matrix is defined for a particular direction. Let $\mathbf{S}^N$ and $\mathbf{S}^E$ denote the sensitivity matrices for northward and eastward E-fields. The grounding resistance error modifies the coefficient matrix by

$$\begin{cases} H^N \leftarrow H^N + \mathbf{S}^N \partial R \\ H^E \leftarrow H^E + \mathbf{S}^E \partial R \end{cases} \tag{7.3}$$

Substituting the updated coefficient matrix in the GIC model gives rise to

$$[(H^N + \mathbf{S}^N \partial R) \mid (H^E + \mathbf{S}^E \partial R)] \times \mathbf{E} = \mathbf{Y} \tag{7.4}$$

Defining the matrix $\mathbf{Y}_b := \mathbf{HE}$, (7.4) can be rewritten as:

$$(E^E \otimes \mathbf{S}^E + E^N \otimes \mathbf{S}^N)^T \partial R = vec(\mathbf{Y} - \mathbf{Y}_b) \tag{7.5}$$

where $\otimes$ is the Kronecker product and $vec()$ is the vectorization function. Defining the matrix $\mathbf{A} := (E^E \otimes \mathbf{S}^E + E^N \otimes \mathbf{S}^N)^T$ generates an overdetermined system with $\partial R$ as the unknown:

$$\mathbf{A}\partial R = vec(\mathbf{Y} - \mathbf{Y}_b) \tag{7.6}$$

Least squares estimation can be used to estimate $\partial R$ as given by

$$\begin{aligned} \hat{\partial R}^{LS} &:= \arg\min_{\partial R} \|vec(\mathbf{Y} - \mathbf{Y}_b) - \mathbf{A}\partial R\|_2 \\ &= (\mathbf{A}^T\mathbf{A})^{-1}\mathbf{A}^T vec(\mathbf{Y} - \mathbf{Y}_b) \end{aligned} \tag{7.7}$$

The coefficient modification presented in (7.3) is valid only for small values of $\partial R$ as the sensitivities are linear approximations. However, $\partial R$ may be large when the grounding resistance data is inaccurate or unavailable. To tackle this, the process can be performed iteratively until $\partial R$ converges to zero. The resistances obtained at each iteration are used as the initial values for the consecutive iteration. The steps of this iterative algorithm are described in Algorithm 7.

**Algorithm 7** Grounding Resistance Estimation with E-field

**procedure** GROUNDING RESISTANCE ESTIMATION WITH E-FIELD($\mathbf{Y}$, $\mathbf{X}$, $R_0$)
    Initialize the estimated resistances $\hat{R}$ to $R_0$
    Define the convergence tolerance, $\varepsilon$
    Initialize $\partial R$ to the all-ones vector
    **while** $\mid \partial R \mid > \varepsilon$ **do**
        Calculate the sensitivities $\mathbf{S}^N$ and $\mathbf{S}^E$
        Calculate $\mathbf{Y}_b = \mathbf{HE}$
        Calculate $\mathbf{A} = (E^E \otimes \mathbf{S}^E + E^N \otimes \mathbf{S}^N)^T$
        Solve for $\partial R$ through $\partial R = (\mathbf{A}^T\mathbf{A})^{-1}\mathbf{A}^T vec(\mathbf{Y} - \mathbf{Y}_b)$
        Update the resistances by $\hat{R} = \hat{R} + \partial R$
    **end while**
    **return** $\hat{R}$
**end procedure**

The inputs of the algorithm are the GIC measurements $\mathbf{Y}$, the E-field $\mathbf{E}$ and the available grounding resistances $R_0$. If no resistance data is available, $R_0$ is represented by a vector of random values within the range of $0.05$ and $0.3$ (reasonable range for the grounding resistance). The output of the algorithm is $\hat{R}$, which is the vector of estimated grounding resistances.

In theory, the estimated resistance obtained from the proposed technique is the same as the one measured by the conventional methods. The proposed algorithm serves as an alternative solution when measuring the resistances is not feasible for practical reasons. There are several challenges associated with the measurement-based approaches. First, external objects such as water pipeline and adjacent railroad tracks distort the earth potential contours. Second, sources of dc current such as dc railroad tracks, pipelines cathodic protection systems and dc transmission lines produce stray currents which interfere with the grounding resistance measurements. Third, the resistance of the electrodes used for the measurements can introduce error if the substation being tested has low resistivity. Last, the grounding resistance mostly depends on the humidity, salt level or temperature and therefore is time-variant and may change significantly with seasons. The conventional grounding resistance measurements are usually performed every five to ten years and even the most recent one might not capture the current state of the soil regarding its humidity, salt level or temperature. In contrast, the estimate from the GIC measurements is in semi-real time. Motivated by the negative impacts of GMDs, electric utilities are investing in GIC monitoring enhancement. More GIC sensors are being installed in the grid which widens the applications of the proposed technique.

### 7.2.1 Sensitivity Calculation

The algorithm presented earlier requires calculation of the sensitivity matrices at each iteration. There are analytical techniques to derive the sensitivities as functions of the network parameters [45]. Alternatively, one can follow the sensitivity definition to calculate the sensitivities as described in Algorithm 8. The algorithm takes the grounding resistances as input. This allows calculating the sensitivities in each iteration after the grounding resistances are updated.

## 7.3 Dependency on the Electric Field

The problem with the proposed technique is that it depends on the E-field whereas only the GIC data is assumed to be available, not the E-field. To address this issue, first, the E-field is estimated through the GICs and then is used in the algorithm. Since the grounding resistances are

**Algorithm 8** Sensitivity Calculation

**procedure** SENSITIVITY CALCULATION($R$)
    Initialize the grounding resistances to $R$
    Enforce an eastward E-field to get $I^{E0}$.
    Enforce a northward E-field to get $I^{N0}$.
    **for** $n = 1$ to $n <$K **do**
        Increase the resistance of substation $n$ by 10%.
        Enforce an eastward E-field to get $I^{E}$.
        Enforce a northward E-field to get $I^{N}$.
        Calculate the $n^{th}$ column of the northward sensitivity matrix by $S_n^E = 10(I^E - I^{E0})/I^{E0}$
        Calculate the $n^{th}$ column of the northward sensitivity matrix by $S_n^N = 10(I^N - I^{N0})/I^{N0}$
        Set the resistance of substation $n$ back to default.
    **end for**
    **return** $\mathbf{S}^N$ and $\mathbf{S}^E$
**end procedure**

not available in the beginning and are going to be estimated later, a meaningful E-field estimation should be robust to the grounding resistance error. The appendix demonstrates that the ordinary LS method can successfully estimate the E-field up to scaling even when the grounding resistances are inaccurate:

$$\hat{\mathbf{E}}^{LS} := \arg\min_{\mathbf{E}} \|\mathbf{Y} - \mathbf{H}\mathbf{E}\|_2 = (\mathbf{H}^T\mathbf{H})^{-1}\mathbf{H}^T\mathbf{Y} \tag{7.8}$$

This estimation scales with the actual E-field, but the ratio is unknown. This uncertainty is included in the model through:

$$\mathbf{E} = \alpha\hat{\mathbf{E}} \Rightarrow \alpha\ vec(\hat{\mathbf{Y}}_b) + \mathbf{A}\partial R = vec(\mathbf{Y}) \tag{7.9}$$

where $\alpha$ is the unknown ratio between the estimated E-field and the actual one. $\hat{\mathbf{Y}}_b$ is similar to $\mathbf{Y}_b$ except that the estimated E-field is used in its definition instead of the actual one: $\hat{\mathbf{Y}}_b = \mathbf{H}\hat{\mathbf{E}}$. The system is augmented to include $\alpha$ as an additional unknown:

$$[\mathbf{A} \mid vec(\hat{\mathbf{Y}}_b)] \times \begin{bmatrix} \partial R \\ \hline \alpha \end{bmatrix} = vec(\mathbf{Y}) \tag{7.10}$$

Defining $\mathbf{x}_a := [\partial R \mid \alpha]^T$ as the augmented state and $\mathbf{A}_a := [\mathbf{A} \mid vec(\hat{\mathbf{Y}}_b)]$ as the augmented design matrix, least squares can be used to solve for $\partial R$ and $\alpha$ as given by

$$\begin{aligned}\hat{\mathbf{x}}_a^{LS} : &= \arg\min_{\mathbf{x}_a} \|vec(\mathbf{Y}) - \mathbf{A}_a\mathbf{x}_a\|_2 \\ &= (\mathbf{A}_a^T\mathbf{A}_a)^{-1}\mathbf{A}_a^T vec(\mathbf{Y}) \end{aligned} \tag{7.11}$$

Least squares provides the solution with the minimum Euclidean norm. However, it is better to minimize the Euclidean norm of $\partial R$, but allow $\alpha$ to take any value. To find the solution with this particular property, regularized least squares may be used as described in the following.

### 7.3.1 Regularized Least Squares

Ordinary least squares is the standard approach to solve the overdetermined system of equation

$$\mathbf{M}\mathbf{x} = b \tag{7.12}$$

where the sum of the squared residuals $\|\mathbf{M}x - b\|_2$ is minimized. Regularized least squares give preference to a particular solution with desirable properties by adding the regularization term as expressed by

$$\hat{\mathbf{x}} := \arg\min_{\mathbf{x}} \|\mathbf{M}\mathbf{x} - b\|_2 + \mu\|\mathbf{F}\mathbf{x}\|_2 \tag{7.13}$$

where $\mathbf{F}$ is suitably chosen to capture the desired regularization and $\mu$ is the penalty weight [92]. This forms a multi-objective optimization problem and its closed-form solution is given by

$$\hat{\mathbf{x}} = (\mathbf{M}^T\mathbf{M} + \mu\mathbf{F}^T\mathbf{F})^{-1}\mathbf{M}^T b \tag{7.14}$$

For the augmented system in (7.10), it is desired to enforce $\partial R$ to zero, but leave $\alpha$ unconstrained. This can be done by selecting $\mathbf{F}$ as a diagonal matrix with 1 on all its diagonal entries but the last

one as given by

$$\mathbf{F} = diag([\vec{\mathbf{1}}_{(1,S)}, 0]) \tag{7.15}$$

where $S$ is the number of substations. The algorithm for estimating the grounding resistance when the E-field is not available is summarized in the following:

**Algorithm 9** Grounding Resistance Estimation without E-field

**procedure** GROUNDING RESISTANCE ESTIMATION WITHOUT E-FIELD($\mathbf{Y}$, $R_0$)
    Initialize the grounding resistances $\hat{R}$ to $R_0$
    Estimate the E-field by $\hat{\mathbf{E}} = (\mathbf{H}^T\mathbf{H})^{-1}\mathbf{H}^T\mathbf{Y}$
    Define the convergence tolerance, $\varepsilon$
    Initialize $\partial R$ to the all-ones vector
    **while** $\mid \partial R \mid > \varepsilon$ **do**
        Calculate the sensitivities $\mathbf{S}^N$ and $\mathbf{S}^E$
        Calculate $\hat{\mathbf{Y}}_b := \mathbf{H}\hat{\mathbf{E}}$
        Calculate $\mathbf{A}_a := [(\hat{E}^E \otimes \mathbf{S}^E + \hat{E}^N \otimes \mathbf{S}^N)^T \mid vec(\hat{\mathbf{Y}}_b)]$
        Solve for $\partial R$ by $[\partial R \mid \alpha]^T = (\mathbf{A}_a^T\mathbf{A}_a)^{-1}\mathbf{A}_a^T vec(\mathbf{Y})$
        Update the resistances by $\hat{R} = \hat{R} + \partial R$
    **end while**
    **return** $\hat{R}$
**end procedure**

## 7.4 Algorithm Implementation

To implement the algorithm efficiently, parts of the computations are performed in a computation program like MATLAB and the rest in a commercial power system software like PowerWorld Simulator. The process involves repetitively running simulation in the power system software, collecting data and transferring it to the computation program for further analysis. With the actual algorithm, the intercommunication between the two programs is as follows: Store the grounding resistances in the computation program, simulate the network with the current resistances in the power system software, calculate the sensitivities, transfer to the computation program and calculate the new grounding resistances accordingly. Repeat the process until the grounding resistances converge. This process is illustrated in Fig. 7.1.

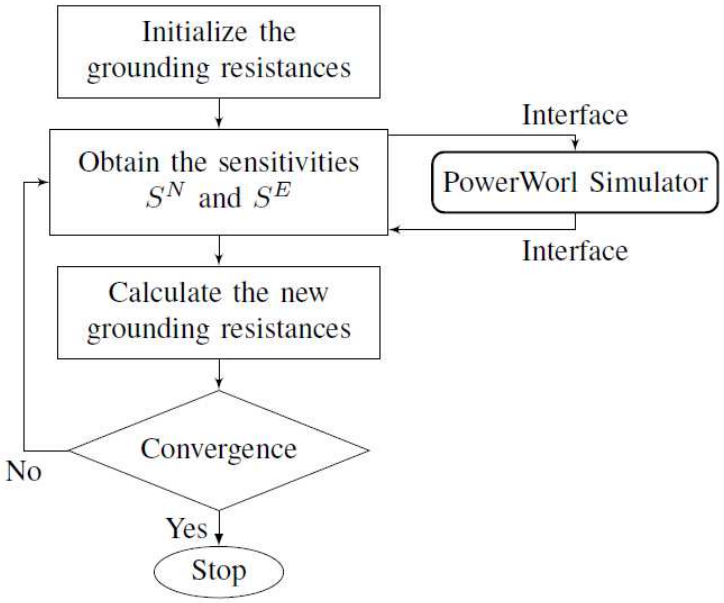


Figure 7.1: Resistance estimation algorithm environment interface.

The sensitivity calculation itself requires repetitive intercommunication as described in the following: Increase the grounding resistance of the $i^{th}$ substation by $10\%$, simulate the network with this set of grounding resistances in the power system software, save the GICs, transfer to the computation program and calculate the $i^{th}$ column of the sensitivity matrix. Repeat this process for all the substations to complete the sensitivity matrix calculation. This process is illustrated in Fig. 7.2.

It is extremely burdensome to manually transfer the data between the two programs. However, building an interface will eliminate the manual steps and automate the process. Component Object Model (COM) is a binary-interface standard for software components that allows intercommunication between different programs. COM objects are independent of the programming language which created them and if well-defined, any environment can reuse them with no knowledge of their internal implementation. This enables an environment to interface with any external program through accessing its COM object(s).

The Simulation Automation Server (SimAuto) allows interface between PowerWorld Simulator and many windows-based programming languages including MATLAB. SimAuto acts as a COM

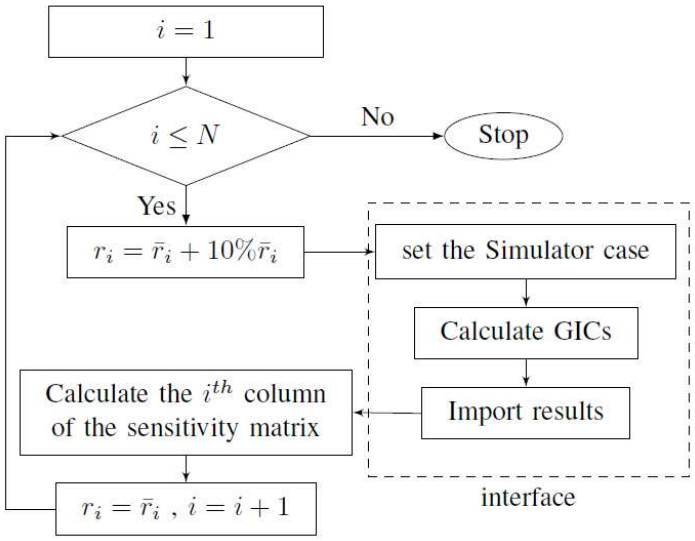


Figure 7.2: Sensitivity calculation environment interface.

object that can be utilized by the external program to access the data of a Simulator case, perform defined Simulator functions and collect the results. For the purpose of this paper, MATLAB is used as the computation program which interface with PowerWorld Simulator through SimAuto. The snippet of MATLAB code for establishing a connection with SimAuto and opening a case is as follows:

```
% establish connection
A = actxserver('pwrworld.SimulatorAuto');
pwFile = strcat(pwd,'\epri.PWB');
% open case
simOutput = A.OpenCase(pwFile);
```

SimAuto allows changing the parameters of a Simulator case through commands in the external computation program. For instance, the grounding resistance of a substation with the substation ID “21” is set to 1.1 using the following script code in MATLAB:

```
% change grounding resistance
type = 'Substation';
fields = {'SubNum','GICSubGroundOhms'};
values = {21,1.1};
simOutput = serv.ChangeParametersSingleElement ...
(type, fields, values);
```

SimAuto also offers the capability to execute Simulator functions through the external software. For example, the script code below enforces an E-field with unity magnitude and 90 degree direction to the simulator case and solves the GIC flow:

```
% calculate GIC
fileline = 'GICCalculate(1,90,NO)';
```

After changing the grounding resistance and calculating the GICs, it is desired to transfer the results from PowerWorld to MATLAB. Below is an example of importing the neutral current for the transformer between buses 17 and 18:

```
% transfer GIC
type = 'Transformer';
fields = {'BusNum','BusNum:1','LineCircuit',...
'GICXFNeutralAmps'};
output = serv.RunScriptCommand(fileline);
values = {17,18,1,1};
simOutput = serv.GetParametersSingleElement ...
(type,fields,values);
```

It is necessary that all the commands are defined properly and without any ambiguity. For example, to import the neutral current of a transformer, defining only the connecting buses is not enough if there is more than one transformer between those two buses. The line circuit should be specified as well in order to uniquely identify the transformer.

Table 7.1: Grounding Resistances of the 20-bus Test Case

| Name | Actual Resistance | Assumed Resistance | Error (%) |
|---|---|---|---|
| SUB1 | 0.20 | 0.31 | 53.53 |
| SUB2 | 0.20 | 0.14 | 31.21 |
| SUB3 | 0.20 | 0.26 | 27.72 |
| SUB4 | 1.00 | 0.90 | 9.56 |
| SUB5 | 0.10 | 0.03 | 70.00 |
| SUB6 | 0.10 | 0.17 | 72.83 |
| SUB7 | 0.10 | 0.16 | 61.87 |

## 7.5 Numerical Results Using a Small Test Case

The effectiveness of the proposed method is validated though simulation. The 20-bus system in [38] is investigated. The substation grounding resistances are presented in Table 7.1. These values are not available to the algorithm and need to be estimated. Instead, the assumed resistances listed in the table are provided. The assumed grounding resistances have an average of $136\%$ absolute error with the error defined as

$$Error^{R_g} = \frac{\|R_0 - R\|_2}{\|R\|_2} \tag{7.16}$$

Synthetic GIC data is created by enforcing an E-field to the system and obtaining the induced GICs through solving the GIC flow in PowerWorld Simulator. For the purpose of this study, the E-field measured during an actual geomagnetic storm is used to maximize the likeness to real GIC measurements [81]. The E-field collected at Fredericksburg observatory during the March 9, 2012 storm is investigated. Fredericksburg observatory is located in the US at a latitude/longitude of $38.205°N$, $77.373°W$. To simulate the system perturbation and measurement noise, white Gaussian noise with different signal-noise-ratios (SNRs) is added to the ideal GICs and the synthetic measurements are obtained.

First, the substation grounding resistances are estimated assuming the E-field is known using Algorithm 7. Figure 7.3 illustrates the estimation error when the GIC measurements are subject to different levels of Gaussian noise. It is observed that the algorithm converges after two iterations

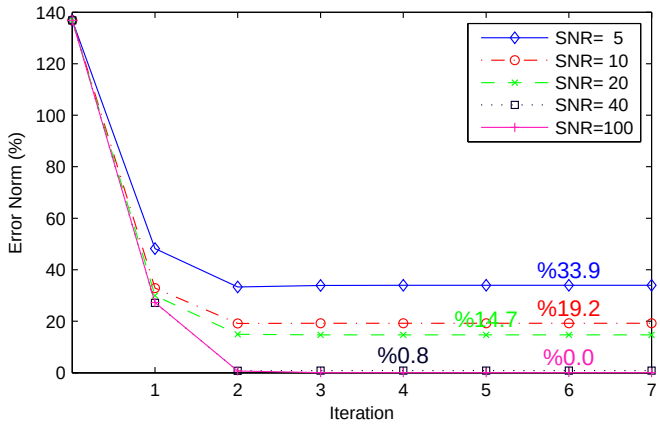


Figure 7.3: Estimation error for the test case when the E-field is known.

for all the noise levels. The final estimation error which is obtained after convergence depends on the noise level; i.e., higher noise level results in higher estimation error. For example, the estimation error is 33.9% when the SNR is 5 dB and zero when SNR is 100 dB (almost noise-free).

Sometimes, the E-field is not provided to the algorithm and only the GICs are available. In this case, the algorithm first estimates the E-field based on the GICs and then uses this estimation to find the resistances as presented in Algorithm 9. This technique is implemented for different measurement noise levels as illustrated in Fig. 7.4. The y-axis in the figure has a logarithmic scale. It is observed that the algorithm diverges when the SNR is 20 dB or lower (higher noise level). For the SNR equal to 30 dB, the algorithm converges, but the estimation accuracy is not much improved from the initial guess; 136.9% error in the initial guess is reduced only to 79.2% which is still too high. The estimation error drops significantly for lower noise levels with the estimation error equal to 8.7%, 0.5% and zero for SNRs equal to 40 dB, 50 dB and 100 dB, respectively. Comparing these results with those from Fig. 7.3, one can conclude that the algorithm is more robust to measurement noise when the E-field is available. Moreover, the algorithm has a faster convergence rate when the E-field is available as it converges in only two iterations with the E-field as opposed to three to four iterations without the E-field.

In practice, the GICs are not available at all the substations and only few substations have GIC sensors installed at their transformer neutrals. Hence, it is desired to evaluate the algorithm when

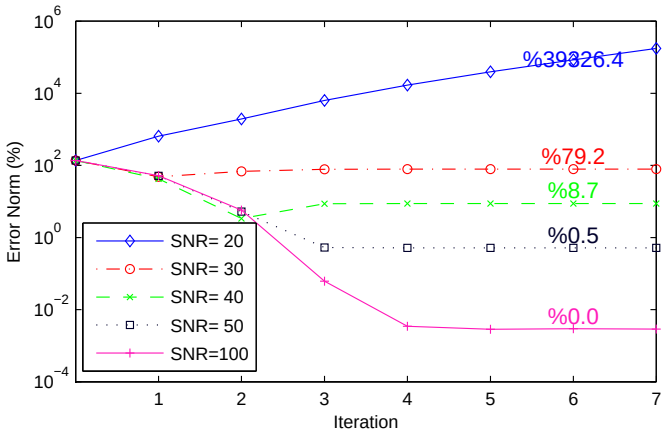


Figure 7.4: Estimation error for the test case when the E-field is unknown.

the GIC data is sparse. To model this, only the GICs at substations 1, 2, and 3 are provided to the algorithm and the rest are unknown. In this case, the algorithm reduces the GIC model to include only the substations with available data and ignores the rest of the network. Using the reduced model, the algorithm performs similarly to the normal case, but finds only the resistance of the substations included in the model. First, the substations are estimated assuming the E-field is known as illustrated in Fig. 7.5. For all noise levels, the error decreases after each iteration until it converges to around 10% at the third iteration. The interesting observation is that the algorithm is extremely robust to the measurement noise under this scenario and the curves for different noise levels are almost aligned. The other observation is that unlike the previous cases, the estimation error does not converge to zero when the measurements are noise free. This is because some of the substations have inaccurate grounding resistances and yet no GIC sensors which makes it impossible to track down the error they introduce to the estimation and makes the system unobservable. Simulation results indicate that the estimation error reduces to zero when the grounding resistances of the substations that are missing GIC sensors are accurate and the GIC measurements are noise free. The more substations with missing GIC sensors in the system and the more inaccurate their assumed grounding resistance, the higher the estimation error as verified through simulation.

It is important to realize that even though the algorithm may not provide 100% accuracy all the time, its estimation is remarkably better than the initial values. In other words, the algorithm

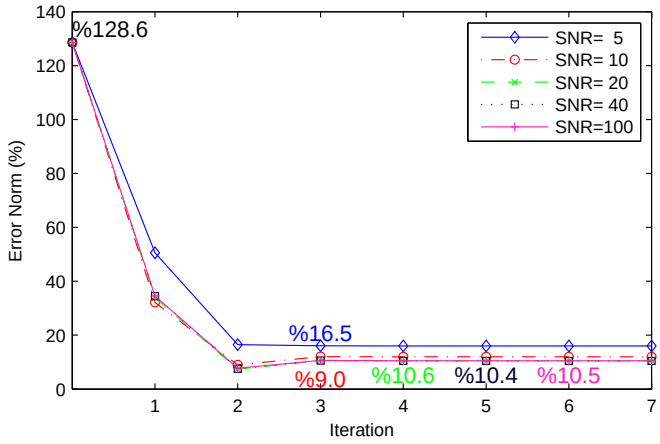


Figure 7.5: Estimation error for the test case when the E-field is known and the GIC data is sparse.

Table 7.2: Estimated Resistances for the Test Case When the GIC Data is Sparse

| Name | $R$ | $R_0$ | Initial Error (%) | $\hat{R}$ | Estimation Error (%) |
|---|---|---|---|---|---|
| SUB1 | 0.20 | 0.36 | 81.15 | 0.19 | 4.41 |
| SUB2 | 0.20 | 0.24 | 18.86 | 0.20 | 2.32 |
| SUB3 | 0.20 | 0.40 | 97.91 | 0.22 | 9.28 |

does not find the actual resistances, but it moves toward them and converges to somewhere in their close proximity. This is demonstrated in Table 7.2 by comparing the actual resistances with the estimated ones when the GIC measurements are noise free. For reference, the initial grounding resistances are presented as well.

The next validation test is to study the performance of the algorithm when the E-field is not available and the GIC data is sparse. The GICs at the first three substations (1, 2 and 3) are provided, but the E-field and the rest of GICs are missing. The algorithm excludes the substations with missing GICs from the model, estimates the E-field from the available GICs with one level of ambiguity and finally uses regularized least squares to find the resistances. Figure 7.6 illustrates the estimation error under this scenario for different measurement noise levels. The algorithm diverges when the SNR is 10 dB or lower. The algorithm converges for lower noise levels with the estimation error equal to 22.9%, 17.4% and 17.8% for SNRs equal to 10, 40 and 100, respectively.

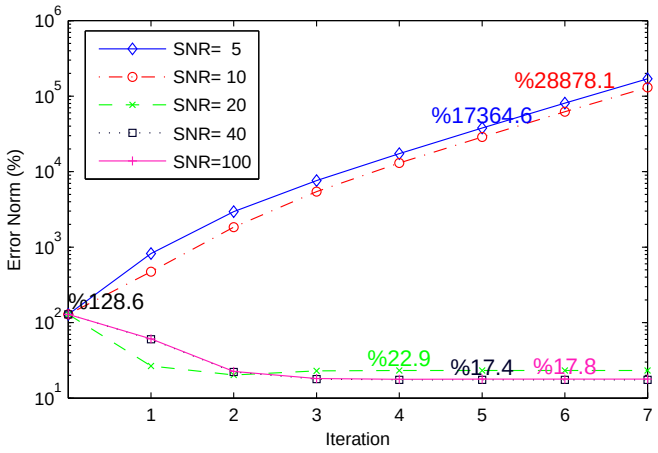


Figure 7.6: Estimation error for the test case when the E-field is unknown and the GIC data is sparse.

Similar to the case with the sparse GIC data and known E-field (Fig. 7.5), the estimation error does not reach zero when the GIC measurements are noise free. Again, this is due to the error in the grounding resistance of the substations that are missing GIC sensors and the lack of observability in these substations. If the actual grounding resistances of such substations are provided to the algorithm, the estimation error will reduce to zero in the absence of measurement noise.

Next, the effect of the assumed grounding resistances on the performance of the algorithm is studied. Four sets of assumed grounding resistances with varying levels of accuracy are considered and the algorithm is used to obtain the actual resistances as shown in Fig. 7.7. The accuracy level of the assumed resistances is denoted by $R_0$ SNR in the figure, and the noise level of the GIC measurements is 20 SNR for all the cases. The algorithm converges in fewer iterations when the assumed resistances are accurate, but the value it converges to is almost the same for all cases. This indicates that the estimation error is not sensitive to the accuracy of the assumed resistances; e.g., it is 9.3 % when the assumed resistance has 509% error and 5.9% when the assumed resistance error is 11.2%.

The accuracy in the assumed resistance of individual substations has varying impact on the performance of the algorithm. To demonstrate this, one substation is taken for testing at a time; its assumed grounding resistance is set to have 200% error while all other substations have accurate assumed resistances. The SNR of the GIC measurements is 20 dB for all the cases and the E-

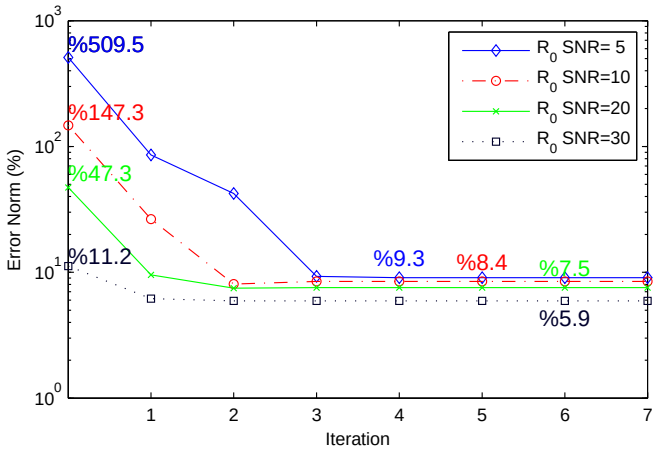


Figure 7.7: Estimation error when the assumed grounding resistances have different levels of accuracy.

field is assumed to be available to the algorithm. Figure 7.8 illustrates the estimation error when different substations have inaccurate assumed resistances. It is observed that the algorithm is most sensitive to the accuracy of the assumed resistances at Sub 3 and Sub 4.

Next, the impact of the noise level of individual GIC sensors on the performance of the algorithm is analyzed. Gaussian noise with SNR equal to 20 dB is added to all the GIC sensors except for the one being tested, which has higher noise level with SNR equal to 5 dB. The estimation error when different GIC sensors are subjected to a high level of noise is shown in Fig. 7.9. The assumed resistances of all the substations have 50% error and the E-field is known. The sensors at Sub 5, Sub 6 and Sub 7 are less robust to the measurement noise.

The error norm used so far for evaluating the estimation accuracy indicates the overall error of all the substations, but does not specify which substation contributes more to the total error. Figure 7.10 illustrates the estimation error of individual substations when the GIC measurements have different levels of noise. All the assumed grounding resistances have 50% error and the E-field is known. It is observed that the estimation error at Sub 7 is the largest and contributes the most to the total error. The estimated resistance of other substations is quite accurate under all noise scenarios. This could relate to the structure of the sensitivity matrices, $\mathbf{S}^N$ and $\mathbf{S}^E$, for this particular system. $\mathbf{S}^N$ and $\mathbf{S}^E$ both have very low values in their last column (row). This indicates that the GICs have low sensitivity to the grounding resistance of Sub 7. Hence, the GIC

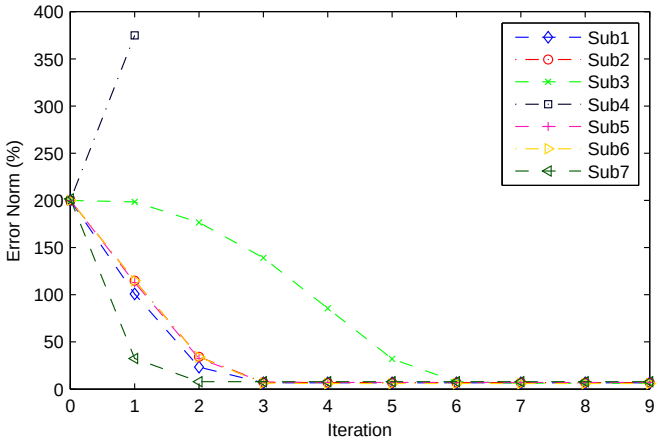


Figure 7.8: Estimation error when different substations have inaccurate assumed resistances.

measurements provide little observability to its resistance. The algorithm is generally not accurate in estimating the resistance of the substations with low sensitivities; however, it is still effective in improving the GIC calculation since such substations have low impact on the GICs regardless of their resistance values.

## 7.6 Application of the Algorithm to Larger Systems

The algorithm is applied to a 62,500 bus, 27,600 substation model of the Eastern Interconnection used in [37]. The goal is to estimate the grounding resistance of the EI substations that are more critical to the GMD analysis and whose values might be of greater interest to utilities. High voltage transformers are more susceptible to GMDs and the existing GIC sensors already installed by utilities are often at such transformers. Motivated by this, the list of high voltage transformers in the EI system is considered. This includes more than 200 transformers with a high-side voltage greater than 300 kV. Next, the top 100 transformers in the list which are most affected by GMDs are identified. This is done by calculating the GICs on the transformers under typical E-field profiles (northward and eastward field with unity magnitude) and selecting those with higher average GICs. A substation might have multiple transformers with high GICs in which case only one of the transformers is selected to avoid redundancy.

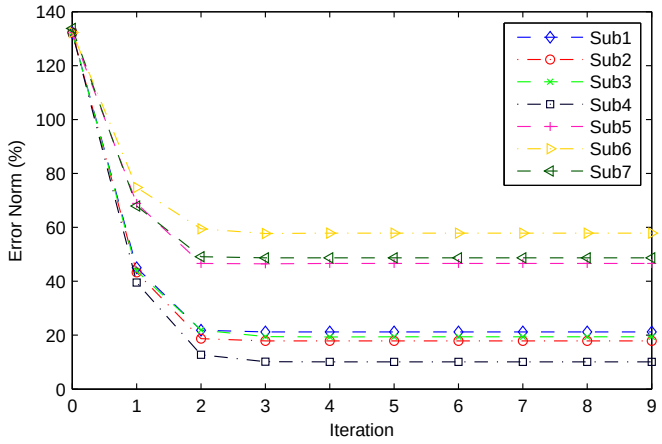


Figure 7.9: The estimation error when different GIC sensors are subject to high level of noise.

The same E-field data used for the 20-bus system is used here, i.e. the data for the March 9, 2012, storm measured at Fredericksburg observatory. This E-field is enforced to the system and the induced GICs are calculated. White Gaussian noise with 30 dB SNR is added to the ideal GICs and the synthetic measurements are obtained.

The assumed grounding resistances of the 100 investigated substations are generated by adding noise with SNR equal to 10 to the actual resistances. Figure 7.11 presents the actual and the assumed resistances (iteration 0); the former is to be estimated by the algorithm and the latter is provided as the initial guess. Starting with the assumed resistances, the algorithm moves towards the actual resistances as shown in the figure (iteration 1 and 2). The E-field is assumed to be unknown for this experiment. The estimation error over the first iterations is calculated and it is observed that the error reduces from 120% to zero in three iterations.

Note that the actual resistances used for the EI system are fictitious and do not reflect the actual values of the real system. As was mentioned before, the grounding resistances are seldom available and this is also the case for the EI system. The proposed algorithm can find the actual resistance of an EI substation if its GIC measurement ever becomes available. On another note, the line and transformer resistances, and the network topology, used in the study are obtained from the EI power flow model with good accuracy, and the grounding resistance is the only piece of information which is missing in the model.

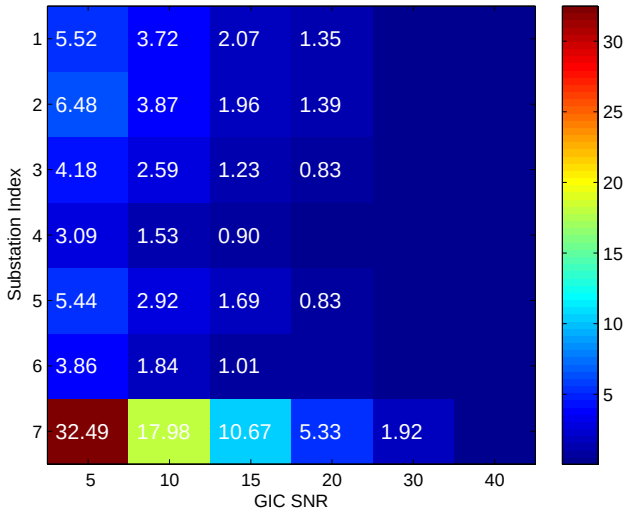


Figure 7.10: Estimation error of individual substations when the GIC measurements have different levels of noise.

## 7.7 Conclusion

In this chapter, an analytical technique is developed which derives the substation grounding resistances from the GIC measurements. In this technique, the relation between the GICs and the grounding resistances is linearized through some sensitivity parameters and linear regression is used to solve for the resistances. The uncertainty in the grounding resistances introduces error to the parameters of the linear model. To tackle this, the problem is reformulated to decouple the uncertainties from the known parameters and regularized least squares is used for solving it. The effectiveness of the algorithm is evaluated using both a small test case as well as a 62,500 bus model of the EI system. As demonstrated, the algorithm can estimate the grounding resistances accurately even when the available GIC measurements are sparse and the assumed resistances have large error.

The study suggests several directions for future research. First, the proposed algorithm should be applied to real GIC measurements as opposed to synthetic ones used here and its robustness to actual measurement noise and uncertainty needs to be validated. Second, the algorithm can be integrated into GIC model validation framework for improved performance. The grounding

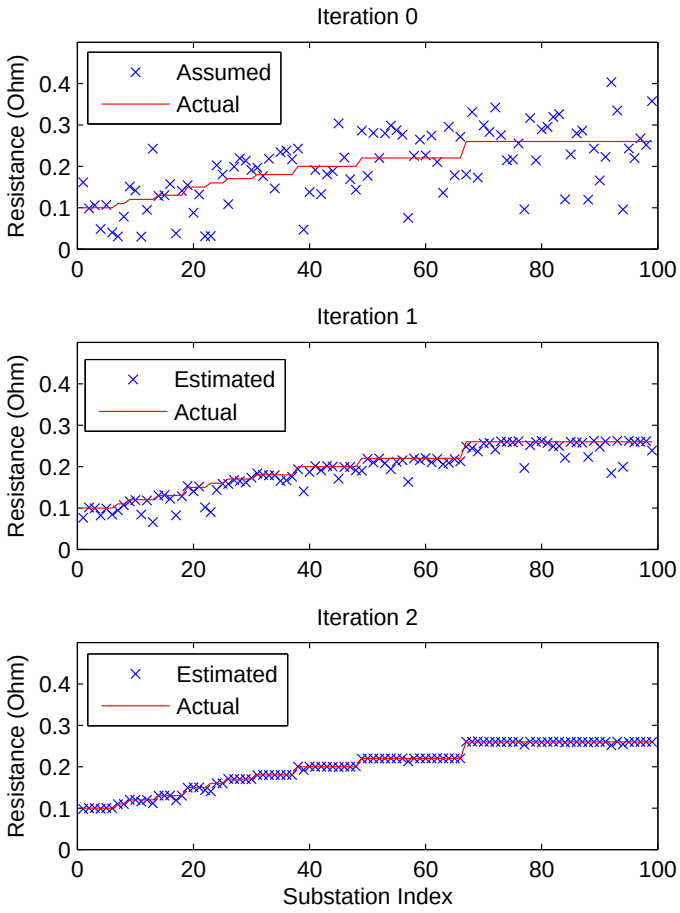


Figure 7.11: Assumed, estimated and actual grounding resistances of the substations in the EI systems.

resistance uncertainty has been a challenge in GIC model validation framework and future research will address this issue by utilizing the proposed algorithm.

# CHAPTER 8

# ENHANCED MAGNETIC FIELD ESTIMATION

## 8.1 Introduction

This chapter focuses on interpolating the magnetic field data to improve the GIC model validation. The available magnetic data is very sparse over the Earth's surface and readings of a distant magnetometer are often used for model validation. This chapter proposes an interpolation technique that considers the magnetic field inherent characteristics. The real magnetic data over a three-year period is analyzed and the dependencies between the observatories are extracted. These interdependencies are eventually incorporated in the interpolation and higher performance is achieved.

The techniques in [52, 53] utilize the physics of the Earth's magnetic field to improve the interpolation. This chapter approaches the problem differently. The historical magnetic data collected over time is extensively analyzed to capture interesting information which can eventually improve the interpolation. Correlation analysis is performed to extract the hidden dependencies between the magnetic fields of different observatories. Such dependencies are later utilized to improve the interpolation accuracy. Finally, the correlation analysis is extended to the frequency domain using dynamic wavelet transform.

This work is motivated by the research presented in Chapters 5 and 6 which looked at correlating the GICs on transformer neutral measurements in Wisconsin for the March 9, 2012, storm. The closest magnetometers to Wisconsin are FRD (Fredericksburg, VA) and OTT (Ottawa, ON), which are still more than 800 miles away. The results of this work tend to facilitate such GIC validation framework by providing the interpolated magnetic field across the Wisconsin area.

The chapter is organized as follows: The dataset used for this study is described in Section 8.2. The correlation analysis is the subject of Section 8.3, which explores the possible interdependencies between the observatories. The proposed interpolation technique incorporating the

dependencies is presented in Section 8.4, while real data analysis is used in Section 8.5 to evaluate its performance. In Section 8.6, the correlation analysis is extended to frequency domain using wavelet transform. Section 8.7 presents a conclusion and directions for future work.

## 8.2 The investigated Magnetic Data

This study uses the 1-minute ground magnetometer data for a three-year test period from January 1, 2011 to December 30, 2014. The data is collected from 21 observatories in North America with the geographic locations illustrated in Fig. 3.2. USGS provides this data in a daily format in [81]. The test data includes 1095 datasets where each dataset has the daily data of all the observatories.

The magnetic data is in three directions – north, east and vertical. The field variation in the vertical direction does not impact the power system significantly. Hence, only the north and east directions are considered for this study. The data analysis and interpolation techniques can be performed in each direction separately and independently. To be concise, the analysis is performed only in the north direction throughout the chapter and readers can extend it to the east direction using the same procedure.

The raw data is preprocessed before performing any analysis. First, the missing data is identified and effectively removed from the raw data. Second, the median filter is used to remove the spikes and unwanted transients. Last, the representation of the magnetic data is transformed from polar to Cartesian coordinates and the fields in the north and east directions are obtained.

## 8.3 Correlation Analysis

The correlation between the magnetic fields of different observatories may reveal interesting information about the evolution of the magnetic field over the Earth's surface during a storm. In this section, correlation analysis is performed on the three-year data and various visualization tools are developed to understand the pairwise correlations between the observatories.

The average dependency between two observatories is obtained by first calculating the correlation coefficient between their magnetic data during each day and then taking the average over all

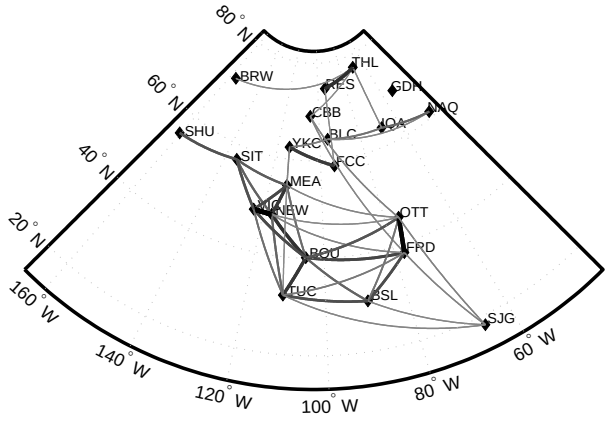


Figure 8.1: Dependencies between the observatories based on their magnetic field.

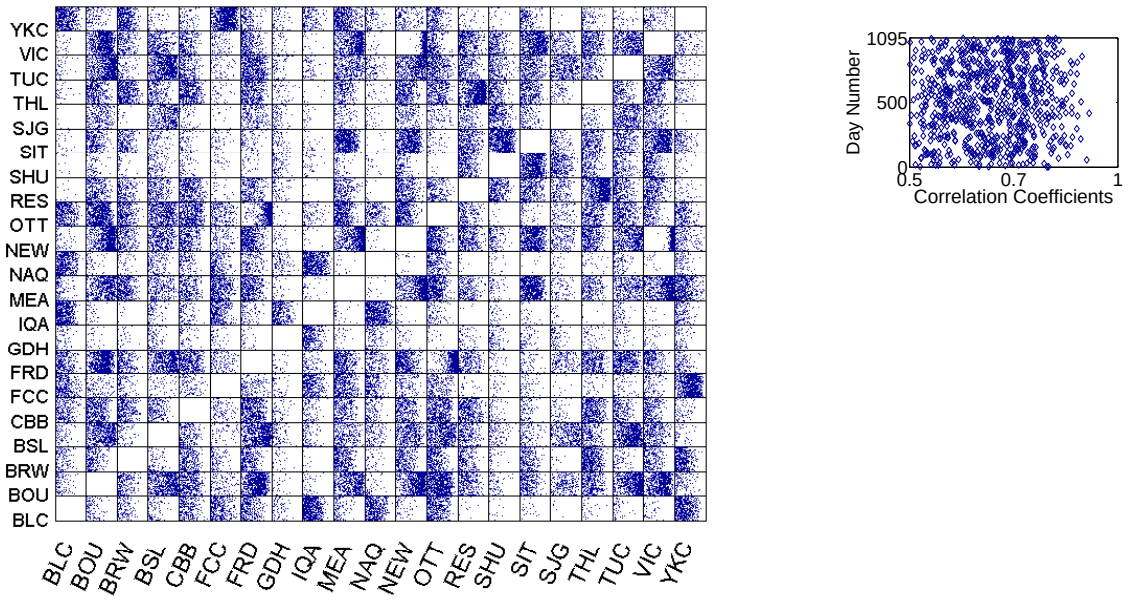


Figure 8.2: Variation of the correlation coefficients over the test days.

the 1095 days in the test period. Pearson coefficient is used as the dependency measure.

Figure 8.1 presents a visualization of the dependencies between different observatories. There is

a line connecting two observatories if their average correlation coefficient is greater than 0.5. The thickness and color of the connecting line relates to the coefficient value where higher coefficients have thicker lines with darker shades of grey.

The variation of the correlation coefficients over the test days is visualized in Fig. 8.2. Each block corresponds to one pair of observatories with the observatory codes shown in the vertical and horizontal axes. Here, only the coefficients more than 0.5 are visualized. For each block, the horizontal axis is used to visualize the coefficient value ranging from 0.5 to 1. The vertical axis denotes the day number in the study period (ranging from 1 to 1095). As an example, the block corresponding to the pair of MEA (Meanook, AB) and SIT (Sitka, AK) observatories is magnified in the figure.

It is observed that some blocks contain a large number of points while others are sparsely covered. A block is densely covered when its corresponding observatories are highly dependent and their coefficients are greater than 0.5 on most of the days. Such observatory pairs are referred to as dependent observatories. The other interesting observation is that at some blocks, the points are concentrated around one line, while at others they are scattered all over the area. An example of the former is the block for the FRD and OTT pair, while the MEA-SIT block follows the latter. Probability distribution may be used to better demonstrate this aspect. The probability distribution of the coefficients between FRD and OTT is illustrated in Fig. 8.3. For this pair, the coefficients have a small standard deviation with a peak at around 0.95. This indicates that for an unseen data, one can tell the value of the coefficient between FRD and OTT with high confidence.

The probability distribution for the SIT and MEA pair is illustrated in Fig. 8.4. Unlike the previous pair, this one exhibits a wide range of variation in its coefficients. Hence, for an unseen datum, one can tell these observatories are dependent with high confidence. However, the value of their coefficient remains unknown.

The probabilistic visualization of the dependent observatories is presented in Fig. 8.5. Each colored block corresponds to one pair of observatories with the observatory codes shown in the vertical and horizontal axes. The number in each block indicates the probability that the corresponding observatories are dependent. This probability is obtained by counting the number of days when the correlation coefficient is greater than 0.5 and dividing it by the total number of days (1095 for this study). The probabilities are expressed in percentage and the block colors correlate

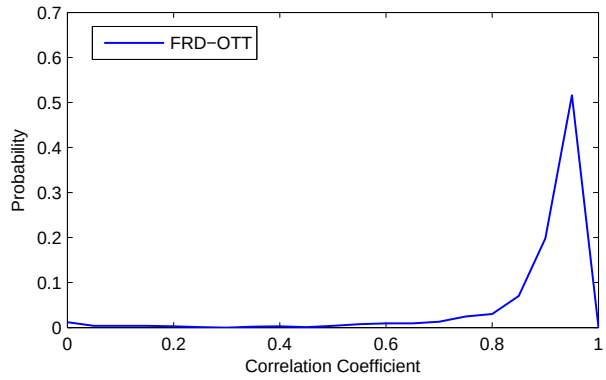


Figure 8.3: Probability distribution of the correlation coefficients (FRD-OTT pair).

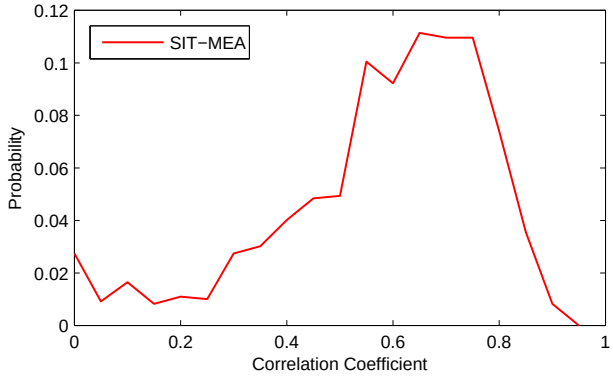


Figure 8.4: Probability distribution of the correlation coefficients (SIT-MEA pair).

with their values. Probabilities less than 40% are not visualized in this figure.

## 8.4 MultiVariant Interpolation

Given the known points $y_i = y(x_i)$ for $i = 1, \cdots, N$, inverse distance weighting (IDW) may be used to obtain the interpolated value $y$ at a given point $x$ as expressed in:

$$y(x) = \frac{\sum_{i=1}^{N} \omega_i(x) y_i}{\sum_{i=1}^{N} \omega_i(x)} \tag{8.1}$$

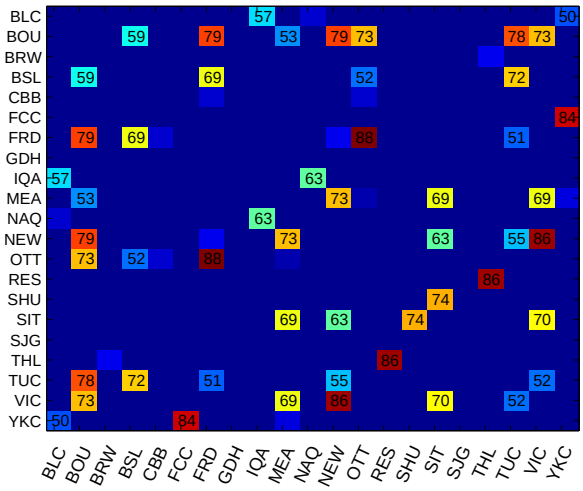


Figure 8.5: Probabilistic visualization of the dependent observatories.

where $\omega_i$ is the weighting function and defines the influence of known points on the interpolated point. A simple IDW weighting function is given by

$$\omega_i(x) = \frac{1}{d(x, x_i)^p} \tag{8.2}$$

where $d(x, x_i)$ is the distance between point $x_i$ and $x$, and $p$ is the power parameter. The larger the power parameter, greater the influence given to the points closer to the interpolated point. Such a weighting function is based on the assumption that closer points have more similar values. Sometimes, factors other than distance might determine the similarity between points and it is desired to incorporate such factors in the weighting function as well.

The similarity of the observatories in their magnetic field is not solely dependent on their distances, as demonstrated in Fig. 8.1. For example, SIT has good correlation with MEA, VIC (Victoria, BC) and NEW (Newport, RI), but has no similarity with YKC (Yellowknife, NT) which is equally close. It is desired to extract such similarity structures within the observatories from the historical data and include them in the weighting function. A possible weighting function which

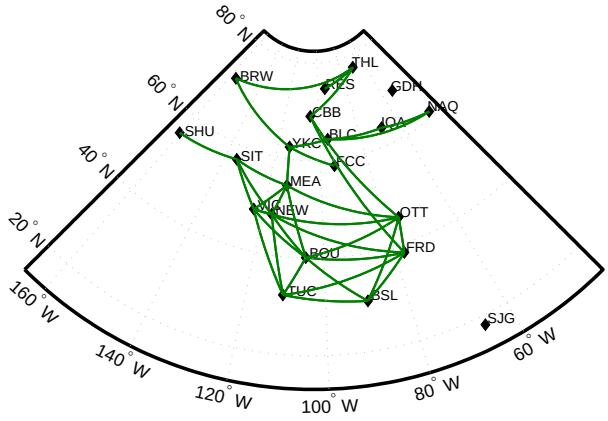


Figure 8.6: A visualization of the similarity parameters.

incorporates the similarity structures is given by:

$$\omega_i(x) = \frac{c(x, x_i)}{d(x, x_i)} \tag{8.3}$$

where $c(x, x_i)$ is a binary variable called similarity parameter that specifies the similarity between points $x$ and $x_i$ as expressed in

$$c(x, x_i) := \begin{cases} 1, & x \text{ and } x_i \text{ are similar} \\ 0, & \text{otherwise} \end{cases} \tag{8.4}$$

The similarity parameters are obtained from the three-year data and based on the dependency probabilities presented in Fig. 8.5. The similarity parameter between two observatories is one when their dependency probability is more than 50% and zero otherwise. A visualization of these parameters is presented in Fig. 8.6. There is a line connecting two observatories when their similarity parameter is one.

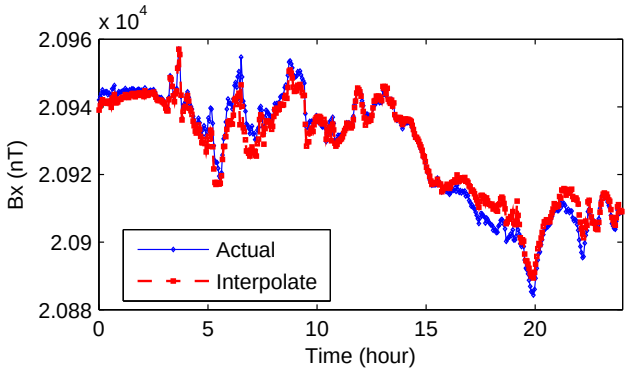


Figure 8.7: Comparison of the interpolated and actual field at FRD for a quiet day, March 1, 2012.

## 8.5 Real Data Studies

In this section, the performance of the proposed interpolation is evaluated. Assuming $N$ observatories with known magnetic field, one observatory is selected for testing and the fields at the $N-1$ remaining observatories are used to interpolate its value. Comparing the interpolated field with the actual one yields the accuracy. This procedure is referred to as the N-1 accuracy test.

The accuracy in interpolating the magnetic field at FRD is demonstrated in Fig. 8.7. The magnetic field from March 1, 2012, is used for this testing. The fields at the remaining observatories are used to interpolate the FRD value. The similarity parameters obtained from the three-year test period are incorporated in the interpolation to achieve higher accuracy. Clearly, the interpolated field agrees well with the actual one.

The accuracy in interpolating FRD field during a stormy day is illustrated in Fig. 8.8. The magnetic field from the March 9, 2012, storm is used for this testing. It is observed that the accuracy is lower for the stormy day than the quiet day. Note that this observation is specific to this study and may not be generally true. For example, the interpolation accuracy for FCC (Fort Churchill, MB) during the same storm is demonstrated in Fig. 8.9. For this observatory, the interpolation has extremely high accuracy even during the storm. To understand how the interpolation performance relates to the level of the geomagnetic activity, more thorough analysis is required which is left for future work.

Next, the N-1 accuracy test is performed on all the observatories and for all the days in the

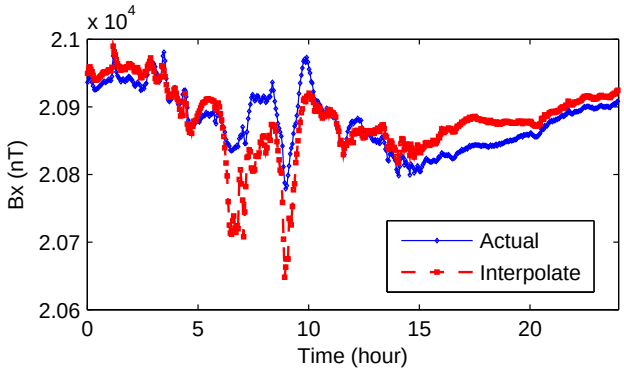


Figure 8.8: Comparison of the interpolated and actual field at FRD for the March 9, 2012 storm.

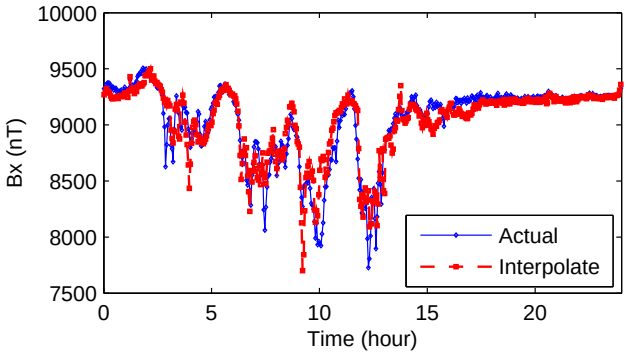


Figure 8.9: Comparison of the interpolated and actual field at FCC for the March $9^{th}$, 2012 storm.

test period. For each test, one observatory and one day is selected. The field at the selected observatory during the selected day is interpolated using the fields at the remaining observatories. The agreement between the interpolated and the actual field is quantified by:

$$Error(\%) = 100 \times \frac{\|\hat{Y} - Y\|_2}{\|Y\|_2} \tag{8.5}$$

where $Y$ and $\hat{Y}$ are the vectors of the actual and interpolated magnetic fields, respectively, and $\|\cdot\|_2$ denotes the Euclidean norm. Using this error definition, the average interpolation error is visualized in Fig. 8.10. For each observatory, first the interpolation error is obtained for all the 1095 days in the test period and then their average is calculated. For reference, the dependencies between the observatories are also illustrated using the visualization in Fig. 8.1. The interesting observation

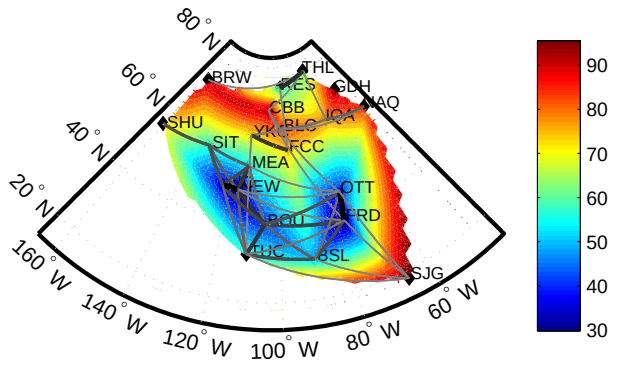


Figure 8.10: Average interpolation error at different observatories.

is that the interpolation error is lower at the observatories which have higher dependencies with others. For example, MEA, NEW, BOU and BUC are highly interdependent as demonstrated by the thick, dark lines connecting them. They also have lower interpolation error as shown with the blue area in the figure.

Integrating the similarity parameters into the interpolation improves the accuracy. Figure 8.11 presents the average interpolation error when no prior information about the similarities is available. The weighting function in (8.2) is used for this study which is solely dependent on the distances. Note that the color bar in the figure ranges from 82% to 94%. This error reduces to 30% when the similarity parameters are included, as shown in Fig. 8.10. It is important to mention that the error definition used here results in relatively high values even for accurate interpolations and is only suitable for comparison purposes. For example, the interpolations presented in Fig. 8.7 and Fig. 8.8 have errors of 19.4% and 89.4%, respectively.

## 8.6 Wavelet Analysis

Wavelet transform decomposes a signal into different frequency bandwidths while maintaining the temporal structure of the signal. Unlike Fourier transform that is only localized in frequency, wavelets are localized in both time and frequency. Wavelets provide a combination of time and frequency spectrum, but the frequency spectrum is not as detailed as that obtained from the Fourier

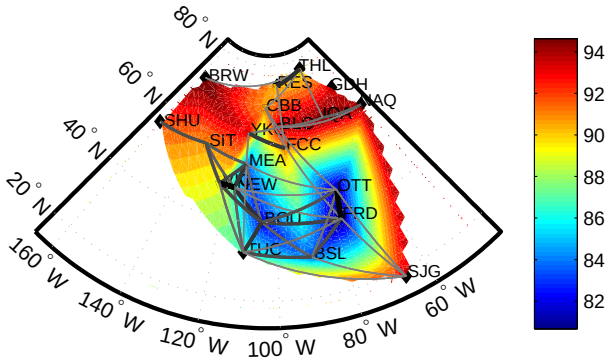


Figure 8.11: Average interpolation error when the similarity parameters are not integrated.

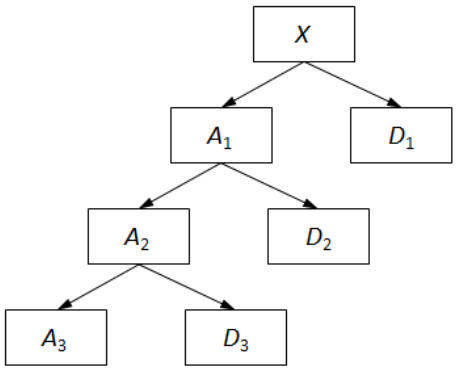


Figure 8.12: Three-level wavelet decomposition.

transform.

The signal is decomposed into two frequency bandwidths, namely approximation and detail. The approximation signal contains the lower half of the frequencies while the detail includes the high half. This process could be repeated on the approximation signal to achieve higher orders of wavelet decomposition. A diagram of the three-level decomposition is presented in Fig. 8.12. In the figure, $D_i$ and $A_i$ are, respectively, the detail and approximation signals at level $i$, and $X$ is the input signal. The detail signal at each level provides a temporal representation of the input signal within a certain frequency bandwidth. The frequency bandwidth associated with each level for a three-level decomposition is illustrated in Fig. 8.13.

Wavelet analysis is applied to the magnetic field data to understand the interdependencies be-

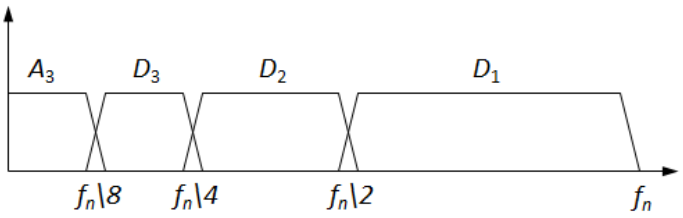


Figure 8.13: Frequency bandwidths of different components in a three-level wavelet decomposition.

Table 8.1: The Frequency Bands of the Detail Signals Using 1-second Magnetic Data

| Wavelet Detail | Frequency (MHz) |
|---|---|
| $D_1$ | 500-1000 |
| $D_2$ | 250-500 |
| $D_3$ | 125-250 |
| $D_4$ | 62.5-125 |

tween the observatories with respect to their frequency spectrum [51]. In this analysis, 1-second magnetic data is used instead of the 1-minute data to cover a wider frequency range. Wavelet decomposition is performed on the data up to 15 levels. The detail signal at each level is used as a temporal representation of its corresponding frequency band. The bands covered by $D_1$ to $D_4$ are presented in Table 8.1.

Next, the correlation analysis is performed on different frequency bands. The correlation coefficients are calculated between the detail signals of the same level, but different observatories. The coefficients between three sets of observatory pairs at different frequency bands are plotted in Fig. 8.14. The magnetic field from the March 9, 2012, storm is used for this testing. The interesting observation is that the coefficients are higher at the lower frequencies bands. This implies that the low frequency components of the magnetic field have higher correlation with their counterparts at the other observatories.

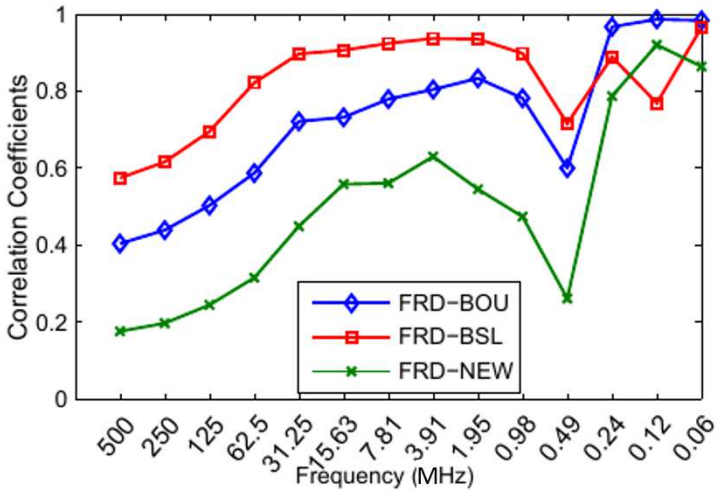


Figure 8.14: Correlation coefficient at different frequency bands.

## 8.7 Conclusion

In this chapter, the magnetic field measurements at 21 observatories in North America over a three-year period are extensively studied and various statistical measures are extracted from the data. Correlation analysis is performed to capture the possible dependencies between the observatories. It is observed that the magnetic fields at some observatories are highly correlated and this dependency is not always related to their distance. To address this, the inverse distance weighting interpolation is modified to account for such dependencies. The modified interpolation improves over the conventional one as demonstrated through real data analysis. Finally, the correlation analysis is extended to the frequency domain using the wavelet transform. The interpolation technique developed in this chapter can provide a more accurate magnetic field input for the GMD model validation frameworks presented in Chapter 5 and Chapter 6. This improves their validation capability and makes them stronger tools for enhancing power system resiliency.

# CHAPTER 9

# ENHANCED E-FIELD ESTIMATION THROUGH DYNAMIC MODELING AND FILTERING

## 9.1 Introduction

This chapter presents dynamic modeling of the electric field as an effective technique to improve the E-field estimation. Actual magnetic field measurements during several GMD events are used to develop a practical dynamic model for the electric field. The developed dynamic model is integrated into a Kalman filter and higher accuracy in E-field estimation is achieved. The overall performance of the proposed estimation technique over the conventional LS estimation is demonstrated through simulation.

The improved E-field estimation developed in this chapter can facilitate the GMD model validation frameworks in Chapters 5 and 6. GIC measurements are often subject to different types of noise, and using Kalman filtering instead of the investigated LS estimator makes these validation techniques more robust to such measurement uncertainties.

The rest of the chapter is organized as follows: The dynamic modeling for E-field is introduced in Section 9.2. Section 9.3 presents Kalman filtering and its application in E-field estimation. In Section 9.4, real E-field data is used to analyze the dynamics of the E-field and derive its dynamic model. A comparison between the Kalman filter approach and the LS estimator is performed in Section 9.5, while Section 9.6 presents a conclusion and directions for future work.

## 9.2 Dynamic Modeling of Electric Field

Analyzing the variation of the E-field with time, one can recognize the correlation of the data with its previous values. This phenomenon is verified by calculating the autocorrelation of the E-field as illustrated in Fig. 9.1. The geomagnetic data at Fredericksburg observatory during the day of

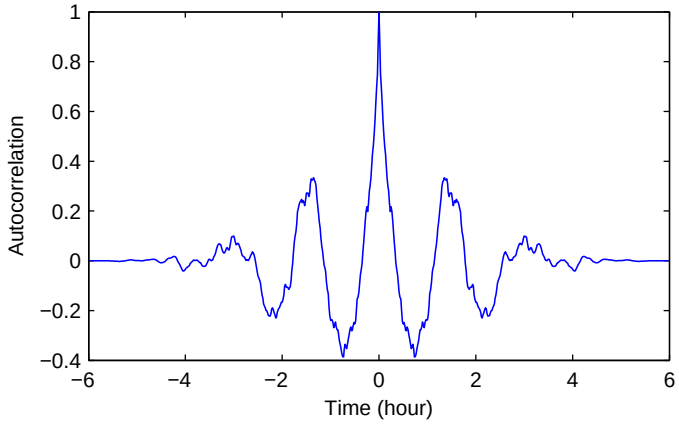


Figure 9.1: Autocorrelation of the E-field in the north direction for the day of August 5, 2011.

August 5, 2011, is used for obtaining this data [81]. The area below the autocorrelation curve represents the dependency of the signal on its previous values.

The evolution of the E-field over time is described by its dynamic model. The autocorrelation observed in the data suggests application of autoregressive (AR) models for describing the dynamics of the system. The first order AR model is defined as

$$X_{k+1} = \mathbf{A}X_k + W_k \tag{9.1}$$

where $\mathbf{A}$ is the state transition model and $w$ is the process noise. This model indicates that the state is linearly dependent on its value at the previous time step.

### 9.2.1 Parameter Estimation

This section presents a method for estimating the parameters of the dynamic model. The dynamic model for E-field is given by

$$\begin{bmatrix} x_{k+1}^N \\ x_{k+1}^E \end{bmatrix} = \begin{bmatrix} a_{11} & a_{12} \\ a_{21} & a_{22} \end{bmatrix} \times \begin{bmatrix} x_k^N \\ x_k^E \end{bmatrix} + \begin{bmatrix} w_k^N \\ w_k^E \end{bmatrix} \tag{9.2}$$

where $w^N = \mathcal{N}(0, \sigma_N^2)$ and $w^E = \mathcal{N}(0, \sigma_E^2)$. For this model, the state transition model is a $2 \times 2$ matrix which has four unknown parameters. The process noise is a 2-dimensional random vector with normal distribution and the variance of each dimension should be estimated. To estimate these six unknown parameters, the problem is formulated as a linear regression problem and the LS estimation is used for solving it.

The data for $N$ consecutive time steps are used to estimate the parameters of the dynamic model. Writing the dynamic model at all the time steps gives rise to $n-1$ equations. These $n-1$ equations are stacked together and written in vector form as

$$
\begin{aligned}
\bar{\mathbf{X}} =& \mathbf{M} \times \bar{A} + \bar{\mathbf{W}} \\
\bar{\mathbf{X}} =& \begin{bmatrix} x_2^N, x_3^N, \cdots, x_n^N, x_2^E, x_3^E, \cdots, x_n^E \end{bmatrix}^T \\
\bar{\mathbf{W}} =& \begin{bmatrix} w_1^N, w_2^N, \cdots, w_{n-1}^N, w_1^E, w_2^E, \cdots, w_{n-1}^E \end{bmatrix}^T \\
\bar{A} =& \begin{bmatrix} a_{11}, a_{12}, a_{21}, a_{22} \end{bmatrix}^T \\
\mathbf{M} =& \begin{bmatrix}
x_1^N & x_1^E & 0 & 0 \\
x_2^N & x_2^E & \vdots & \vdots \\
\vdots & \vdots & 0 & 0 \\
x_{n-1}^N & x_{n-1}^E & & \\
 & & x_1^N & x_1^E \\
0 & 0 & x_2^N & x_2^E \\
\vdots & \vdots & \vdots & \vdots \\
0 & 0 & x_{n-1}^N & x_{n-1}^E
\end{bmatrix}
\end{aligned}
\tag{9.3}
$$

The LS estimation is used to solve the overdetermined system of equations presented in (9.3). The parameters of the state transition model are calculated by

$$
\bar{A} = (\mathbf{M}^T \mathbf{M})^{-1} \mathbf{M}^T \bar{\mathbf{X}} \tag{9.4}
$$

and the variance vector of the process noise is given by

$$\bar{\mathbf{W}} = \begin{bmatrix} \hat{W}^N \\ \hat{W}^E \end{bmatrix} = \bar{\mathbf{X}} - \bar{A}\mathbf{M} \Rightarrow \begin{cases} \sigma_N = \text{Var}\left( \hat{W}^N \right) \\ \sigma_E = \text{Var}\left( \hat{W}^E \right) \end{cases} \tag{9.5}$$

### 9.2.2 Simplified Dynamic Model

The dynamic model presented in (9.1) assumes a coupling between the northward and eastward fields. This allows values in one direction to be dependent on the previous values in other directions. One can simplify the dynamic model by ignoring this coupling. The simplified model is given by

$$\begin{cases} x_{k+1}^N = a_N x_k^N + w_k^N \\ x_{k+1}^E = a_E x_k^E + w_k^E \end{cases} \tag{9.6}$$

where $a_N$ and $a_E$ are the transition models for the northward and eastward E-fields respectively. The method for estimating these two parameters is similar to the one presented in the previous section.

## 9.3 E-field Estimation Using Kalman Filter

A stochastic linear time-invariant (LTI) system consists of the dynamic model and the observer model as presented in (9.7). The dynamic model describes the evolution of the state with time and is in the form of an ordinary differential equation. The observer model relates the observations to the states through a linear model. In equation (9.7), $W_k$ and $V_k$ are independent Gaussian random vectors and they represent the state noise and the observation noise respectively.

$$\begin{cases} X_{k+1} = \mathbf{A}X_k + W_k \\ Z_k = \mathbf{H}X_k + V_k \end{cases} \tag{9.7}$$

To solve the stochastic LTI system, the classical Kaman filter is used. The Kalman filter is a

recursive estimator which estimates the state at the current step based on the state estimated at the previous step and the current observations. The estimation process is usually presented in two steps: the prediction step and the correction step. In the prediction step, the estimated state at the previous step is used to make a prior estimate of the state at the current step as given by

$$\hat{X}_k^- = \mathbf{A}\hat{X}_{k-1}^+ \tag{9.8}$$

where $\hat{X}_k^-$ is the priori estimate at the $k^{th}$ time step and $\hat{X}_{k-1}^+$ is the posteriori estimate or the final estimate at the $k-1^{th}$ time step. The prediction step also involves estimating the error covariance at the current step based on the error covariance at the previous step as described in (9.9). In this equation, $\mathbf{Q}$ is the covariance of the noise for the state model.

$$\mathbf{P}_k^- = \mathbf{A}\mathbf{P}_{k-1}^+\mathbf{A}^T + \mathbf{Q} \tag{9.9}$$

In the correction step, the prior estimate of the state is corrected by utilizing the observation at the current step as given by

$$\hat{X}_k^+ = \hat{X}_k^- + \mathbf{K}_k(X_k - \mathbf{H}\hat{X}_k^-) \tag{9.10}$$

where $\mathbf{K}_k$ is the Kalman gain at the $k$-th step and is calculated by (9.11). The Kalman gain is the optimal weighting for the innovation $Z_k - \mathbf{H}X_k$ and minimizes the error.

$$\mathbf{K}_k = \mathbf{P}_k^-\mathbf{H}^T(\mathbf{H}\mathbf{P}_k^-\mathbf{H}^T + \mathbf{R})^{-1} \tag{9.11}$$

Finally, the error covariance is updated at the end of the correction step as given by

$$\mathbf{P}_k^+ = (\mathbf{I} - \mathbf{K}_k\mathbf{H})\mathbf{P}_k^- \tag{9.12}$$

The prediction step and the correction step are executed recursively until the states at all the time steps are estimated. To initialize the recursions, the estimated state and its error covariance at the

first time step are initialized by

$$\begin{cases} \hat{X}_0 = \mathbf{E}[X_0] \\ \mathbf{P}_0 = \mathbf{E}[(X_0 - \mu)(X_0 - \mu)^T] \end{cases} \tag{9.13}$$

If the initial state is known, $\hat{X}_0 = X_0$ and $\mathbf{P}_0 = 0$ are used instead for the initialization.

## 9.4 E-field Dynamic Modeling Using Real Data

In this section, actual magnetic field measurements are used to study the dynamic behavior of the E-field during geomagnetic storms. During the day of August $5$, $2011$, a geomagnetic storm started at 18:00 UTC and reached a very high level in the following hours. The magnetic field measured at Fredericksburg observatory during this storm is used to obtain the E-field as illustrated in Fig. 9.2. Note that the variation of E-field is very small during the normal hours, but large peaks are observed during the storm. A dynamic model is developed for the data during the storm. The parameters of this model are calculated by eqs. (9.3) to (9.5). These parameters are $a_{11} = 0.923$, $a_{12} = 0.621$, $a_{21} = 0.009$, $a_{22} = 0.866$, $\sigma_N = 11.24$, and $\sigma_E = 2.55$. Note that $\sigma_E$ is remarkably smaller than $\sigma_N$, which indicates that the autocorrelation of electric field in the east direction is more significant.

The dynamic model can be simplified by ignoring the coupling between the northward and eastward E-fields as proposed by (9.6). The parameters of the simplified model are $a_N = 0.923$, $a_E = 0.866$, $\sigma_N = 11.24$, and $\sigma_E = 2.55$. Interestingly, the noise level of the simplified model is equal to the original model. This indicates that the simplified model is as accurate as the original model and ignoring the coupling between the two fields introduces no error to the model. In other words, the coupling is insignificant and can be ignored for simplification purposes. Hence, the simplified dynamic model will be used for the ensuing numerical analysis.

It is important to understand how the parameters of the dynamic model change over different storms. The E-field data for three different geomagnetic storms and three normal days are analyzed and the parameters of their dynamic models are calculated as presented in Table 9.1. An interesting observation is that the noise level for stormy days is higher than for normal days. This implies that

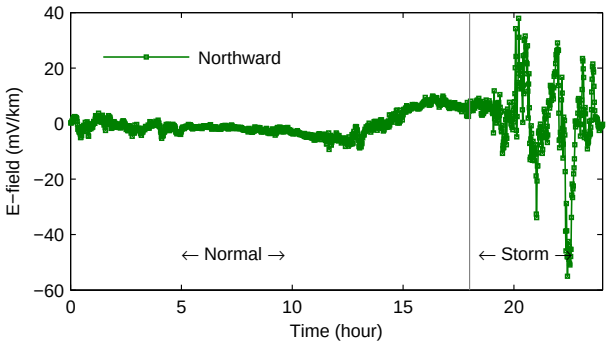


(a)

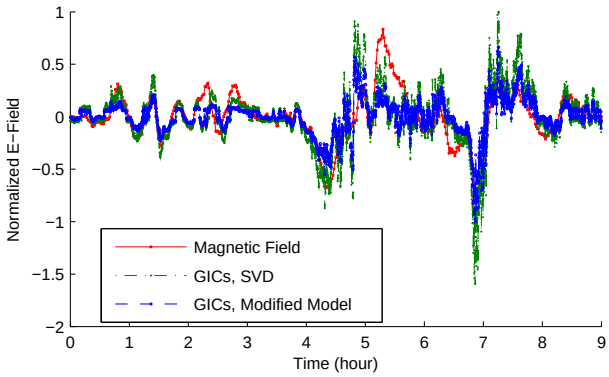


(b)

Figure 9.2: E-field in (a) north direction and (b) east direction.

the dynamic model has lower accuracy in modeling the E-field of a stormy day compared to a normal day.

Note that the values of $a_N$ and $a_E$ range only from $0.80$ to $0.93$ for both stormy days and normal days. This suggests that these parameters are not highly dependent on the individual E-field measurements and could be approximated as constants over different sets of data. According to Table 9.1, the average of $a_N$ over the six datasets is $0.88$ and the average of $a_E$ is also $0.88$. These two values can be used as the approximation of the dynamic model parameters for any given E-field data. The advantage of this approximation is that one can develop the dynamic model for unknown datasets.

Table 9.1: Parameters of the E-field Dynamic Model for Different Geomagnetic Events

| | $a_N$ | $a_E$ | $\sigma_N$ | $\sigma_E$ |
|---|---|---|---|---|
| Storm 1 | 0.92 | 0.86 | 11.24 | 2.55 |
| Storm 2 | 0.88 | 0.90 | 29.61 | 1.45 |
| Storm 3 | 0.80 | 0.86 | 17.58 | 2.24 |
| Normal 1 | 0.86 | 0.85 | 2.03 | 0.17 |
| Normal 2 | 0.93 | 0.91 | 1.37 | 0.09 |
| Normal 3 | 0.90 | 0.90 | 2.80 | 0.28 |

The general E-field dynamic model derived from actual data is given by

$$\begin{cases} x_{k+1}^N = 0.88 x_k^N + w_k^N \\ x_{k+1}^E = 0.88 x_k^E + w_k^E \end{cases} \tag{9.14}$$

where $w^N = \mathcal{N}(0, \sigma_N^2)$ and $w^E = \mathcal{N}(0, \sigma_E^2)$. Note that $\sigma_N$ and $\sigma_E$ depend on the individual E-field datasets and are not provided by this model. Fortunately, these parameters do not affect the results of the Kalman filter significantly. Hence, random values could be selected for these parameters.

The dynamic model presented in (9.1) is an autoregressive model of order one. However, higher order AR models can be used to describe the dynamics of the E-field. In general, the AR model of order $p$ is defined as

$$X_k = \sum_{i=1}^{p} A_i X_{k-i} + W_k \tag{9.15}$$

Table 9.2 presents the AR models of E-field with orders from one to five. The northward E-field for the August 5, 2011, storm is used to derive the parameters of these models. An interesting observation is that increasing the order of the model does not affect the noise level. This indicates that the E-field at one time step depends on the E-field at the last step, but not the earlier ones. Hence the first order AR model provides sufficient accuracy and using higher order models is not necessary.

Table 9.2: Parameters of the AR Models with Different Orders

| Order | Transition Model | Noise |
|---|---|---|
| 1 | $a_1$ =0.92, | $\sigma$ =11.2 |
| 2 | $a_1$ =1.02, $a_2$ =-0.10 | $\sigma$ =11.2 |
| 3 | $a_1$ =1.04, $a_2$ =-0.32, $a_3$ =0.21 | $\sigma$ =11.2 |
| 4 | $a_1$ =1.05, $a_2$ = -0.33, $a_3$ =0.26, $a_4$ =-0.04, | $\sigma$ =11.2 |
| 5 | $a_1$ = 1.05, $a_2$ =-.35, $a_3$ =.27, $a_4$ =-.09, $a_4$ =.04 | $\sigma$ =11.2 |

## 9.5 Numerical Results and Simulations

In this section, the performance of the LS estimator is compared with the Kalman filter based on the simulation results. The effect of sensor failure rate, outlier rate and Gaussian noise level on the performance of the two estimators is studied and accuracy comparison is conducted accordingly. For this study, the 20-bus system in [38] is investigated.

To analyze the performance of the estimators, the E-field presented in Fig. 9.2 is enforced to the system. The GICs induced by this E-field are determined via solving the GIC flow program in PowerWorld Simulator. The GIC model in (3.14) can also be used for calculating transformer GICs. The results obtained from this model are identical to those provided by the GIC flow program.

The GICs obtained from the GIC flow program represent ideal measurements. The noisy measurements are obtained by adding white Gaussian or nonuniform noise to the ideal GIC values. The Monte Carlo simulation with $1000$ realizations is used to simulate the randomness in the additive noise.

The effect of the Gaussian noise level on the performance of the estimators is illustrated in Fig. 9.3. In this calculation, the outlier rate and failure rate are set to zero. According to this figure, the Kalman filter outperforms the LS method at higher noise levels and falls below the LS method at lower noise levels. Moreover, the advantage of the Kalman filter over the LS method is more for the east direction. This relates to the higher autocorrelation of the E-field in the east direction as was mentioned earlier.

Figure 9.4 illustrates the effect of the outlier rate on the performance of the estimators. In this study, the Gaussian noise level and failure rate are set to zero. The Kalman filter outperforms the

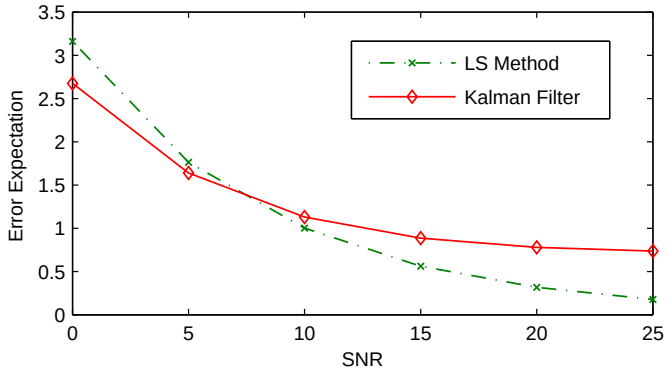


(a)

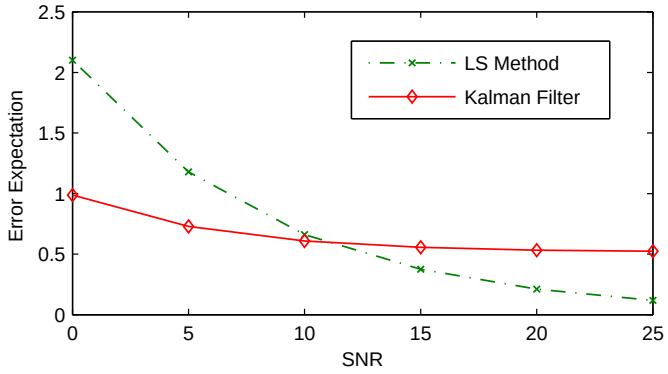


(b)

Figure 9.3: Effect of the Gaussian noise level on the performance of the Kalman filter and the LS estimator: Expectation of the estimation error in (a) north direction and (b) east direction.

LS estimator at higher outlier rates and falls below the LS estimator at lower outlier rates. The advantage of the Kalman filter is more in the east direction, which relates to the higher autocorrelation in this direction.

Accuracy comparison of the two estimators for different failure rates is presented in Fig. 9.5. In the east direction, the Kalman filter outperforms the LS method at higher failure rates and falls below at lower failure rates. In the north direction, both LS estimator and Kalman filter fail to estimate the electric filed with adequate precision. To improve the estimation accuracy in the north direction, more robust estimation approaches such as the least absolute value estimation and the Huber's estimator are encouraged [82].

As mentioned before, the dynamic model has lower accuracy in modeling the E-field of a stormy day as opposed to a normal day. The accuracy comparison of the two estimators in estimating the

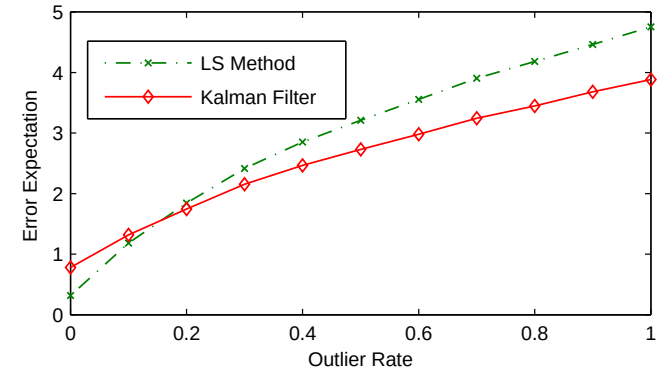


(a)

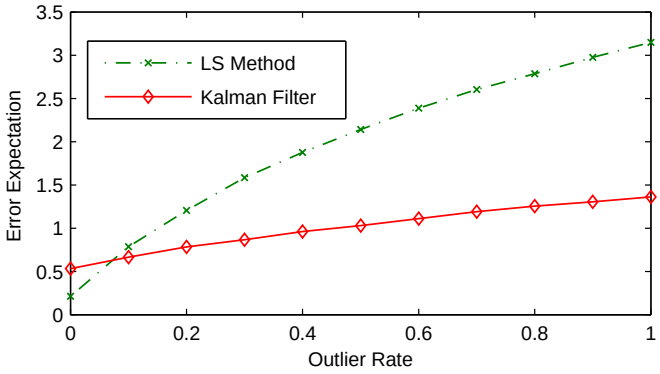


(b)

Figure 9.4: Effect of the outlier rate on the performance of the Kalman filter and the LS estimator: Expectation of the estimation error in (a) north direction and (b) east direction.

E-field of a normal day is presented in Fig. 9.6. Comparing this figure with Fig. 9.5, one can conclude that the advantage of the Kalman filter over the LS method is more for the normal days than for the stormy days. This relates to the fact that the dynamic model is more accurate for the normal days. the Kalman filter is built upon the dynamic model and its effectiveness depends on the accuracy of the dynamic model.

The effect of the E-field standard deviation on the accuracy of the Kalman filter is illustrated in Fig.9.7. Here, the E-field data for six different geomagnetic storms in 2011 are studied. the Kalman filter is used to estimate the E-field at three different outlier rates when the failure rate and Gaussian noise level are set to zero. Clearly, the estimation error correlates with the E-field standard deviation. When the standard deviation increases, the accuracy of the dynamic model declines. Hence the accuracy of the Kalman filter which is built upon that dynamic model will

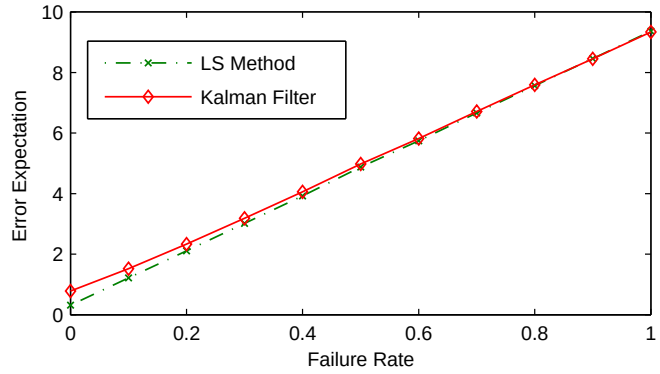


(a)

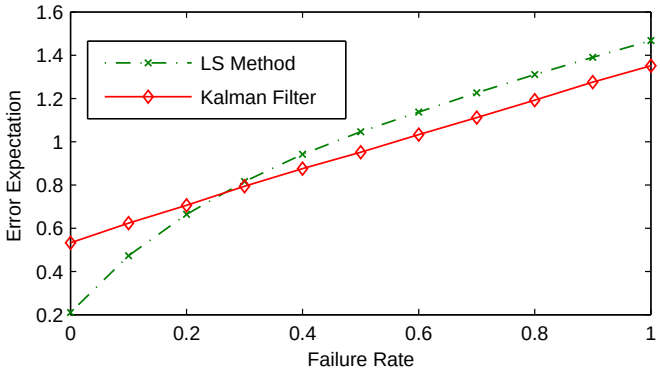


(b)

Figure 9.5: Effect of the failure rate on the performance of the Kalman filter and the LS estimator: Expectation of the estimation error in (a) north direction and (b) east direction

decrease as well.

The E-field estimations are compared with the actual data in Fig. 9.8. In this study, the outlier rate is $0.5$, SNR is $20$ and the failure rate is zero. Clearly, the E-field estimated by the Kalman filter agrees well with the actual data, whereas discrepancies are observed between the LS estimation and the actual one.

## 9.6 Conclusions

In this chapter, the dependency of E-field on its earlier observations is studied and its dynamic model is developed. Analyzing the actual E-field data for several geomagnetic storms indicates that the transition parameters of the dynamic model $a_N$ and $a_E$ have small variation over different

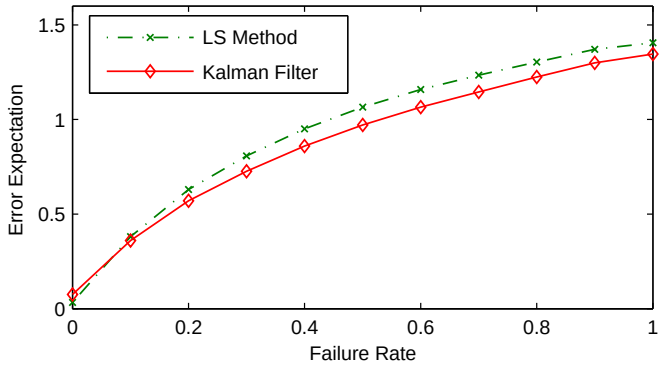


(a)

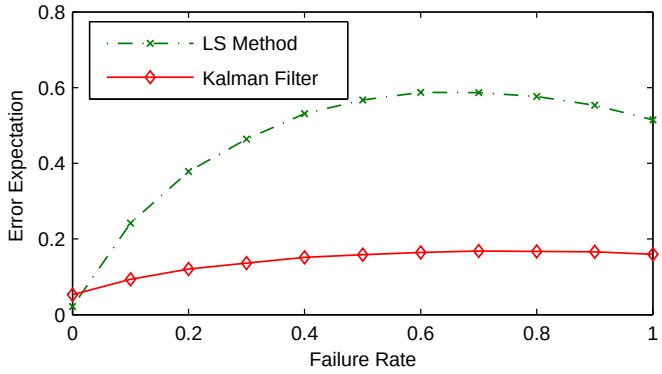


(b)

Figure 9.6: Effect of the failure rate on the estimation error using the E-field data of a normal day: Expectation of the estimation error in (a) north direction and (b) east direction.

datasets. This enables development of a general dynamic model which approximates the dynamics of any unknown E-field. Moreover, studying the E-field data of both stormy days and normal days, it is observed that the dynamic model is less accurate for stormy days compared to normal days.

This chapter utilizes the system dynamics to improve the E-field estimation. The dynamic model is integrated into the Kalman filter and better E-field estimation is obtained. The simulation results indicate that the Kalman filter outperforms the LS estimator at higher Gaussian noise levels, higher failure rates and higher outlier rates.

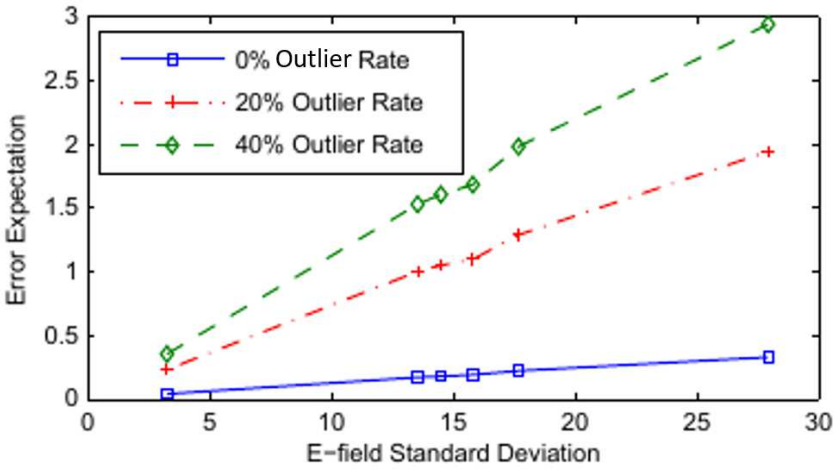


Figure 9.7: Effect of the E-field standard deviation on the accuracy of the Kalman filter.

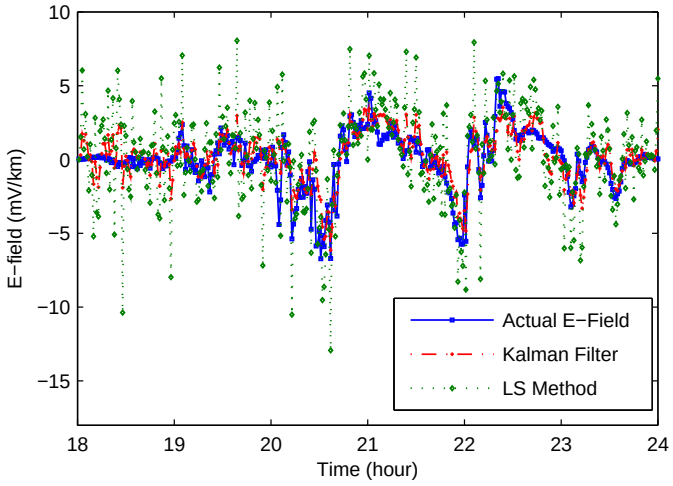


Figure 9.8: Accuracy comparison of the Kalman filter and LS method.

# CHAPTER 10

# ENHANCED E-FIELD ESTIMATION UNDER MEASUREMENT UNCERTAINTIES

## 10.1 Introduction

This chapter investigates the uncertainties in the GIC measurements and evaluates their impacts on the E-field estimation. Realistic noise scenarios for GIC measurements are considered and various estimators are introduced to handle different type of uncertainties. The LS estimator is used for GIC readings with white Gaussian noise, and the lease absolute value (LAV) estimator is utilized to handle outliers. Ridge Regression (RR) estimator is proposed as an alternative to LS method when additional information on the prior electric field is known. Moreover, a general probabilistic GIC measurement model has been developed. Using the probabilistic model, the accuracy and reliability of the LS estimator are derived analytically. The analytical results are verified numerically using the WECC 9-bus system and the 20-bus test case. Similar to Chapter 9, this chapter contributes to the resiliency of power systems against GMDs by providing better E-field estimation.

The chapter is organized as follows. LS, RR and LAV estimations are presented Section 10.2. In Section 10.3, a probabilistic model for the GIC measurements is developed. The reliability analysis of the LS estimator is the subject of Section 10.4. Numerical results are provided in Section 10.5.2 and the chapter is wrapped up in Section 10.6.

## 10.2 The Proposed E-Field Estimators

The GIC model is defined in (3.14) and its representation at one instant in time is reproduced below:

$$\mathbf{Z} = \mathbf{H}x + \mathbf{V} \tag{10.1}$$

Without prior information of $\mathbf{V}$, the most popular one is the ordinary LS estimator, as given by

$$\hat{\mathbf{X}}^{LS} := \arg\min_{\mathbf{X}} \|\mathbf{Z} - \mathbf{H}\mathbf{X}\|_2 = (\mathbf{H}^T\mathbf{H})^{-1}\mathbf{H}^T\mathbf{Z} \tag{10.2}$$

where $\|\cdot\|_2$ is the vector Euclidean norm. Assuming that the matrix $\mathbf{H}$ is full rank, the LS estimator has simple closed-form solution and thus is efficiently computable. It is also statistically optimal assuming $\mathbf{V}$ is white Gaussian of uniform variance.

If some GIC readings are corrupted outliers, i.e., some entries of $\mathbf{V}$ fail to follow the normal distribution, robust estimation approaches are necessary. A simple one of that kind is the LAV approach, as given by

$$\hat{\mathbf{X}}^{LAV} := \arg\min_{\mathbf{X}} \|\mathbf{Z} - \mathbf{H}\mathbf{X}\|_1 \tag{10.3}$$

where $\|\cdot\|_1$ denotes the vector Manhattan norm which is equal to the sum of entry-wise absolute values. Although there is generally no closed-form solution for (10.3), it can be transformed to a convex linear program, for which efficient solvers are available. The LAV estimator is less accurate if there are actually no outliers; thus, different robust estimators have been proposed to tackle this, such as Huber's Estimator or a more recent one motivated by sparsity [82].

Additional information on the prior of $\mathbf{V}$ could greatly improve the performance of linear estimators. If the relative covariance of $\mathbf{X}$ with respect to noise standard deviation is known, the RR may be used through augmenting the LS error criterion as

$$\begin{aligned}\hat{\mathbf{X}}^{RR} :&= \arg\min_{\mathbf{X}} \|\mathbf{Z} - \mathbf{H}\mathbf{X}\|_2^2 + \mathbf{X}^T(\lambda\mathbf{I})^{-1}\mathbf{E} \\ &= (\mathbf{H}^T\mathbf{H} + \lambda^{-1}\mathbf{I})^{-1}\mathbf{H}^T\mathbf{Z}\end{aligned} \tag{10.4}$$

where $\lambda\mathbf{I}$ is the relative covariance of $\mathbf{X}$. By incorporating the prior information on $\mathbf{X}$, the RR is especially powerful in improving the numerical stability when $\mathbf{H}$ is ill-conditioned. However, this introduces some bias on the estimator, which may be difficult to account for in practice. Note that the three estimators either have closed form expression or can be solved as a linear program. Hence, all the estimators enjoy low computational complexity.

## 10.3 Probabilistic Noise Modeling

Let $z$, $x$ and $v$ be the random variables representing the GIC measurements $\mathbf{Z}$, the E-field $\mathbf{X}$, and the measurement noise $\mathbf{V}$, respectively. Earlier investigations introduced white Gaussian noise, nonuniform Gaussian noise and sensor failure as the three major sources of error in the GIC measurements [54]. A general probabilistic model which captures these three types of measurement error is presented in this section.

### 10.3.1 Additive White Gaussian Noise

The noise generated by many natural sources is in the form of white Gaussian noise. White Gaussian noise is represented by a series of independent and identically distributed random variables with normal distribution given by

$$v = N_n = \mathcal{N}(0, \sigma^2)_{m\times 1} \tag{10.5}$$

where $\sigma$ is the standard deviation of white Gaussian noise and $m$ is the number of measurements.

### 10.3.2 Nonuniform Gaussian Noise

The Gaussian noise which is added to the GICs may not be identical for all the sensors and some of the sensors may encounter higher noise levels. Corrupted outliers are subjected to Gaussian noise with significantly higher standard deviation as given by

$$v = [\mathcal{N}(0, \sigma^2), \mathcal{N}(0, s_0\sigma^2), \cdots, \mathcal{N}(0, \sigma^2)]^T \tag{10.6}$$

where $s_o$ is the ratio of the noise level of the outliers to the normal measurements. This ratio is assumed to be the same for all the outliers in the system. However, this is not a critical assumption and more general models considering distinct outlier ratios can be developed.

A discrete random variable is defined to specify whether a sensor is an outlier as given by

$$u_o^k := \begin{cases} 1, & \text{if the } k\text{-th sensor is outlier} \\ 0, & \text{if the } k\text{-th sensor is not outlier} \end{cases} \tag{10.7}$$

where $u_o^k$ is the outlier variable for the $k$-th sensor. The probability distribution of this random variable is given by

$$\mathbf{P}_{u_o}(i) := \begin{cases} p_o, & i = 1 \\ 1 - p_o, & i = 0 \end{cases} \tag{10.8}$$

where $p_o$ is the outlier rate which is the probability of being an outlier and is assumed to be the same for all the sensors.

### 10.3.3 Faulty Sensors

Sometimes, the GIC device fails to measure the GIC and the output of the sensor is a random variable within the range of the sensor's reading as given by

$$z = \mathcal{U}(0, z_{\text{max}}) \tag{10.9}$$

where $\mathcal{U}(,)$ represents a random variable with uniform distribution and $z_{\text{max}}$ is the maximum value that the sensor can read.

A discrete random variable is defined to specify whether a sensor is faulty or not as given by

$$u_f^k := \begin{cases} 1, & \text{if the } k\text{-th sensor is faulty} \\ 0, & \text{if the } k\text{-th sensor is not faulty} \end{cases} \tag{10.10}$$

where $u_f^k$ is the fault variable for the $k$-th sensor. The probability distribution of this random

variable is given by

$$\mathbf{P}_{u_f}(i) := \begin{cases} p_f, & i = 1 \\ 1 - p_f, & i = 0 \end{cases} \tag{10.11}$$

In this equation, $p_f$ is the probability of being faulty and is assumed to be the same for all the sensors. $N_u = \mathcal{U}(0, z_{\max})_{m\times 1}$ is a vector of random variables with uniform distributions and is defined to represent the output of the faulty sensors.

### 10.3.4 Probabilistic Measurement Model

Using the random variables defined earlier, one can develop a general measurement model which captures various noise scenarios as given by

$$\begin{aligned} z =& (1 - u_f) \cdot (\mathbf{H}x + ([1]_{m\times 1} + (s_o - 1)u_o) \cdot N_n) \\ &+ u_f \cdot N_u \end{aligned} \tag{10.12}$$

Note that in this model, $u_f$ and $N_u$ are used to characterize the faulty sensors, $u_o$ captures the outliers and $N_n$ accounts for the uniform Gaussian noise scenario. The proposed measurement model is useful for studying the probability distribution of the estimation error and consequently evaluating the reliability of the estimator.

## 10.4 Reliability Analysis

The reliability of a system is the probability that it performs its intended function without failure for a specific period of time. The reliability of a system decays exponentially over time when the failure rate of the system is constant.

The reliability of an estimator is defined as the probability that its error does not exceed a threshold for a specific period of time. To calculate the estimator reliability, the probability distribution of the estimation error is studied and the estimator failure rate is calculated accordingly. Assuming

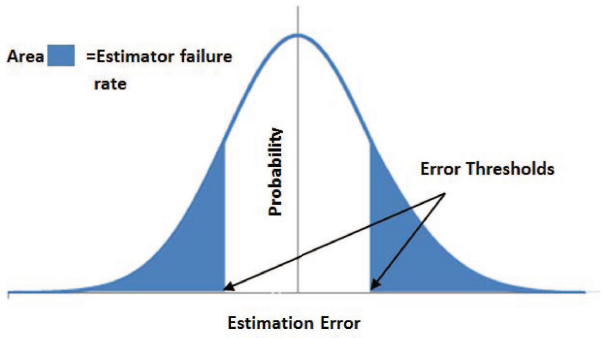


Figure 10.1: Probability distribution of the estimation error and the estimator failure rate.

constant failure rate for the estimator over time, the reliability of the estimator is determined by

$$\mathbf{R}(t) = \mathbf{Pr}\{t < T_f\} = e^{-\lambda t} \tag{10.13}$$

where $\lambda$ is the failure rate of the estimator and $T_f$ is the estimator time to failure.

To obtain the estimator failure rate, the probability distribution of the estimation error is required. The probability of estimation error has normal distribution when the observation noise is Gaussian. Hence, calculating the first and second moments of the estimation error completely parameterizes the error distribution. The probability distribution of the estimation error and the estimator failure rate under the Gaussian noise scenario are shown in Fig. 10.1.

Note that when there are faulty sensors in the system, the measurement noise is no longer Gaussian. In this case, the probability of the error no longer follows a normal distribution, and fitting it with a normal distribution causes inaccuracy in the reliability assessment. This phenomenon is demonstrated through an example in Section 10.5.2.

### 10.4.1 Expectation of Estimation Error

The probabilistic model in (10.12) is used to derive the expectation of GIC measurement as given by

$$\mathbf{E}[z] = (1 - p_f)\mathbf{H}\mathbf{E}[x] + p_f \frac{z_{\max}}{2} \times [1]_{m \times 1} \tag{10.14}$$

The estimated state obtained by LS estimation is presented in (10.2). Deriving the expectation of the estimated state from (10.2) and substituting into (10.14) gives rise to

$$\mathbf{E}[\hat{x}] = (1 - p_f)\mathbf{E}[x] + p_f \frac{Z_{\max}}{2}(\mathbf{H}^T\mathbf{H})^{-1}\mathbf{H}^T[1]_{N\times 1} \tag{10.15}$$

The expectation of electric field is zero, which zeros out the first term in (10.15). In the GIC model, the sum of entry-wise values of the columns in matrix $\mathbf{H}$ is zero, which zeros the second term in (10.15) as well. Hence, the expectation of estimation error is zero as given by

$$\mathbf{E}[e] = \mathbf{E}[x - \hat{x}] = \mathbf{E}[x] - \mathbf{E}[\hat{x}] = 0 \tag{10.16}$$

### 10.4.2 Second Moment of Estimation Error

To compute the second moment of the estimated state, the second moment of the observation should be determined as proposed by

$$\hat{x}\hat{x}^T = (\mathbf{H}^T\mathbf{H})^{-1}\mathbf{H}^T z z^T (\mathbf{H}^T\mathbf{H})^{-1}\mathbf{H}^{\mathbf{T}} \tag{10.17}$$

Using the GIC probabilistic model, the second moment of the observation is computed by

$$\begin{aligned}\mathbf{E}[zz^T] &= (\mathbf{E}[(1-u_f)(1-u_f)^T]) \cdot (\mathbf{H}\mathbf{E}[xx^T]\mathbf{H}^T) \\ &+(s_0-1)^2\mathbf{E}[(1-u_f)(1-u_f)^T] \cdot \mathbf{E}[u_o u_o^T] \cdot \mathbf{E}[N_n N_n^T] + \mathbf{E}[N_u N_u^T] \cdot \mathbf{E}[u_f u_f^T]\end{aligned} \tag{10.18}$$

where the cross moments of $N_u$, $u_o$ and $N_n$ are given by

$$\begin{aligned}\mathbf{E}[N_u N_u^T]_{(ij)} &= \begin{cases} \frac{z_{\max}^2}{3}, & i = j \\ \frac{z_{\max}^2}{4}, & i \neq j \end{cases} \\ \mathbf{E}[u_o u_o^T]_{(ij)} &= \begin{cases} p_o, & i = j \\ p_o^2, & i \neq j \end{cases} \\ \mathbf{E}[N_n N_n^T]_{(ij)} &= \begin{cases} \sigma^2, & i = j \\ 0, & i \neq j \end{cases}\end{aligned} \tag{10.19}$$

To compute $\mathbf{E}[zz^T]$, $\mathbf{E}[xx^T]$ which is the second moment of the actual state should be determined as proposed by (10.18). If prior information on the variance of the actual state is not available, a realistic state model should be developed to estimate it. A basic generative model for the electric field is $x = [\cos(\theta) \;\; \sin(\theta)]^T$ where $\theta = \mathcal{U}(0, 2\pi)$ is the angle of electric filed. Using more realistic models for the electric field provides higher accuracy. Future studies can extend this work by including more realistic models.

The power series for $\cos^2\theta$, $\sin^2\theta$ and $\cos\theta\sin\theta$ at $\theta = 0$ are given by

$$\begin{cases} \sin^2\theta = \sum_{k=1}^{\infty} \frac{(-1)^{k-1} 2^{2k-1} x^{2k}}{(2k!)} \\ \sin\theta\cos\theta = \sum_{k=0}^{\infty} \frac{(-1)^{k} 2^{2k} x^{2k+1}}{(2k+1!)} \\ \cos^2\theta = 1 - \sin^2\theta \end{cases} \tag{10.20}$$

These power series are used for calculating the second moment of the state as given by

$$\mathbf{E}[xx^T] = \begin{pmatrix} \mathbf{E}[\cos^2\theta] & \mathbf{E}[\sin\theta\cos\theta] \\ \mathbf{E}[\sin\theta\cos\theta] & \mathbf{E}[\sin^2\theta] \end{pmatrix} = \begin{bmatrix} 0.5 & 0 \\ 0 & 0.5 \end{bmatrix} \tag{10.21}$$

The second moment of estimation error is calculated by

$$\mathbf{E}[ee^T] = \mathbf{E}[\hat{x}\hat{x}^T] - (2p_f - 1) \begin{bmatrix} 0.5 & 0 \\ 0 & 0.5 \end{bmatrix} \tag{10.22}$$

## 10.5 Numerical Results

In this section, the accuracy of the LS, LAV and RR estimators under various noise scenarios is evaluated through numerical results. Moreover, analytical and numerical results are presented for the reliability analysis of the LS estimator.

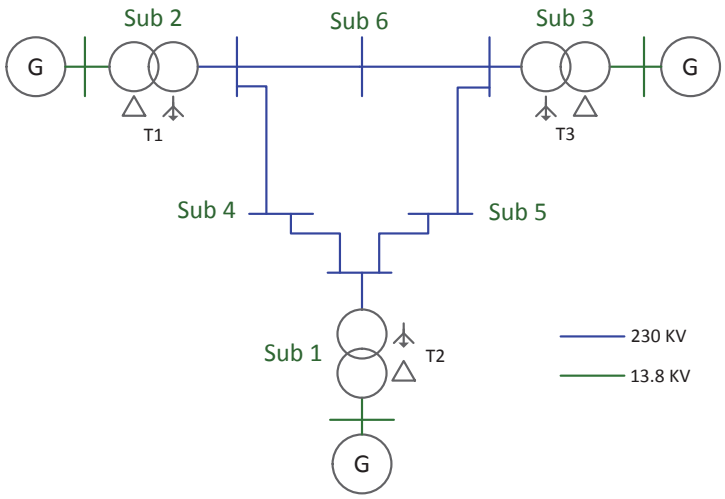


Figure 10.2: Single-line diagram of the 9-bus test case.

Table 10.1: Substation Location and Grounding Resistance for the 9-bus Test Case

| Name | Latitude | Longitude | Grounding Resistance ($\Omega$) |
|---|---|---|---|
| Sub1 | 39 | -88 | 0.38 |
| Sub2 | 41 | -89 | 0.38 |
| Sub3 | 40 | -87 | 0.38 |
| Sub4 | 40 | -88.5 | 0.47 |
| Sub5 | 40.5 | -88 | 0.47 |
| Sub6 | 39.5 | -87.5 | 0.47 |

### 10.5.1 Estimators Accuracy Evaluation

The first test case to study is a 9-bus system which is modified from the WECC standard 9-bus system [55] by including bus geographic coordinates, transformer neutral resistances, etc. This test case has six substations and three transformers as illustrated in Fig. 10.2. The geographic locations of the substations and their grounding resistances are presented in Table 10.1.

Variable electric field is enforced to the system. The magnitude of the enforced electric field is one and its angle is a random variable between 0 and $2\pi$ with uniform distribution. Monte Carlo simulation with 1000 realizations is investigated to perfectly simulate the randomness of electric field angle.

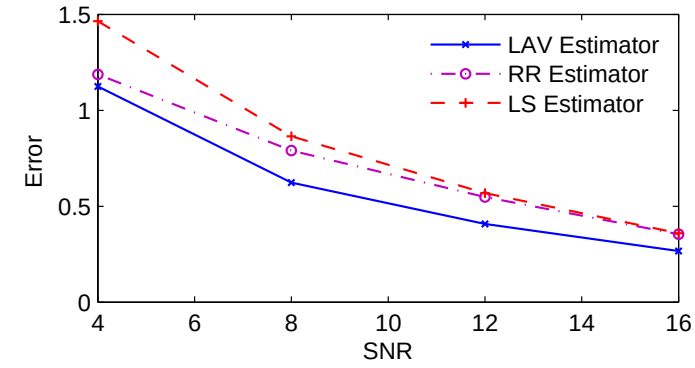


(a)

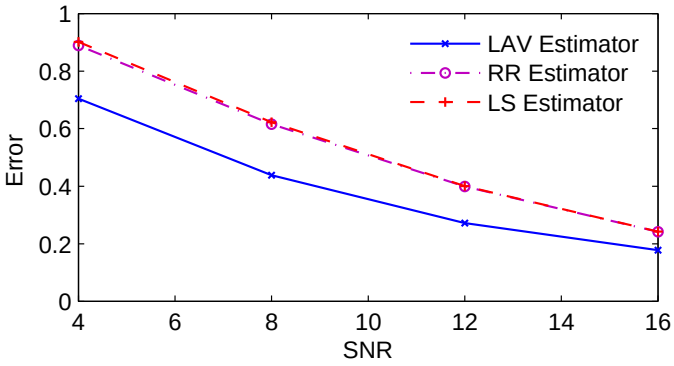


(b)

Figure 10.3: Estimation error versus SNR for the 9-bus test case under uniform Gaussian noise: (a) magnitude and (b) angle of electric field.

Table 10.2: Transformers Coefficients for the 9-bus Test Case

| Name | $\mathbf{H}^N$ | $\mathbf{H}^E$ |
|---|---|---|
| T1 | -35.638 | 1.999 |
| T2 | 49.358 | -46.47 |
| T3 | -13.721 | 44.471 |

The GICs induced by the electric field are determined via solving the GIC flow program in PowerWorld Simulator. Table 10.2 presents the coefficients of the three transformers. The coefficient matrix is full rank which ensures the effectiveness of LS estimator.

The GICs obtained from the GIC flow program represent ideal measurements. The noisy measurements are obtained by adding white Gaussian or nonuniform noise to the ideal GIC values. The investigated Monte Carlo simulation incorporates the randomness in additive noise. Figure

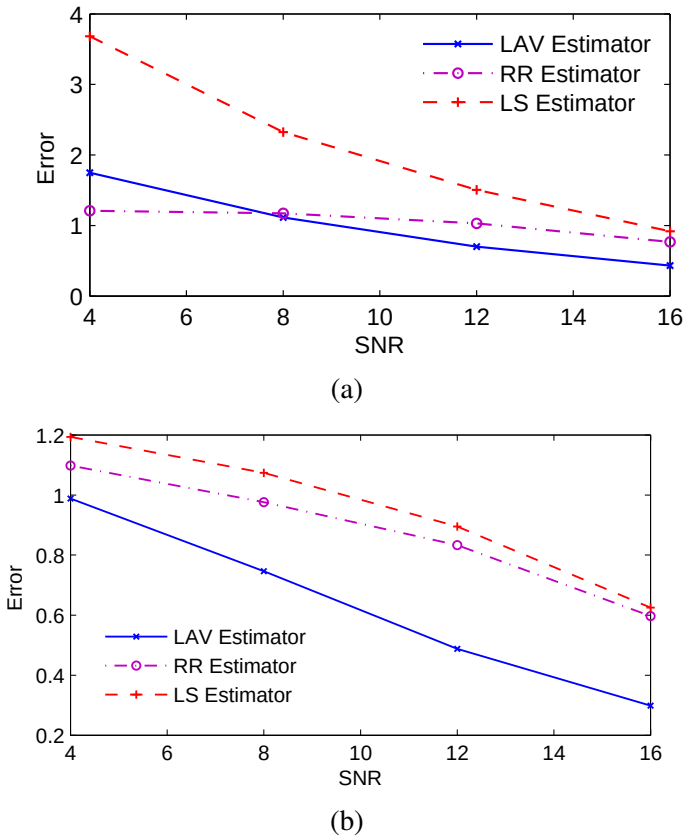


Figure 10.4: Estimation error versus SNR for the 9-bus test case under nonuniform Gaussian noise: (a) Magnitude and (b) angle of Electric Field.

10.3 illustrates the accuracy of LS, RR, and LAV estimators when the GIC measurements are subjected to white Gaussian noise. Clearly, the LS estimator outperforms the LAV in estimating both magnitude and angle when the measurement noise is purely white Gaussian.

Ridge Regression (RR) estimator can be used as an alternative to LS estimator when the relative covariance of the electric field is known. The additional information on $\mathbf{V}$ improves the performance as illustrated in Fig. 10.3. The advantage of the RR estimator over the LS is more for smaller SNRs which encourages the application of the former at higher noise levels. Moreover, the improvement of the RR estimator over the LS estimator is higher for the magnitude than for the angle.

To have nonuniform noise, the noise standard deviation at the third substation is increased by 5 times, which means the corresponding measurement can be considered as an outlier. Figure 10.4

shows the improvement of LAV estimator over the LS under this setup. Comparing the uniform and nonuniform noise scenarios, the LAV estimation error is almost the same for both uniform and nonuniform noise scenarios, whereas the LS estimation error is significantly higher for the nonuniform noise scenario.

Employing RR estimator instead of the LS improves the estimations in the same fashion as the uniform noise scenario. In fact, the accuracy of RR estimator in magnitude estimation is as good as that of the LAV under this setup, which results from the additional information.

Next, the accuracy of the three estimators is evaluated in the case of faulty sensors. To simulate this, the GIC at the third substation is replaced by a white Gaussian noise which has zero coherence with the original GIC. The standard deviation of the replaced Gaussian noise is equal to the GIC norm at the substation. The accuracy of the LS and RR estimators decreases significantly in the presence of faulty sensors as shown in Fig. 10.5. The accuracy of the LAV estimator is not affected as it detects the outliers and eliminates them from the estimations process.

The second test case to study is the 20-bus system. Similar to the 9-bus test case, an E-field is enforced to the system which has unity magnitude and random angle with uniform distribution between 0 and $2\pi$. Figure 10.6 illustrates the error norm for all three estimators when the GIC measurements are subjected to white Gaussian noise. Clearly, LS and RR estimators outperform the LAV under this setup. To generate nonuniform noise, one of the transformers is randomly selected and the standard deviation of its noise is increased by 5 times. The randomness of this selection is modeled through Monte Carlo simulation. The accuracy of the LAV estimator improves over the LS and RR under this noise scenario as shown in Fig. 10.7.

The accuracy comparison of the RR and LS estimators for the 20-bus system agrees with that for the 9-bus test case. For both systems, the improvement of the RR estimator is higher for the magnitude estimation and also at smaller SNRs. Comparing the results for the two test cases, one can conclude that the advantage of the RR estimator over the LS is more for the smaller systems. This may relate to the data redundancy in the larger system which reduces the advantage of prior knowledge about $\mathbf{X}$.

In Fig. 10.8, the number of outliers is increased by randomly selecting more transformers and increasing their noise level by five times. Clearly, the number of outliers does not limit the performance of the LAV estimator and this estimator outperforms the others for any number of outliers.

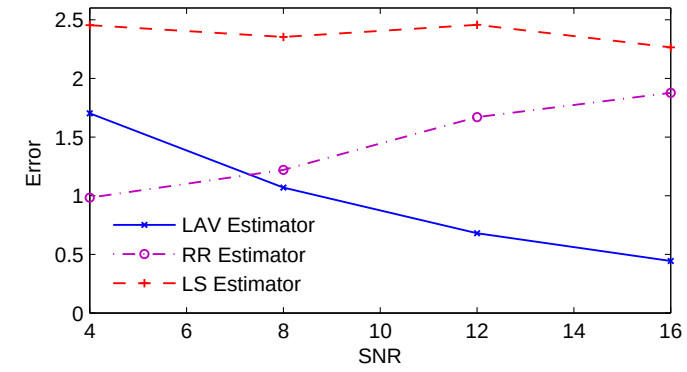


(a)

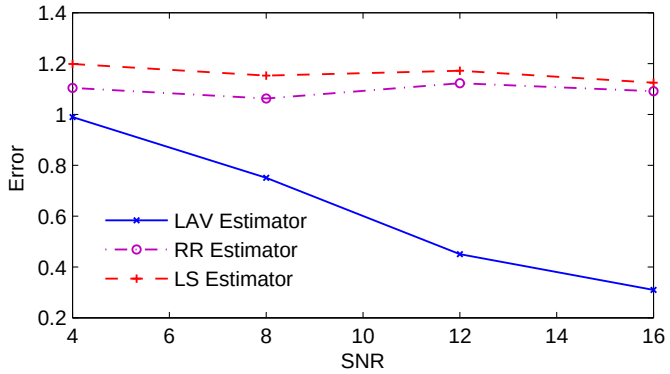


(b)

Figure 10.5: Estimation error versus SNR for the 9-bus system and in the case of having faulty sensors: (a) Magnitude and (b) angle of Electric Field.

To investigate faulty measurements, one of the transformers is randomly selected and its GIC is replaced by white Gaussian noise. The standard deviation of the replaced Gaussian noise is equal to the Manhattan norm of the transformer GIC. The accuracy comparison of the three transformers under this setup is illustrated in Fig. 10.9. Similar to the 9-bus system, LAV estimator outperforms the other two for this noise scenario.

### 10.5.2 Reliability Analysis of the LS Estimator

In this section, the analytical derivations of the error distribution and the reliability for the LS estimator are verified through numerical results. Variable electric field is enforced to the system. The magnitude of the enforced electric field is $1(\frac{V}{km})$ and its angle is a random variable between $0$

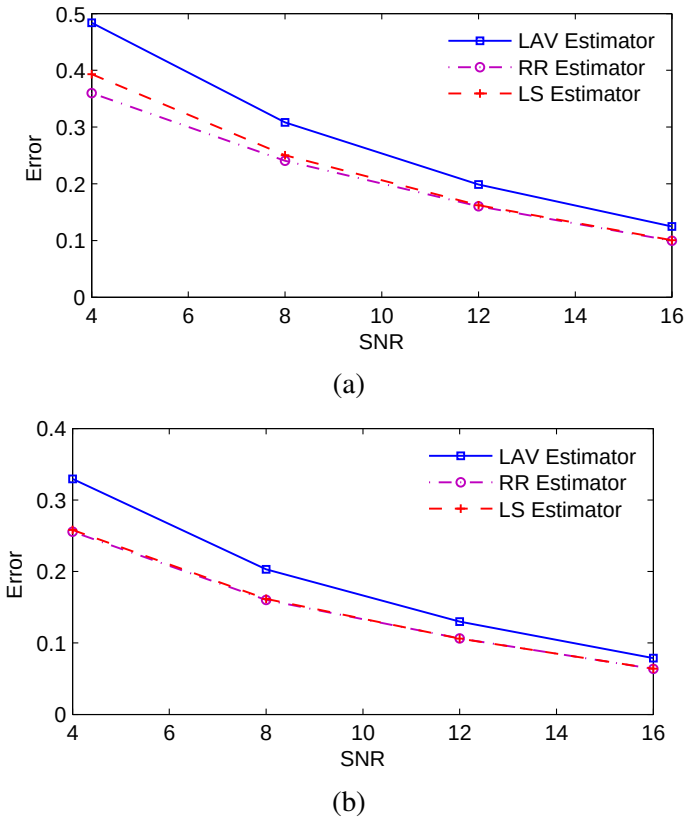


Figure 10.6: Estimation error versus SNR for the 20-bus test case under uniform Gaussian noise: (a) Magnitude and (b) angle of Electric Field.

and $2\pi$ with uniform distribution. Monte Carlo simulation with $1000$ realizations is investigated to simulate the angle randomness.

The GICs induced by the electric field are determined via solving the GIC flow program in PowerWorld Simulator. The GICs obtained from the GIC flow program represent ideal measurements. The probabilistic model in (10.12) is used to obtain the noisy measurements and Monte Carlo simulation is used to simulate its randomness. The analytical results presented earlier indicate that the expectation of estimation error is zero. Monte Carlo simulation is used to calculate the error expectation in the north direction and a similar result is obtained as shown in Fig. 10.10. For conciseness, the results are presented only in the north direction throughout the subsection.

The second moment of the estimation error direction at different failure rates is illustrated in Fig. 10.11. The Gaussian noise level and outlier rate are set to zero in this study. Clearly, the

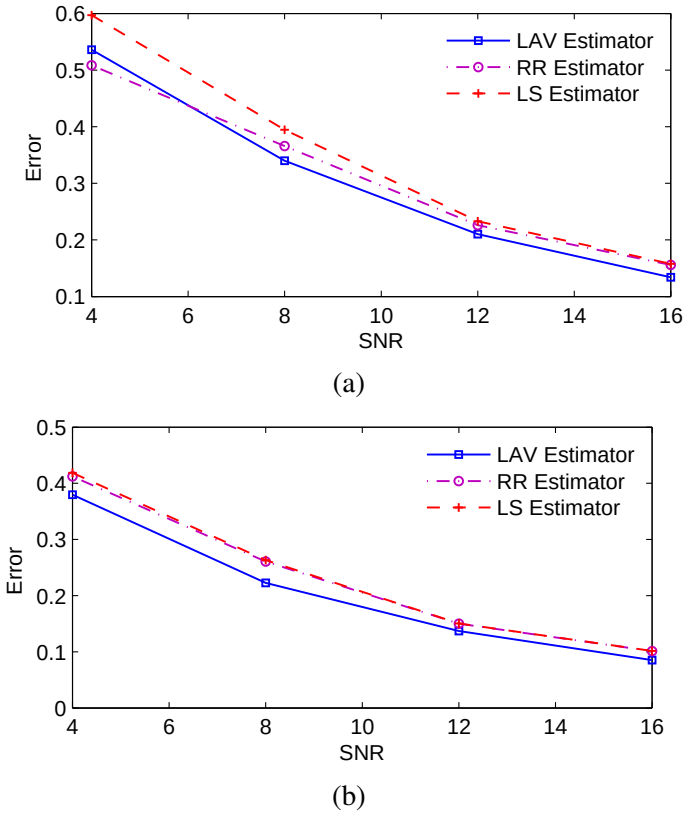


Figure 10.7: Estimation error versus SNR for the 20-bus test case under nonuniform Gaussian noise: (a) Magnitude and (b) angle of Electric Field.

mathematical model agrees well with the simulations. According to this figure, the second moment of the error has a quadratic relation with the sensor failure rate, $p_f$.

The effect of outlier rate on the second moment of estimation error is shown in Fig. 10.12. In this calculation, the failure rate is zero and the signal-to-noise ratio (SNR) is $15$ dB. According to the figure, the mathematical model and the simulation both demonstrate the linear dependence of error variance on the outlier rate, $p_o$.

Figure 10.13 presents the second moment of the estimation error in north direction at different Gaussian noise levels. In this calculation, the failure rate is zero and the outlier rate is $5\%$. Clearly, the mathematical model is consistent with the simulation results.

The reliability of the LS estimator is shown in Fig. 10.14. In this study, the SNR is $15$ dB and $10\%$ error is used as the threshold error. The failure rate is zero and the measurement noise is

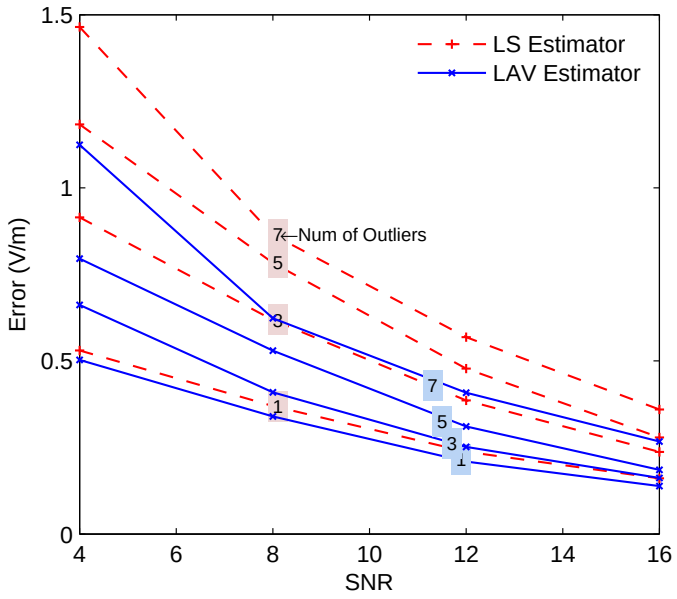


(a)

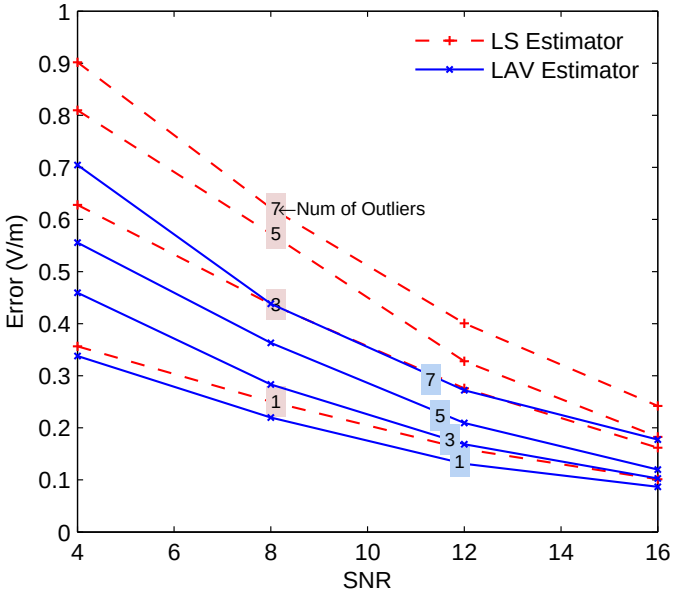


(b)

Figure 10.8: Estimation error versus SNR for the 20-bus system and for various number of outliers: (a) magnitude and (b) angle of electric field.

Gaussian. Hence, the estimation error follows a normal distribution. Equations (10.16) and (10.22) are used to obtain the expectation and variance of the error distribution. The estimator failure rate

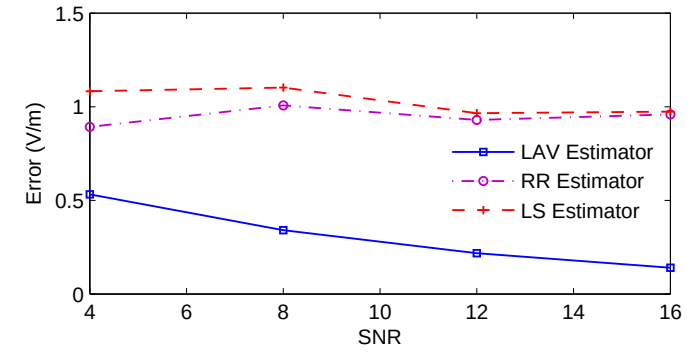


(a)

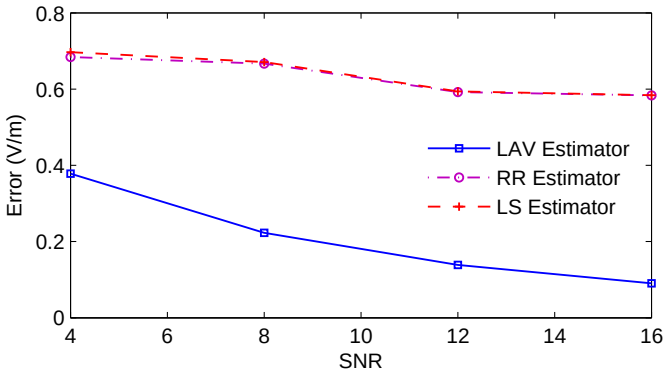


(b)

Figure 10.9: Estimation error versus SNR for the 20-bus system and in the case of having faulty sensors: (a) magnitude and (b) angle of electric field.

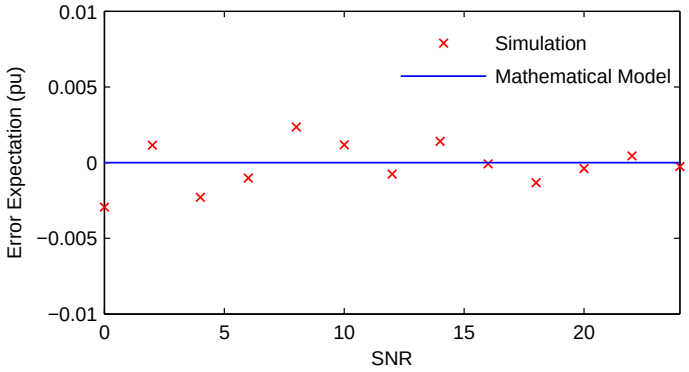


Figure 10.10: Expectation of estimation error at different Gaussian noise levels.

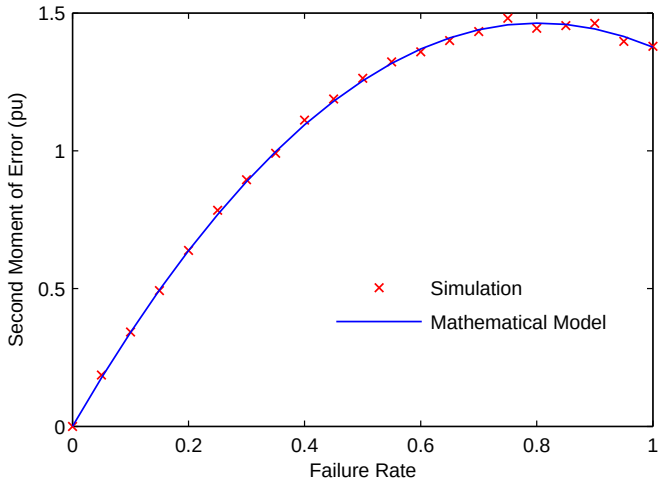


Figure 10.11: Effect of failure rate on the second moment of LS estimation error.

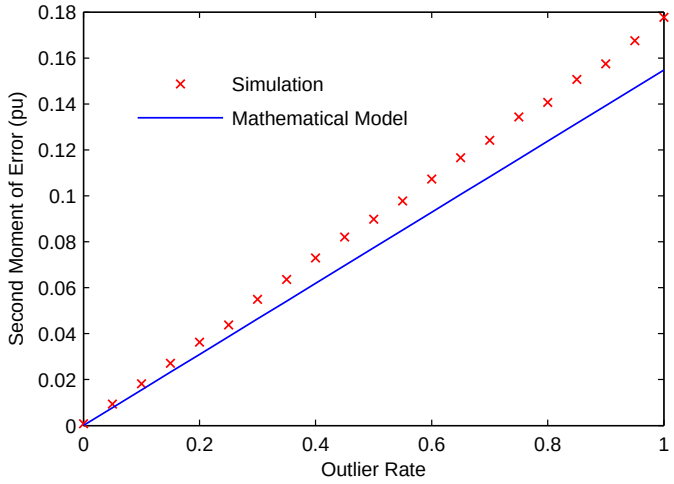


Figure 10.12: Effect of outlier rate on the second moment of LS estimation error.

is calculated according to Fig. 10.1 and the reliability is determined accordingly. In the figure, the analytical model and the simulation are termed as "AM" and "Sim", respectively. Clearly, the analytical model agrees well with the simulation.

According to Fig. 10.14, the reliability curves follow exponential decay and their time constants depend on the sensor outlier rate. The variation of estimator failure rate with the sensor outlier rate is shown in Fig. 10.15. The reliability of the estimator declines as the outlier rate increases.

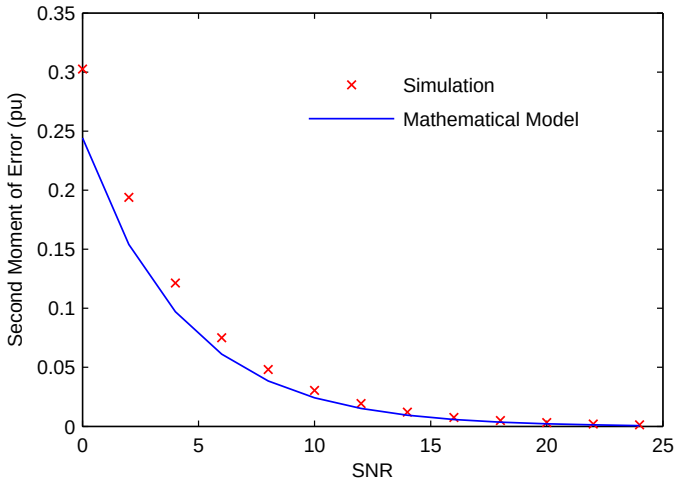


Figure 10.13: Second moment of LS estimation error and its variation with Gaussian noise level.

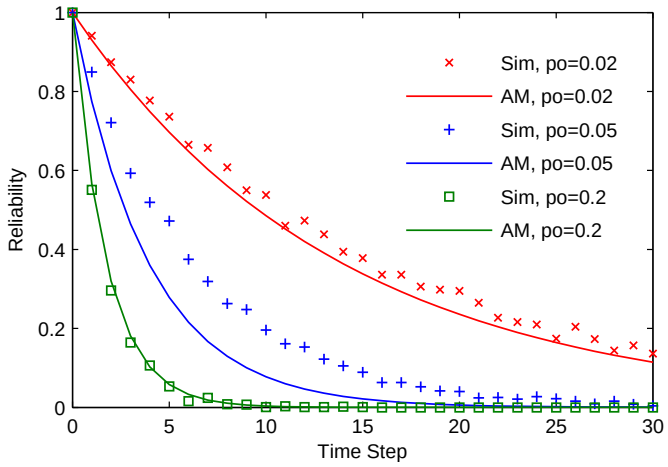


Figure 10.14: Reliability of LS estimator at different outlier rates.

Figure 10.16 illustrates the effect of Gaussian noise level on the estimator failure rate. In this calculation, the failure rate is zero and the outlier rate is $5\%$. The mathematical model provides good accuracy in calculating the estimator failure rate.

Variation of the estimator failure rate with the sensor failure rate is presented in Fig. 10.17. The Gaussian noise level and outlier rate are set to zero. When the sensor failure rate is not zero, the measurement noise is not Gaussian and the assumption of having normally distributed

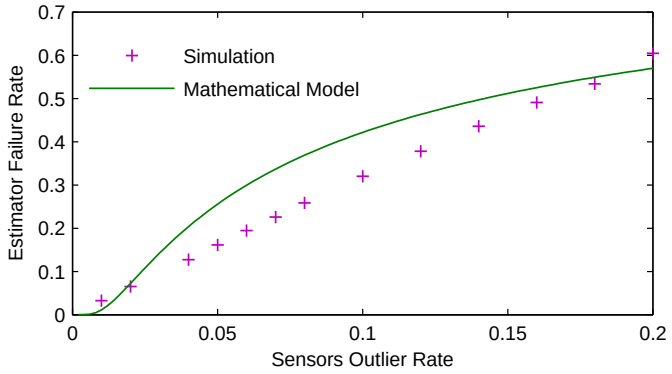


Figure 10.15: Variation of estimator failure rate with the outlier rate of the sensor.

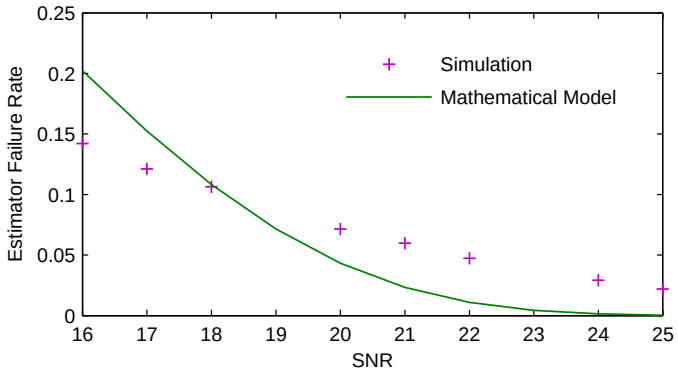


Figure 10.16: Effect of Gaussian noise level on the estimator failure rate.

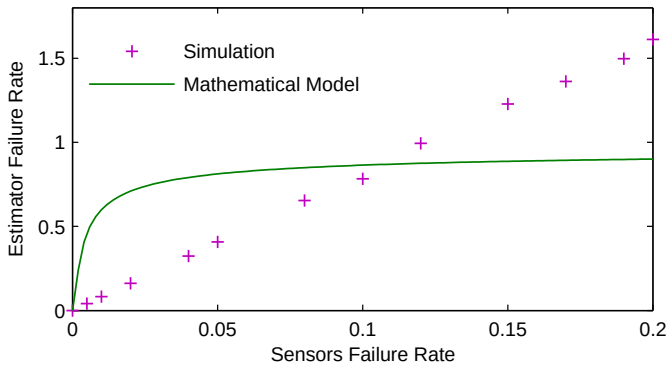


Figure 10.17: Variation of the estimator failure rate with the failure rate of the sensors.

error no longer holds. Hence, the mathematical model fails to accurately estimate the reliability and a discrepancy is observed between the mathematical model and the simulation. A possible approach to solve this problem is to calculate the higher order moments of the estimation error and approximate the error distribution based on its higher order moments. Further studies are necessary to tackle this problem.

## 10.6 Conclusions

This chapter analyzes the impact of the GIC measurement error on the accuracy of the E-field estimation. Realistic noise scenarios are considered for GIC measurements and suitable estimators are proposed to handle different types of uncertainties. A probabilistic model for GIC measurements has been developed. Using the developed model, the moments of the estimation error are calculated. Moreover, an analytical model for assessing the estimator's reliability has been developed. Numerical results indicate that the proposed model can effectively evaluate the estimator's reliability when the system is subject to Gaussian noise. In the case of faulty sensors, the estimation error no longer follows the normal distribution and thus the proposed reliability assessment technique fails. This opens up future research on enhancing the reliability assessment framework with respect to sensor failures.

# CHAPTER 11

# ADDING GMD MODELS TO THE EXISTING TEST CASES

## 11.1 Introduction

Realistic public test cases can facilitate the studies on the GMDs impacts on the power system by providing a benchmark to validate the related analysis tools. Many standard test cases are available for different aspects of power system analysis. These cases are designed for ac analysis and do not contain the necessary inputs such as the substation grounding resistances and the geographic coordinates which are essential for GMD studies. In this chapter, a framework is proposed to generate GMD-related parameters for the existing standard power system test cases. The substation geographic coordinates are the key parameters which are missing in the existing cases. The Kamada and Kawai (KK) algorithm and the Force-directed (FD) method are presented as two effective graph drawing algorithms to generate the geographic layout and determine the coordinates. The effectiveness of the proposed framework is evaluated through numerical results using the 20-bus system and the IEEE 24-bus system.

The tool developed in this chapter can improve many aspects of the GMD analysis by providing suitable benchmarks for evaluation purposes. This includes all the GMD-related studies in this thesis. Most of the analysis is performed on the 20-bus system since it is one of the few test cases available for GMD studies. Extending the analysis to other systems can provide better performance evaluation.

The chapter is organized as follows: The framework for determining the GIC-related parameters is presented in Section 11.2. Section 11.3 demonstrates the proposed technique through numerical results. Section 11.4 presents a conclusion and direction for future work.

## 11.2 Determining the GIC-related Parameters

The key parameters required for GMD analysis, which are usually missing in standard test cases, are the substation grounding resistances and geographic coordinates. A rather simplistic model for determining the substation grounding resistances is used in [45]. In this model, the assumed resistance depends on the highest substation voltage level and its assumed size (based on the number of lines coming into the substation), with larger, higher voltage substations having lower values. Soil resistivity, which certainly can have an impact, is not included in this simplistic model. Ballpark values are usually substantially below 0.5Ω for 230kV and above substations, and between 1 and 2Ω for the lower voltage substations.

The geographic coordinates may be obtained through developing a geographic layout of the system using the existing graph drawing techniques as described in the following.

### 11.2.1 Force-directed Graph Drawings

Force-directed graph drawings is a method for drawing graphs in a way that looks pleasant to the eye [93]. The vertices of the graph are positioned in two-dimensional or three-dimensional space so that the edges are about the same length and the number of crossings is minimized. The algorithm assigns forces among the set of edges and the set of vertices and uses these forces to simulate the movement of the vertices or to minimize their energy. Attractive forces like springs are used to attract the vertices that are connected in the graph (based on Hooke's law). Repulsive forces like electrically charged particles are used to separate all pairs of vertices (based on Coulomb's law). The layout is obtained by solving for the equilibrium state of this system of forces. In equilibrium, the edges have similar lengths because of the spring attractions and the vertices are as far as possible from each other due to the electric repulsive forces.

The attractive and repulsive forces between a pair of vertices are defined as

$$\begin{cases} f_a(d) = \frac{d^2}{k} \\ f_r(d) = -\frac{k^2}{d} \end{cases} \tag{11.1}$$

where $f_a$ and $f_r$ are respectively the attractive and repulsive forces and $d$ is the distance between

the pair of vertices. $k$ is the optimal distance between the vertices as given by

$$k = C\sqrt{\frac{area}{number\ \ of\ \ vertices}} \tag{11.2}$$

where $C$ is a constant.

### 11.2.2 Kamada and Kawai Algorithm

the FD method does not preserve the distances between the vertices and the edges and the resulting layout has uniform lengths. Sometimes, it is desired to maintain the distances, especially in GMD applications where the line lengths have significant impact on the GIC flows. the KK algorithm minimizes the difference between the ideal lengths and actual ones instead of minimizing the number of edge crossings [94]. Unlike the FD algorithm, no repulsive forces are considered between vertices. Spring forces are used between all pairs of vertices, with ideal spring lengths equal to the vertices' graph-theoretic distance. The optimal layout is obtained by minimizing the total spring energy.

Let $n$ be the number of vertices and $p_1, p_2, \cdots, p_n$ be the particles in a plane representing the vertices $v_1, v_2, \cdots, v_n$ respectively. The energy of the system is given by

$$E = \sum_{i=1}^{n-1} \sum_{j=i+1}^{n} \frac{1}{2} k_{ij}(|p_i - p_j| - l_{ij}) \tag{11.3}$$

where $l_{ij}$ is the desired length of the spring between $p_i$ and $p_j$ and is calculated by

$$l_{ij} = \frac{L_0}{\max\limits_{i \leq j} d_{ij}} d_{ij} \tag{11.4}$$

where $d_{ij}$ is the distance between $v_i$ and $v_j$ and $L_0$ is the length of the display area. $k_{ij}$ is the strength of the spring between $p_i$ and $p_j$ as expressed in:

$$k_{ij} = \frac{K^{spr}}{d_{ij}^2} \tag{11.5}$$

where $K^{spr}$ is a constant. For a two-dimensional space, the particle $p_i$ is represented by the rect-

angular coordinates $(x_i, y_i)$ and the system energy in (11.3) is given by

$$E = \sum_{i=1}^{n-1} \sum_{j=i+1}^{n} \frac{1}{2} k_{ij} \{(x_i - x_j)^2 + (y_i - y_j)^2 + l_{ij}^2 - 2l_{ij}\sqrt{(x_i - x_j)^2 + (y_i - y_j)^2}\} \tag{11.6}$$

The necessary condition of the local minimum is as follows:

$$\frac{\partial E}{\partial x_m} = \frac{\partial E}{\partial y_m} = 0, \qquad 1 \leq m \leq n \tag{11.7}$$

The partial derivative of the energy with respect to $x$ and $y$ is expressed in:

$$\begin{aligned} \frac{\partial E}{\partial x_m} &= \sum_{i \neq m} k_{mi} \{(x_m - x_i) - \frac{l_{mi}(x_m - x_i)}{\sqrt{(x_m - x_i)^2 + (y_m - y_i)^2}}\} \\ \frac{\partial E}{\partial y_m} &= \sum_{i \neq m} k_{mi} \{(y_m - y_i) - \frac{l_{mi}(x_m - x_i)}{\sqrt{(x_m - x_i)^2 + (y_m - y_i)^2}}\} \end{aligned} \tag{11.8}$$

This gives rise to a system of $2n$ nonlinear equations and Newton-Raphson may be used for solving it.

Note that KK requires the line lengths as input. However, the lengths are not usually available for the synthetic cases. To address this, the line resistances may be used as a criterion to determine the lengths. The line resistance depends on its conductor type, the conductor bundling structure and the length. The conductor type and the bundling structure depend on the voltage level. Heuristics may be developed to get the resistance per meter for different voltage levels through the statistical analysis of the real power systems. Using the resistance (available in standard test cases) and the estimated resistance per line, the line length can be estimated.

## 11.3 Numerical Results

In this section, the geographic layouts of two power systems are developed using the proposed algorithms. The first system to study is the 20-bus system in [38]. This test case includes many features found in typical high voltage transmission networks. The case is designed specifically

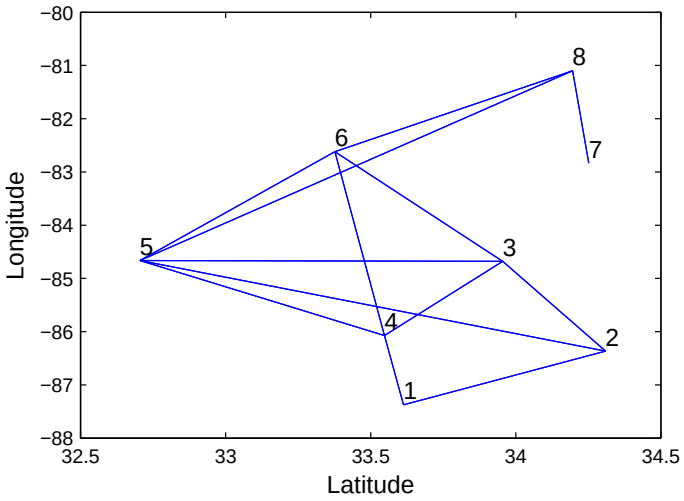


Figure 11.1: Geographic layout of the system using the available coordinates.

for GMD applications and contains substation geographic coordinates. Figure 11.1 illustrates the geographic layout of the system using the available coordinates.

The KK algorithm is utilized to develop a geographic layout. The coordinates are not provided to the algorithm and are to be estimated. Instead, the line lengths are calculated from the coordinates and are given to the algorithm:

$$
\begin{aligned}
a &= sin^2(\frac{\phi_2 - \phi_1}{2}) + cos(\phi_1)cos(\phi_2)sin^2(\frac{\lambda_2 - \lambda_1}{2}) \\
c &= 2atan2(\sqrt{a}, \sqrt{1-a}) \\
d &= Rc
\end{aligned} \tag{11.9}
$$

where $\phi$ and $\lambda$ are latitude and longitude respectively, $d$ is the distance between points 1 and 2 (in mile), and $R$ is the Earth radius, i.e. 6,371 km. Figure 11.2 illustrates the resulting layout obtained from KK algorithm. Comparing this layout with the actual one in Fig. 11.1, it is observed that the layout developed by the KK algorithm preserves the lengths, but does not capture the original layout. This is because developing the layout from only the line lengths does not provide a unique solution and additional information is required to retrieve the original layout.

The line lengths are calculated for the layout developed by the KK algorithm and are compared

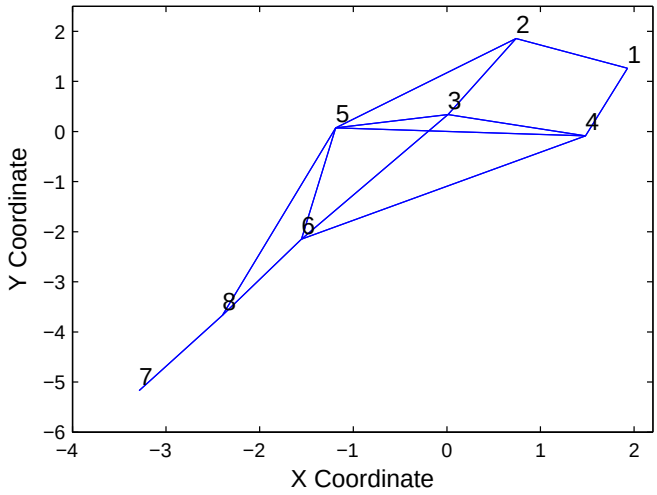


Figure 11.2: Geographic layout of the 20-bus system obtained from KK algorithm.

with the actual ones derived from the coordinates. This comparison is illustrated in Fig. 11.3. The obtained lengths agree well with the actual ones, except for occasional mismatches.

Next, the geographic layout is calculated through the FD algorithm as illustrated in Fig. 11.4. The resulting layout has only one crossing and the line lengths are almost uniform. The algorithm uses only the incident matrix as input and the actual line lengths are ignored.

The second system to study is the IEEE 24-bus system. This system is designed for ac analysis and does not contain the substation geographic coordinates. To make it suitable for GMD studies, the KK algorithm is utilized to develop a geographic layout of the system and consequently obtain the substation coordinates. The resulting layout is shown in Fig. 11.5. The KK algorithm takes the incident matrix and the line lengths as input. The required line lengths are collected from the available data in [95]. Note that the line lengths are not usually available for the synthetic standard cases and the line resistances may be used to estimate them as described in Section 11.2. Alternatively, the FD method may be used instead of KK algorithm to get the layout since it does not require the line lengths.

The line lengths obtained from the KK layout are compared with the actual lengths in Fig. 11.6. There is relatively good agreement between the obtained and actual lengths.

Next, the layout is obtained using the FD method as shown in Fig. 11.7. Unlike the KK layout,

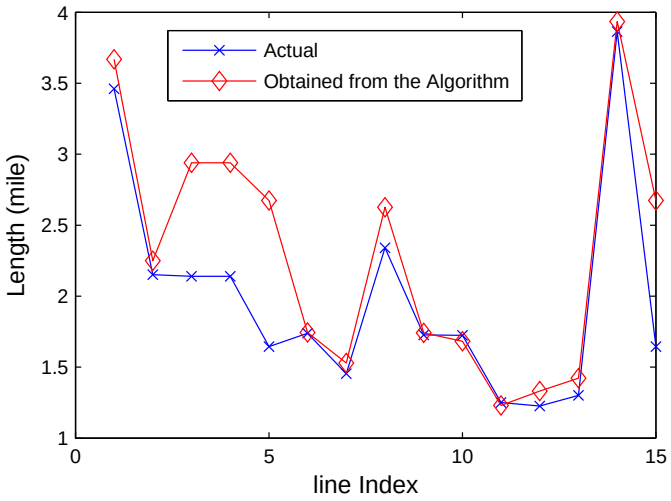


Figure 11.3: Comparison of the line lengths obtained from the KK algorithm with the actual ones for the 20-bus system.

that had many crossings and looked very crowded; this layout has only one crossing and appears aesthetically pleasant to the eye. The line lengths are almost uniform and bear no correlation with the actual lengths.

Pearson correlation coefficient is used to measure the correlation between the actual lengths and those obtained from the investigated layout designs. Table 11.1 presents the correlation coefficients for both drawing methods and the two investigated systems. It is observed that the KK algorithm provides much better correlation than the FD method. Moreover, the correlations are higher for the EPRI 20-bus case than the IEEE 24-buse system. This could relate to the fact that the 20-bus case was originally designed for GMD studies and has an actual geographic layout. On the other hand, the 24-bus system may not have been designed based on a real geographic layout, and therefore, there might be no feasible layout that can correlate well with the available line lengths. Further exploration into the feasibility of the geographic layout given a set of line lengths will be an interesting future direction.

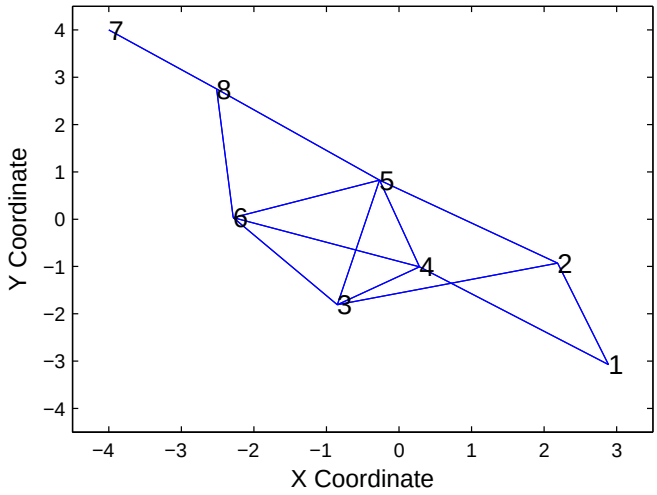


Figure 11.4: Geographic layout of the 20-bus system obtained from FD method.

Table 11.1: Grounding Resistances of the 20-bus Test Case

| Test Case | Kamada-Kawai | Force-directed |
|---|---|---|
| IEEE 24-bus | 0.694 | 0.1711 |
| EPRI 20-bus | 0.8554 | 0.3441 |

## 11.4 Conclusions

In this chapter, a framework is proposed to incorporate GMD modeling into the already existing standard power system cases. The geographic coordinates are the key parameters that are missing in the standard cases and are essential for GMD studies. KK and BF are presented as two effective graph drawing techniques to generate the geographic layout and consequently get the coordinates. The proposed framework is applied to the 20-bus and 24-bus systems and their coordinates are determined. Numerical results indicate that the layout obtained from KK preserves the line lengths, while BF provides a layout which is aesthetically pleasing, but its resulting lengths have little correlation with the actual lengths.

The study suggests several directions for future research: First, the algorithm can be applied to other standard test cases such as the IEEE 118-bus or 300-bus systems. Second, the algorithm for estimating the line lengths from their resistances were described briefly. This algorithm can be fur-

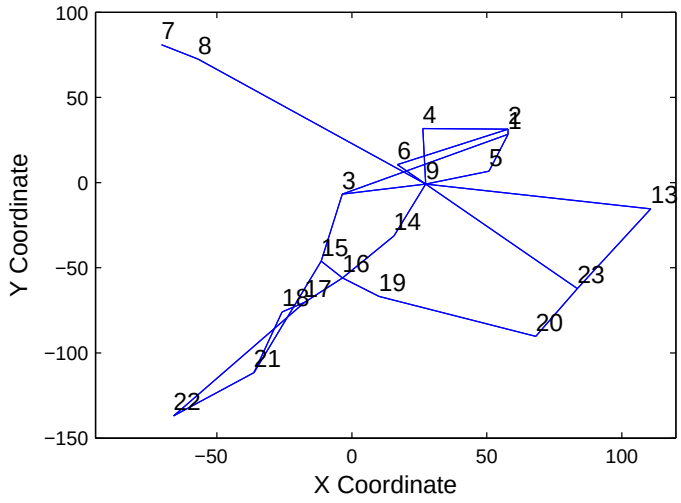


Figure 11.5: Geographic layout of the IEEE 24-bus system obtained from KK algorithm.

ther refined and statistical analysis of the actual systems may be utilized to verify its effectiveness. Last, the effectiveness of the test cases generated from the proposed framework may be validated by performing GMD studies on the generated case and evaluating the results.

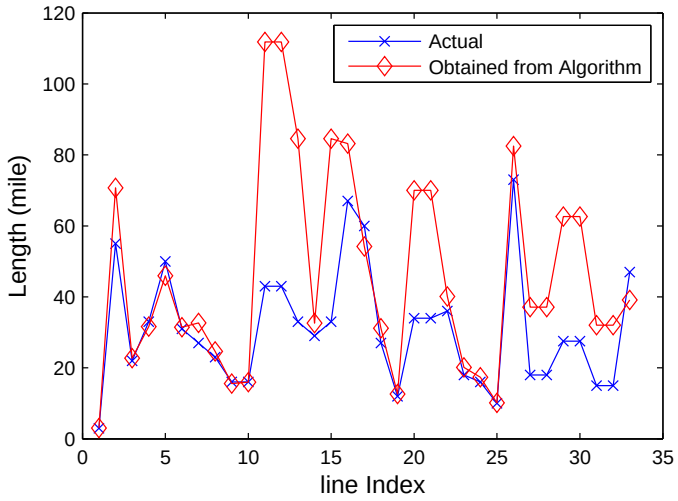


Figure 11.6: Comparison of the line lengths obtained from the KK algorithm with the actual ones for the 24-bus system.

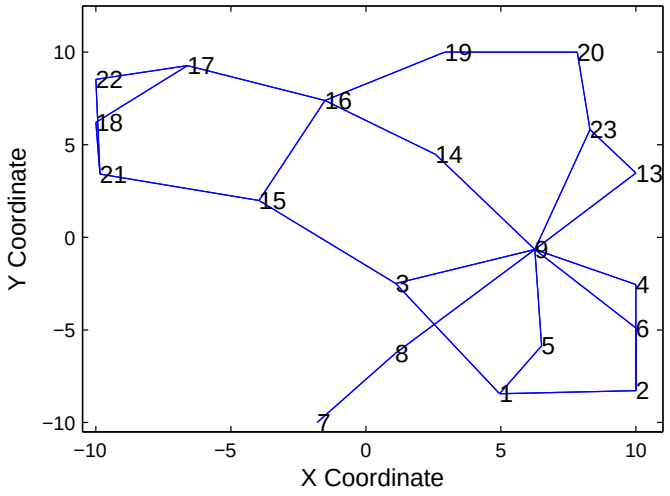


Figure 11.7: Geographic layout of the IEEE 24-bus system obtained from FD method.

# CHAPTER 12

# CONCLUSION

In this chapter, a summary of the thesis is presented and the main contributions are highlighted. The chapter concludes with final remarks and future research directions.

## 12.1 Summary and Contributions

**Chapter 2.** In this chapter, we develop two generation redispatch algorithms which improve the power system resiliency against cyber attacks. ROPF modifies the conventional OPF with the objective of optimizing resiliency instead of the generation cost. Security-compliant control subspace synthesis is a greedy algorithm that has lower computational complexity and is suitable for online RAS applications. Numerical results on the small IEEE 24-bus test case indicate that both methods provide sufficient security for the system with reasonable running time. For a larger case like the IEEE 118-bus system, ROPF offers extremely good security, yet the running time is quite high for online applications. On the other hand, the greedy algorithm offers a solution that is less secure, but much faster to compute.

**Chapter 3.** This chapter provides some background on GMDs, their negative impacts and the importance of their modeling. GIC modeling is presented in detail and methods to estimate the E-field using both magnetic and GIC data are developed.

**Chapter 4.** In this chapter, a novel line switching algorithm is developed to mitigate the GMD negative impacts. The algorithm minimizes the GIC-saturated reactive power loss based on TLODFs (counterparts of LODFs in GIC analysis). Some aspects of the AC analysis are considered to provide sufficient AC-related security measures. The computational complexity of the algorithm is analyzed and heuristics are utilized to reduce its running time for large-system applications. The

algorithm performance is evaluated through numerical results using the small 20-bus system, the medium-size UIUC 150-bus system and the large Texas 2000-bus case. The algorithm provides an effective tool to minimize the transformer damage during GMDs and improve the resiliency.

**Chapter 5.** This chapter investigates how to validate the GIC model using a modeless, SVD-based approach. Under an ideal uniform electric field, there exists a linear relation between the transformer GIC values and the E-field. Nonetheless, without accurate information of the power network topology and dc conductances, it becomes extremely difficult to characterize such linear dependency and accordingly estimate the E-field for validation. To tackle this, further analysis of the geomagnetic data suggests that the GIC matrix formed by different transformers across time will have rank-2 and the right singular vectors can be used to infer the E-field. This SVD-based approach has validated the linear relation using a realistic test case. The validation framework is also extended to account for non-uniform E-field and is successfully demonstrated through simulation. GMD modeling is a fundamental part of the GMD mitigation and the validation tool presented in this chapter can contribute to the resiliency against GMDs by improving the associated models. The work presented in this chapter was published in [59].

**Chapter 6.** In this chapter, a novel validation technique is presented which utilizes the network parameters (when available) to provide a stronger validation tool. This method introduces the transformer scales to account for the system uncertainties and provides the extra capability of detecting the outlier measurements. The proposed validation framework is demonstrated using a PowerWorld case study and its performance is extensively studied under various scenarios. More interesting real data validation is conducted using the GIC measurements provided by ATC. The data from five transformers are validated and the existing outlier in the set of the measurements is successfully detected. The work presented in this chapter was published in [60].

**Chapter 7.** In this chapter, an analytical technique is developed which derives the substation grounding resistances from the GIC measurements. In this technique, the relation between the GICs and the grounding resistances is linearized through some sensitivity parameters and linear regression is used to solve for the resistances. The uncertainty in the grounding resistances introduces error to the parameters of the linear model. To tackle this, the problem is reformulated

to decouple the uncertainties from the known parameters and regularized least squares is used for solving it. The effectiveness of the algorithm is evaluated using both a small test case as well as a 62,500 bus model of the EI system. As demonstrated, the algorithm can estimate the grounding resistances accurately even when the available GIC measurements are sparse and the assumed resistances have large error. The proposed technique reduces the uncertainties of the GMD model by providing more accurate grounding resistances. This improves the resiliency to GMDs through better assessment of the GICs and their risks. The work presented in this chapter was published in [61].

**Chapter 8.** In this chapter, the magnetic field measurements at 21 observatories in North America over a three-year period are extensively studied and various statistical measures are extracted from the data. Correlation analysis is performed to capture the possible dependencies between the observatories. It is observed that the magnetic fields at some observatories are highly correlated and this dependency is not always related to their geographic distance. To address this, the inverse distance weighting interpolation is modified to account for such dependencies. The modified interpolation improves over the conventional one as demonstrated through real data analysis. Finally, the correlation analysis is extended to the frequency domain using the wavelet transform. The proposed technique contributes to the resiliency by providing a better assessment of the GMD risks at distinct locations in the network. The work presented in this chapter was published in [62].

**Chapter 9.** In this chapter, the dependency of E-field on its earlier observations is studied and its dynamic model is developed. Analyzing the actual E-field data for several geomagnetic storms indicates that the transition parameters of the dynamic model have small variation over different datasets. This enables development of a general dynamic model which approximates the dynamics of any unknown E-field. Moreover, the system dynamics are utilized to improve the E-field estimation. The dynamic model is integrated into a Kalman filter and better E-field estimation is obtained. The advantage of the Kalman filter over the LS estimator is demonstrated through simulation. This work can facilitate the GMD model validation frameworks in Chapters 5 and 6 by providing a better E-field estimation than the investigated LS estimator. The work presented in this chapter was published in [63].

**Chapter 10.** This chapter considers the uncertainties in the GIC measurements and their impacts on the E-field estimation. Realistic noise scenarios for GIC measurements are considered and suitable estimators are proposed to handle different types of uncertainties. Moreover, a probabilistic model for GIC measurements has been developed. Using the developed model, the moments of the estimation error are calculated and an analytical model has been developed to assess the estimator's reliability. Similar to Chapter 9, this chapter contributes to the GMD resiliency by providing enhanced E-field estimation. The work presented in this chapter was published in [64] and [54].

**Chapter 11.** In this chapter, a framework is proposed to include GMD modeling into the already existing standard power system cases. The geographic coordinates are the key parameters which are missing in the standard cases and are essential for GMD studies. KK and BF are presented as two effective graph drawing techniques to generate the geographic layout and consequently get the coordinates. The proposed framework is applied to the 20-bus and the IEEE 24-bus systems and their coordinates are determined. Numerical results indicate that the layout obtained from KK preserves the line lengths, while BF provides a layout which is aesthetically pleasing, but its resulting lengths have little correlation with the actual lengths. The tool developed in this chapter can improve many aspects of the GMD analysis, including all the GMD-related studies in this thesis, by providing suitable benchmarks for evaluation purposes.

## 12.2 Future Work

This thesis suggests several directions for future research. With regard to the GMD mitigation framework, there are certainly a number of issues that are left for future work. First, the proposed algorithm minimizes the total loss, but imposes no limit on the loss of individual transformers. The algorithm can be further refined to restrict the loss of each transformer while minimizing the overall loss. Second, this framework focuses on line switching as the remedial action. Future research can extend this framework to other types of actions such as shunt capacitor switching and neutral blocking devices.

The parameter-based model validation presented in Chapter 6 enables outlier detection, but provides no explanation for the existing abnormalities. Presently, one of the ATC transformers is

discovered as an outlier, but the question of why it has such divergent behavior stays unanswered. Future research will answer this question by looking at possible factors such as different E-field, the nearby body of water or ground structure.

Several matters with regard to the magnetic field interpolation need to be considered in future research. First, the correlation analysis performed here does not consider the severity of the storm and it is not clear yet how the correlations change from a quiet day to a stormy day. We can address this by classifying the test days based on their level of solar activity and perform correlation analysis on each class separately. Second, the proposed interpolation can be integrated with the GIC model validation to achieve better performance. This integration can address the practical problem of validating the GICs on Wisconsin transformers.

# APPENDIX

# E-FIELD ESTIMATION UNDER GROUNDING RESISTANCE UNCERTAINTIES

This appendix demonstrates that the uncertainty in the substation grounding resistance affects the E-field estimation only by some scaling factor. Numerical results indicate that the sensitivity of the GIC at a particular substation to the grounding resistance of other substations is significantly lower than to its own grounding resistance. This implies that the sensitivity matrix is almost diagonal. Moreover, reference [45] demonstrates analytically that the sensitivity of the GIC at a substation to its grounding resistance does not depend on the E-field direction; i.e., the diagonal entries of the northward and eastward sensitivity matrices ($\mathbf{S}^N$ and $\mathbf{S}^E$) are equal. These two features of the sensitivity matrices (diagonally dominant matrices with approximately equal diagonal entries) suggest that the variation of the substation grounding resistances has linear impact on the E-field estimation.

Using the same setup as that presented in Chapter 7 (Section 7.6), the E-field measured at Fredericksburg on March 9, 2012, is enforced to the EI system and the synthetic GIC data is generated for the 100 substations by solving the GIC power flow and obtaining the induced GICs. To model the worst case scenario, extremely inaccurate grounding resistances are considered with 510% error from the actual resistances. The E-field is estimated from the GIC data using the LS method and the inaccurate grounding resistances. The estimated E-field is compared with the actual one and it is observed that the two fields have extremely high correlation. This experiment is repeated for five different sets of assumed grounding resistances (termed as R1 to R5) with the same level of inaccuracy (around 500% error) and similar results are observed. Table A.1 presents the Pearson correlation coefficient between the estimated E-field from each resistance set and the actual field, and also the ratio of their Euclidean norms. The correlation is more than 0.999

Table A.1: Correlation between the E-fields Estimated under Substation Grounding Resistance Uncertainty and the Actual Field

| Grounding Resistance Set | Northward E-Field | | Eastward E-Field | |
|---|---|---|---|---|
| | Correlation | Norm Ratio | Correlation | Norm Ratio |
| R1 | 1.0000 | 0.79 | 1.0000 | 0.76 |
| R2 | 1.0000 | 0.75 | 0.9997 | 0.82 |
| R3 | 0.9999 | 0.77 | 0.9992 | 0.76 |
| R4 | 0.9999 | 0.88 | 0.9998 | 0.90 |
| R5 | 1.0000 | 0.86 | 0.9998 | 0.87 |

even though the assumed resistances are extremely inaccurate. This verifies that the LS method estimates the E-filed accurately up to scaling in the presence of grounding resistance uncertainty.

# REFERENCES


[1] "2012 special reliability assessment interim report: Effects of geomagnetic disturbances on the bulk power system," North American Electric Reliability Corporation (NERC), Tech. Rep., Feb. 2012.

[2] "High-impact, low-frequency event risk to the north american bulk power system," North American Electric Reliability Corporation (NERC), Tech. Rep., Jun. 2010.

[3] "Electric power system resiliency: Challenges and opportunities," Electric Power Research Institute (EPRI), Tech. Rep., Feb. 2016.

[4] "IEEE guide for electric power distribution reliability indices - redline," IEEE Std 1366-2012 (Revision of IEEE Std 1366-2003), May 2012.

[5] "Severe impact resilience: Considerations and recommendations," North American Electric Reliability Corporation (NERC), Tech. Rep., May 2012.

[6] "Economic benefits of increasing electric grid resilience to weather outages," Executive Office of the President, Aug. 2013.

[7] A. P. Meliopoulos and A. G. Bakirtzis, "Corrective control computations for large power systems," *IEEE Transactions on Power Apparatus and Systems*, vol. PAS-102, no. 11, pp. 3598–3604, Nov. 1983.

[8] P. M. Anderson and B. K. LeReverend, "Industry experience with special protection schemes," *IEEE Transactions on Power Systems*, vol. 11, no. 3, pp. 1166–1179, Aug. 1996.

[9] C. F. Henville and E. Struyke, "Ras and streched power system," *Western Protective Relaying Conference*, 2006.

[10] "Special protection systems (SPS) / remedial action schemes (RAS): assessment of definition, regional practices, and application of related standards," North American Electric Reliability Corporation (NERC), Tech. Rep., Apr. 2013.

[11] M. Varghese, L. Jin, S. Ghosh, G. Lin, and B. Pek, "The caiso experience of implementing automated remedial action schemes in energy management systems," in *2009 IEEE Power Energy Society General Meeting*, Jul. 2009.

[12] J. Wen, W. H. E. Liu, P. L. Arons, and S. K. Pandey, "Evolution pathway towards wide area monitoring and protection, a real-world implementation of centralized ras system," *IEEE Transactions on Smart Grid*, vol. 5, no. 3, pp. 1506–1513, May 2014.

[13] R. Ramanathan, B. Tuck, and J. O'Brien, "BPA's experience of implementing remedial action schemes in power flow for operation studies," in *2013 IEEE Power Energy Society General Meeting*, Jul. 2013.

[14] S. C. Pai and J. Sun, "BCTCs experience towards a smarter grid - increasing limits and reliability with centralized intelligence remedial action schemes," in *Electric Power Conference, 2008. EPEC 2008. IEEE Canada*, Oct. 2008, pp. 1–7.

[15] A. A. Fouad, A. Ghafurian, K. Nodehi, and Y. Mansour, "Calculation of generation-shedding requirements of the B.C. hydro system using transient energy functions," *IEEE Power Engineering Review*, vol. PER-6, no. 5, pp. 31–32, May 1986.

[16] Y. Zhang and K. Tomsovic, "Adaptive remedial action scheme based on transient energy analysis," in *Power Systems Conference and Exposition, 2004. IEEE PES*, Oct. 2004, pp. 925–931 vol.2.

[17] I. Genc, R. Diao, V. Vittal, S. Kolluri, and S. Mandal, "Decision tree-based preventive and corrective control applications for dynamic security enhancement in power systems," *IEEE Transactions on Power Systems*, vol. 25, no. 3, pp. 1611–1619, Aug. 2010.

[18] D. Ruiz-Vega and M. Pavella, "A comprehensive approach to transient stability control. ii. open loop emergency control," *IEEE Transactions on Power Systems*, vol. 18, no. 4, pp. 1454–1460, Nov. 2003.

[19] B. Gou and H. Zhang, "Fast real-time corrective control strategy for overload relief in bulk power systems," *IET Generation, Transmission Distribution*, vol. 7, no. 12, pp. 1508–1515, Dec. 2013.

[20] W. Shao and V. Vittal, "Corrective switching algorithm for relieving overloads and voltage violations," *IEEE Transactions on Power Systems*, vol. 20, no. 4, pp. 1877–1885, Nov. 2005.

[21] V. D. Albertson, J. M. Thorson, R. E. Clayton, and S. C. Tripathy, "Solar-induced-currents in power systems: Cause and effects," *IEEE Transactions on Power Apparatus and Systems*, vol. PAS-92, no. 2, pp. 471–477, Mar. 1973.

[22] J. Kappenman, "Low-frequency protection concepts for the electric power grid:geomagnetically induced current (GIC) and E3 HEMP mitigation," Oak Ridge National Laboratory (ORNL), 2010.

[23] J. G. Kappenman, S. R. Norr, G. A. Sweezy, D. L. Carlson, V. D. Albertson, J. E. Harder, and B. L. Damsky, "GIC mitigation: a neutral blocking/bypass device to prevent the flow of GIC in power systems," *IEEE Transactions on Power Delivery*, vol. 6, no. 3, pp. 1271–1281, Jul. 1991.

[24] H. Zhu and T. J. Overbye, "Blocking device placement for mitigating the effects of geomagnetically induced currents," *IEEE Transactions on Power Systems*, vol. 30, no. 4, pp. 2081–2089, Jul. 2015.

[25] E. Arajärvi, R. Pirjola, and A. Viljanen, "Effects of neutral point reactors and series capacitors on geomagnetically induced currents in a high-voltage electric power transmission system," *Space Weather*, vol. 9, no. 11, 2011.

[26] L. Bolduc, M. Granger, G. Pare, J. Saintonge, and L. Brophy, "Development of a dc current-blocking device for transformer neutrals," *IEEE Transactions on Power Delivery*, vol. 20, no. 1, pp. 163–168, Jan. 2005.

[27] B. Kovan and F. de León, "Mitigation of geomagnetically induced currents by neutral switching," *IEEE Transactions on Power Delivery*, vol. 30, no. 4, pp. 1999–2006, Aug. 2015.

[28] J. G. Kappenman, "Mitigation of geomagnetically induced and dc stray currents," EPRI Rep. EL-3295, Tech. Rep., 1983.

[29] A. A. Hussein and M. H. Ali, "Suppression of geomagnetic induced current using controlled ground resistance of transformer," *Electric Power Systems Research*, vol. 140, pp. 9 – 19, 2016.

[30] J. G. Rolim and L. J. B. Machado, "A study of the use of corrective switching in transmission systems," *IEEE Transactions on Power Systems*, vol. 14, no. 1, pp. 336–341, Feb. 1999.

[31] K. Hedman, R. O'Neill, E. Fisher, and S. Oren, "Optimal transmission switching with contingency analysis," in *IEEE PES General Meeting*, Jul. 2010.

[32] A. A. Mazi, B. F. Wollenberg, and M. H. Hesse, "Corrective control of power system flows by line and bus-bar switching," *IEEE Power Engineering Review*, vol. PER-6, no. 8, pp. 53–53, Aug. 1986.

[33] V. D. Albertson, J. G. Kappenman, N. Mohan, and G. A. Skarbakka, "Load-flow studies in the presence of geomagnetically-induced currents," *IEEE Transactions on Power Apparatus and Systems*, vol. PAS-100, no. 2, pp. 594–607, Feb. 1981.

[34] R. A. Walling and A. N. Khan, "Characteristics of transformer exciting-current during geomagnetic disturbances," *IEEE Transactions on Power Delivery*, vol. 6, no. 4, pp. 1707–1714, Oct. 1991.

[35] J. Kappenman, "Geomagnetic storms and their impacts on the U. S. power grid," Metatech Corporation Report Meta-R-319, Tech. Rep., Jan. 2010.

[36] D. H. Boteler and R. J. Pirjola, "Modelling geomagnetically induced currents produced by realistic and uniform electric fields," *IEEE Transactions on Power Delivery*, vol. 13, no. 4, pp. 1303–1308, Oct. 1998.

[37] T. J. Overbye, T. R. Hutchins, K. Shetye, J. Weber, and S. Dahman, "Integration of geomagnetic disturbance modeling into the power flow: A methodology for large-scale system studies," in *North American Power Symposium (NAPS)*, Sep. 2012.

[38] R. Horton, D. Boteler, T. J. Overbye, R. Pirjola, and R. C. Dugan, "A test case for the calculation of geomagnetically induced currents," *IEEE Transactions on Power Delivery*, vol. 27, no. 4, pp. 2368–2373, Oct. 2012.

[39] A. B. Birchfield, K. M. Gegner, T. Xu, K. S. Shetye, and T. J. Overbye, "Statistical considerations in the creation of realistic synthetic power grids for geomagnetic disturbance studies," *IEEE Transactions on Power Systems*, 2016.

[40] R. Pirjola, "Properties of matrices included in the calculation of geomagnetically induced currents (GICs) in power systems and introduction of a test model for gic computation algorithms," *Earth, Planets and Space*, vol. 61, no. 2, pp. 263–272, 2009.

[41] A. Yan, D. Zhou, and L. Marti, "Analysis of geomagnetically induced currents," in *2013 IEEE Power Energy Society General Meeting*, Jul. 2013, pp. 1–6.

[42] D. H. Boteler, A. J. C. Lackey, L. Marti, and S. Shelemy, "Equivalent circuits for modelling geomagnetically induced currents from a neighbouring network," in *2013 IEEE Power Energy Society General Meeting*, Jul. 2013, pp. 1–5.

[43] R. Pirjola, "Study of effects of changes of earthing resistances on geomagnetically induced currents in an electric power transmission system," *Radio Science*, vol. 43, no. 1, 2008, rS1004.

[44] L. Marti, A. Rezaei-Zare, and D. Boteler, "Calculation of induced electric field during a geomagnetic storm using recursive convolution," *IEEE Transactions on Power Delivery*, vol. 29, no. 2, pp. 802–807, Apr. 2014.

[45] U. Bui, T. J. Overbye, K. Shetye, H. Zhu, and J. Weber, "Geomagnetically induced current sensitivity to assumed substation grounding resistance," in *North American Power Symposium (NAPS), 2013*, Sep. 2013.

[46] "IEEE guide for measuring earth resistivity, ground impedance, and earth surface potentials of a grounding system," IEEE Std 81-2012 (Revision of IEEE Std 81-1983), pp. 1–86, Dec. 2012.

[47] A. P. S. Meliopoulos, G. Cokkinides, H. Abdallah, S. Duong, and S. Patel, "A pc based ground impedance measurement instrument," *IEEE Transactions on Power Delivery*, vol. 8, no. 3, pp. 1095–1106, Jul. 1993.

[48] F. Dawalibi and D. Mukhedkar, "Ground electrode resistance measurements in non uniform soils," *IEEE Transactions on Power Apparatus and Systems*, vol. PAS-93, no. 1, pp. 109–115, Jan. 1974.

[49] G. F. Thug, *Earth Resistances*. London: Georges Newnes Limited, 1964.

[50] F. Dawalibi and D. Mukhedkar, "Optimum design of substation grounding in a two layer earth structure: Part i, analytical study," *IEEE Transactions on Power Apparatus and Systems*, vol. 94, no. 2, pp. 252–261, Mar. 1975.

[51] Z. Xu, J. L. Gannon, and E. J. Rigler, "Report of geomagnetic pulsation indices for space weather applications," U.S. Geological Survey, Tech. Rep. 1166, 2013.

[52] U. Mersmann, W. Baujohann, F. Kuppers, and K. Lange, "Analysis of an eastward electrojet by means of upward continuation of ground-based magnetometer data," *Journal of Geophysics*, vol. 45, pp. 281–298, 1979.

[53] C. D. Beggan and S. A. McLay, "Interpolation of magnetic and electric fields using spherical elementary current systems," in *Ionospheric Radio Systems and Techniques (IRST 2012), 12th IET International Conference on*, May 2012, pp. 1–5.

[54] M. Kazerooni, H. Zhu, K. Shetye, and T. J. Overbye, "Estimation of geoelectric field for validating geomagnetic disturbance modeling," in *Power and Energy Conference at Illinois (PECI)*, Feb. 2013.

[55] Synthetic Power Cases-Illinois Center for a Smarter Electric Grid. [Online]. Available: http://icseg.iti.illinois.edu/

[56] Power Systems Test Case Archives. [Online]. Available: http://www2.ee.washington.edu/research/pstca/

[57] G. D. Battista, P. Eades, R. Tamassia, and I. G. Tollis, *Graph Drawing: Algorithms for the Visualization of Graphs*, 1st ed. Prentice Hall PTR, 1998.

[58] U. Brandes, *Drawing on Physical Analogies*. Berlin, Heidelberg: Springer Berlin Heidelberg, 2001.

[59] M. Kazerooni, H. Zhu, and T. J. Overbye, "Singular value decomposition in geomagnetically induced current validation," in *Innovative Smart Grid Technologies Conference (ISGT), 2015 IEEE Power Energy Society*, Feb. 2015.

[60] M. Kazerooni, H. Zhu, T. Overbye, and D. Wojtczak, "Transmission system geomagnetically induced current model validation," accepted for publication in *IEEE Transactions on Power Systems*, 2016.

[61] M. Kazerooni, H. Zhu, and T. J. Overbye, "Improved modeling of geomagnetically induced currents utilizing derivation techniques for substation grounding resistance," accepted for publication in *IEEE Transactions on Power Delivery*, 2016.

[62] M. Kazerooni, H. Zhu, and T. J. Overbye, "Use of sparse magnetometer measurements for geomagnetically induced current model validation," in *North American Power Symposium (NAPS)*, Oct. 2015.

[63] M. Kazerooni, H. Zhu, and T. J. Overbye, "Dynamic modeling and filtering in geomagnetically induced current validation," in *North American Power Symposium (NAPS)*, Sep. 2014.

[64] M. Kazerooni, H. Zhu, and T. J. Overbye, "Probabilistic modeling and reliability analysis for validating geomagnetically induced current data," in *North American Power Symposium (NAPS)*, 2013.

[65] K. Stouffer, J. Falco, and K. Scarfone, "Guide to industrial control systems (ics) security," *NIST Special Publication*, vol. 800, 2008.

[66] "A summary of control system security standards activities in the energy sector," U.S. Department of Energy Office of Electricity Delivery and Energy Reliability, Oct. 2005.

[67] "NERC CIP 002 1 - critical cyber asset identification," National Energy Regulatory Comission, Tech. Rep., 2006.

[68] J. Weiss, "Are the NERC CIPS making the grid less reliable," *Control Global*, 2009.

[69] S. Mohan, S. Bak, Y. E. E. Betti, H. Yun, L. Sha, and M. Caccamo, "S3a: Secure system simplex architecture for enhanced security and robustness of cyber-physical systems," in *Proceedings of the 2Nd ACM International Conference on High Confidence Networked Systems*, 2013.

[70] S. Cheung, B. Dutertre, M. Fong, U. Lindqvist, K. Skinner, and A. Valdes, "Using model-based intrusion detection for scada networks," in *Proceedings of the SCADA Security Scientific Symposium*, Miami Beach, Florida, Jan. 2007.

[71] W. M. Goble, *Control Systems Safety Evaluation and Reliability*. International Society of Automation, 2010.

[72] W. Shao and V. Vittal, "Corrective switching algorithm for relieving overloads and voltage violations," *IEEE Transactions on Power Systems*, vol. 20, no. 4, pp. 1877–1885, Nov. 2005.

[73] H. Ota, Y. Kitayama, H. Ito, N. Fukushima, K. Omata, K. Morita, and Y. Kokai, "Development of transient stability control system (tsc system) based on on-line stability calculation," *IEEE Transactions on Power Systems*, vol. 11, no. 3, pp. 1463–1472, Aug. 1996.

[74] C. W. Taylor, F. R. Nassief, and R. L. Cresap, "Northwest power pool transient stability and load shedding controls for generation-load imbalances," *IEEE Transactions on Power Apparatus and Systems*, vol. PAS-100, no. 7, pp. 3486–3495, Jul. 1981.

[75] S. M. Rovnyak, K. Mei, and G. Li, "Fast load shedding for angle stability control," in *Power Engineering Society General Meeting, 2003, IEEE*, Jul. 2003.

[76] G. Hug-Glanzmann and G. Andersson, "Decentralized optimal power flow control for overlapping areas in power systems," *IEEE Transactions on Power Systems*, vol. 24, no. 1, pp. 327–336, Feb. 2009.

[77] A. R. Escobedo, E. Moreno-Centeno, and K. W. Hedman, "Topology control for load shed recovery," *IEEE Transactions on Power Systems*, vol. 29, no. 2, pp. 908–916, Mar. 2014.

[78] "D-FACTS devices in PowerWorld simulator." [Online]. Available: http://www.powerworld.com/files/clientconf2014/07Weber_DFACTS.pdf

[79] A. B. Birchfield, K. M. Gegner, T. Xu, K. S. Shetye, and T. J. Overbye, "Statistical considerations in the creation of realistic synthetic power grids for geomagnetic disturbance studies," *IEEE Transactions on Power Systems*, 2016.

[80] V. D. Albertson, J. M. Thorson, and S. A. Miske, "The effects of geomagnetic storms on electrical power systems," *IEEE Transactions on Power Apparatus and Systems*, vol. PAS-93, no. 4, pp. 1031–1044, Jul. 1974.

[81] International Real-time Magnetic Observatory Network. [Online]. Available: http://www.intermagnet.org/

[82] G. B. Giannakis, G. Mateos, S. Farahmand, V. Kekatos, and H. Zhu, "USPACOR: Universal sparsity-controlling outlier rejection," in *2011 IEEE International Conference on Acoustics, Speech and Signal Processing (ICASSP)*, May 2011, pp. 1952–1955.

[83] X. Dong, Y. Liu, and J. G. Kappenman, "Comparative analysis of exciting current harmonics and reactive power consumption from GIC saturated transformers," in *IEEE Power Engineering Society Winter Meeting*, Jan. 2001.

[84] T. J. Overbye, K. S. Shetye, T. R. Hutchins, Q. Qiu, and J. D. Weber, "Power grid sensitivity analysis of geomagnetically induced currents," *IEEE Transactions on Power Systems*, vol. 28, no. 4, pp. 4821–4828, Nov. 2013.

[85] T. Guler, G. Gross, and M. Liu, "Generalized line outage distribution factors," *IEEE Transactions on Power Systems*, vol. 22, no. 2, pp. 879–881, May 2007.

[86] F. L. Alvarado, "Computational complexity in power systems," *IEEE Transactions on Power Apparatus and Systems*, vol. 95, no. 4, pp. 1028–1037, Jul. 1976.

[87] R. Yuster and U. Zwick, "Fast sparse matrix multiplication," *ACM Trans. Algorithms*, vol. 1, no. 1, pp. 2–13, Jul. 2005.

[88] G. H. Golub and C. F. V. Loan, *Matrix Computations*, 3rd ed. Johns Hopkins, 1996.

[89] L. C. Liu, Y and R. Pirjola, "Observations and modeling of gic in the chinese large-scale high-voltage power networks," *J. Space Weather Space Clim.*, vol. 4, no. A03, 2014.

[90] NERC, "Benchmark geomagnetic disturbance event," GMDTF Meeting, North American Electric Reliability Corporation (NERC), Tech. Rep., Apr. 2014.

[91] "Special sensor ultroviolet spectrograph imager." [Online]. Available: http://ssusi.jhuapl.edu/

[92] J. J. Leader, *Numerical Analysis and Scientific Computation*. Pearson Addison Wesley, 2004.

[93] T. M. J. Fruchterman and E. M. Reingold, "Graph drawing by force-directed placement," *Softw. Pract. Exper.*, vol. 21, no. 11, pp. 1129–1164, Nov. 1991.

[94] T. Kamada and S. Kawai, "An algorithm for drawing general undirected graphs," *Information Processing Letters*, vol. 31, no. 1, pp. 7 – 15, 1989.

[95] Power Systems Control and Automation Laboratory. [Online]. Available: http://pscal.ece.gatech.edu/archive/testsys/lines.html